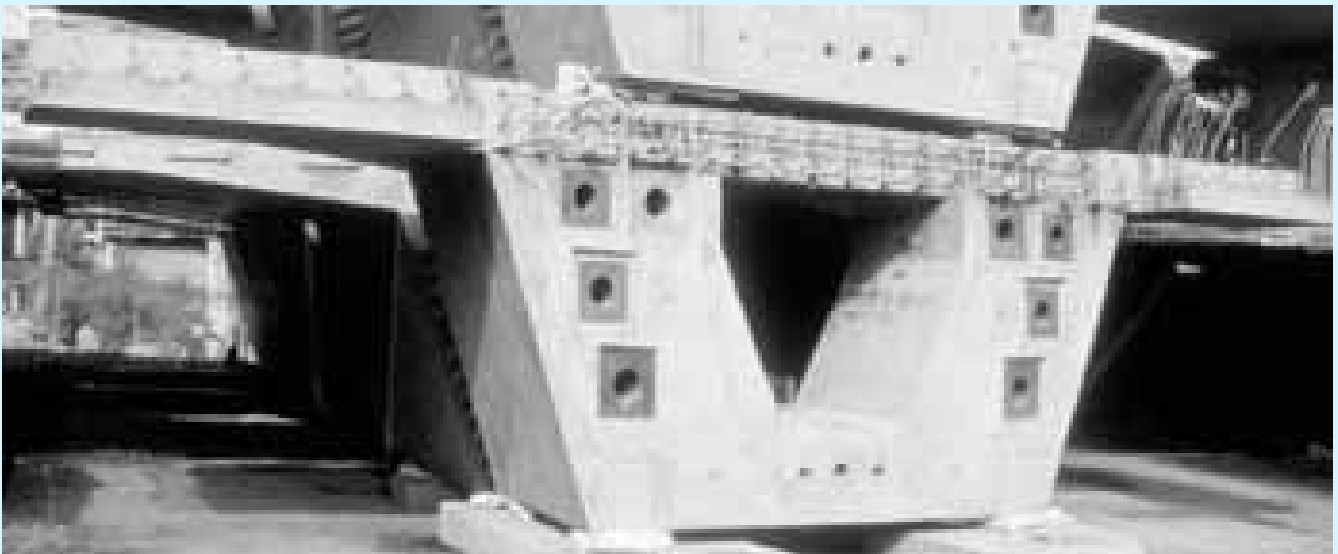


Chaffo Nigatu

Design of Pier Segments in Segmental Hollow Box Girder Bridges



Cuvillier Verlag Göttingen

Design of Pier Segments in Segmental Hollow Box Girder Bridges

*Vom Promotionsausschuss der
Technischen Universität Hamburg-Harburg
zur Erlangung des akademischen Grades
Doktor-Ingenieur (Dr.-Ing.)
genehmigte Dissertation*

von

*Ing. Nigatu Chaffo, MSc
aus Äthiopien*

2003

1. Gutachter: Univ.-Prof. Dr.-Ing. Günter Axel Rombach
2. Gutachter: Univ.-Prof. Dr.-Ing. Uwe Starossek
Prüfungsvorsitzender: Univ.-Prof. Dr.-Ing. Lutz Franke

Tag der mündlichen Prüfung: 19. Januar 2004

Acknowledgements

First and foremost I would like to give special thanks to my Heavenly Father, the Almighty God for all His assistance and comfort that He has bestowed on me during my stay in Germany. Many thanks go to all of my immediate families who have supported me through prayers during my study.

My special thanks goes to Prof. Dr.-Ing. G. Rombach who had communicated with me starting from my home university and encouraged me to actualise my dreams to pursue a research work in Segmental Bridge at Technical University Hamburg-Harburg, Germany. Also during my stay in Hamburg, his immediate supervision and accessibility has helped me a lot to achieve my goals. My honourable respect and thanks goes to German Academic Exchange Service (DAAD) who has supported me financially to conduct the research work.

I would like to thank Prof. Dr.-Ing. U. Starossek for assuming the position of co-referat and Prof. Dr.-Ing. L. Franke for assuming the position of chairmanship of the defence committee.

Also my thank goes to Prof. I. R. Dr.-Ing. U. Quast who had read my interim reports and wrote a recommendation for extension of my research work. My cordial thanks goes to my former office mate Dr.-Ing. Angelika Specker for her helps during my arrival and later.

During tedious correction work of the manuscript, my thank goes to my Nigerian flat mate Jimoh A. Yamah, Rebecca Bednall and Joanna L. Yates from the United Kingdom. I would like to thank Jimoh for his kind friendship.

Finally I would like to thank my local church in Arba Minch and Bethel Evangelical Church in Hamburg for their prayer. This dissertation is dedicated to my parents Chaffo Dullo and Daffe Mua for their love through out my life.

Hamburg December 2003

Nigatu Chaffo

Table of contents

Symbols	XI
1 Introduction	1
1.1 General	1
1.1.1 Prestressing.....	3
1.1.2 Construction – Assembling of segments.....	4
1.1.3 Typical segmental hollow box girder bridge	7
1.2 Research objectives	11
1.3 Scope of this dissertation	12
2 Background information	13
2.1 Strut-and-tie model.....	13
2.2 Structure’s B-and-D region	15
2.3 General design procedure and modeling.....	16
2.4 Modeling of individual B-and-D regions	17
2.4.1 Principles and general design procedures	17
2.4.2 The load path method	19
2.4.3 Model selection	24
2.5 Dimensioning of struts, ties and nodes.....	25
2.5.1 Definitions and general rule	25
2.5.2 Struts-and-ties.....	25
2.5.3 Nodes	27
2.6 Design of diaphragms in bridges and shear walls	27
2.6.1 Shear wall with central support	28
2.6.2 Shear wall with two supports and without opening.....	28
2.6.3 Shear wall with two supports and opening under pure shear.....	29
2.7 Strut-and-tie model for anchorage regions	30
2.7.1 The tripod model.....	31
2.7.2 Corbel action.....	32
2.7.3 Frame action	33
2.7.4 Extent of the D-region	33
2.7.5 Shear-friction.....	34
2.7.6 Skew reinforcement	35

2.7.7	Strut-and-tie model of Neuser	36
2.8	Design of anchorage zone	38
2.8.1	General	38
2.8.2	Verification of anchorage design	39
2.8.3	Concentrated force.....	40
2.8.4	Practical modeling.....	41
2.8.5	Design of anchorage zone according to CEB-FIP.....	45
2.8.6	Design of anchorage zone according to AASHTO specifications	48
2.8.6.1	Anchorage stresses	48
2.8.6.2	Forces and reinforcement in general zones.....	49
3	Stresses in shear wall analyzed by finite element method	51
3.1	Modeling	51
3.2	Evaluation of load arrangement.....	56
3.3	Elastic and inelastic analysis	62
3.3.1	Evaluation of results for permanent loading	62
3.3.1.1	Shear wall with two supports and without opening.....	62
3.3.1.2	Shear wall with two supports and with opening.....	63
3.3.1.3	Shear wall with central support and without opening	65
3.3.2	Evaluation of results for maximum shear	67
3.3.2.1	Shear wall with two supports and without opening.....	67
3.3.2.2	Shear wall with two supports and with opening.....	70
3.3.3	Crack formation due to maximum shear loading.....	71
3.3.3.1	Shear wall with two supports and without opening.....	71
3.3.3.2	Shear wall with two supports and with opening.....	72
3.3.4	Summary	73
4	3D-finite element model of an existing segmental bridge	75
4.1	Modeling	75
4.2	Verification	81
4.3	Dimensions, loads and prestressing.....	82
4.4	Finite element analysis of the bridge	84

4.4.1	Permanent loading	84
4.4.1.1	Pier segment without manhole.....	84
4.4.1.2	Pier segment with manhole.....	87
4.4.2	Load case for max torsion.....	90
4.4.2.1	Pier segment without manhole.....	90
4.4.2.2	Pier segment with manhole.....	92
4.4.3	Load case for shear	94
4.4.3.1	Pier segment without manhole.....	94
4.4.3.2	Pier segment with manhole.....	97
4.4.4	Summary	99
5	Transfer of prestressing force from diaphragm to webs and slabs	101
5.1	Force distribution due to load arrangement on the 1 row	103
5.2	Force distribution due to load arrangement on the 2 row	104
5.3	Force distribution due to load arrangement on the 3 row	105
5.4	Force distribution due to load arrangement on the column A	106
5.5	Force distribution due to load arrangement on the column B	107
5.6	Force distribution due to load arrangement on the column C.....	108
6	Evaluation of strut-and-tie model for design of diaphragms	109
6.1	Strut-and-tie model for loads from superstructure	109
6.1.1	Closed diaphragm - shear and torsion loading	109
6.1.2	Pier segment with two supports and manhole	110
6.1.3	Pier segment with central support and closed diaphragm permanent loads	113
6.2	Strut-and-tie model for prestressing force	116
7	Summary and conclusion	119
	References	121
	Appendix A Forces of the tripod model	129
	Appendix B Strut-and-tie model for indirect support.....	133
	Appendix C Comparison of tensile forces	137
	Appendix D Derivation of formulae.....	139
	Appendix E Strut-and-tie model for direct support with open diaphragm ..	145
	Appendix F Tendon and reinforcement layout of pier segment.....	149

Symbols

Some of the symbols used in the formulae and for geometrical descriptions that are not explained inside the dissertation are given below. In general the notations of Eurocodes EC1 and EC2 are used

Latin upper case symbols

A_B	Cross-sectional area of concrete in contact with bearing
A_c	Total cross-sectional area of a concrete section
A_L	Loaded area
A_p	Area of prestressing tendon or tendons
A_s	Area of reinforcement within the tension zone
A_{sw}	Cross-sectional area of shear reinforcement
A_{ss}	Area of stirrup steel
E_{cd}	Design value of secant modulus of elasticity
E_{cm}	Secant modulus of elasticity of normal weight concrete
E_c	Tangent modulus of elasticity of normal weight concrete at a stress of $\omega_c=0$ and at 28 days
E_p	Modulus of elasticity of prestressing steel
E_s	Modulus of elasticity of reinforcement or prestressing steel
F	Action or force
G	Permanent action Shear modulus
J	Second moment of area
M	Bending moment
M_{Sd}	Design value of the applied internal bending moment
M_T	Torsional moment
M_{uls}	Bending moment in ultimate limit state
N	Axial force
P	Prestressing force
$P_{m,t}$	Mean value of the prestressing force at time t , at any point distance x along the member
P_0	Initial force at the active end of the tendon immediately after stressing
Q	Variable action

Q_{ik}	Double axle load (load model 1, EC 1, part 3)
T_{Sd}	Design value of applied torsional moment
V	Shear force
V_p	Vertical force from prestressing

Latin lower case symbols

a	Distance
b	Width
b_w	Smallest web width of T, I or L-beams
d	Diameter ; depth
f	Strength (of a material)
f_c	Compressive strength of concrete
f_{cd}	Design value of concrete cylinder compressive strength
f_{ck}	Characteristic compressive cylinder strength of concrete at 28 days
f_{cm}	Mean value of concrete cylinder compressive strength
f_{ctm}	Mean value of axial tensile strength of concrete
$f_{ct,0,05k}$	Characteristic tensile strength of concrete (5% fractile)
f_{tk}	Characteristic tensile strength of reinforcement
f_{yd}	Design yield strength of reinforcement
f_{yk}	Characteristic yield stress of reinforcement
h	Height ; overall depth of cross-section
l	Length; span
l_{seg}	Length of one segment
q	Variable action - live load
q_1	Live load in lane 1
q_2	Live load in lane 2
s	Spacing of stirrups
t	Thickness ; time being considered
x, y, z	Coordinates
x	Neutral axis depth
z	Lever arm of internal forces

Greek symbols

ζ	Coefficient taking account of long term effect of compressive strength
η	Angle ; ratio
ν_c	Partial safety factors for concrete material properties
ν_G	Partial safety factors for permanent action
ν_Q	Partial safety factors for variable action
ν_s	Partial safety factors for the properties of reinforcement or prestressing steel
κ	Strain
κ_c	Compressive strain in the concrete
κ_{c1}	Compressive strain in the concrete at the peak stress f_c
κ_{c2}	Strain in the concrete at reaching the maximum strength
κ_{cu}	Ultimate compressive strain in the concrete
σ	Coefficient of friction
ω_c	Compressive stress in the concrete
ω_{po}	Initial stress in tendon during tensioning
ω_{pmo}	Stress in the tendon immediately after stressing or transfer
ω_x	Compressive stress in x direction
ω_y	Compressive stress in y direction
ω_z	Compressive stress in z direction
λ	Diameter of a reinforcing bar or a prestressing duct (or d_s)
τ	Poisson's ratio

Subscripts

c	Concrete ; compression
d	Design
eff	Effective
f	Flange
F	Action
g	Permanent action
k	Characteristic
max	Maximum
min	Minimum

p	Prestressing force
ps	Prestressing steel
q	Variable action
R	Resistance
s	Reinforcing steel
S	Internal moments and forces
sup	Superior ; upper
t	Tension or torsion
u	Ultimate
v	Shear
w	Web
x,y,z	Coordinates
y	Yield

1 Introduction

1.1 General

Segments are slices of a structural element between joints which are perpendicular to the longitudinal axis of the structure stressed together by means of prestressing tendons. The first segmental bridge was built by Eugene Freyssinet in the late 1940s. He used precast I-beam segments for construction of well-known six bridges over the Marne River in France [1]. The longitudinal structures were assembled from precast elements that were prestressed vertically and connected by dry joints and longitudinal post-tensioned tendons. Precast segments were also used by Jean Muller to build a girder bridge in upstate New York, where longitudinal girders were precast in three segments each, which were assembled by dry joints and longitudinal post-tensioning tendons [1a]. The above mentioned type of constructions refers to I-beam segmental bridges. Nowadays, mainly hollow box girder segmental bridges are built (Fig. 1.1, 1.2). The first one was the bridge over the Seine at Choisy-le-Roi in France, which was built in 1962 and has length $l = 37+55+37 = 129$ m [1b]. The various hollow box sections are shown in figure 1.1.

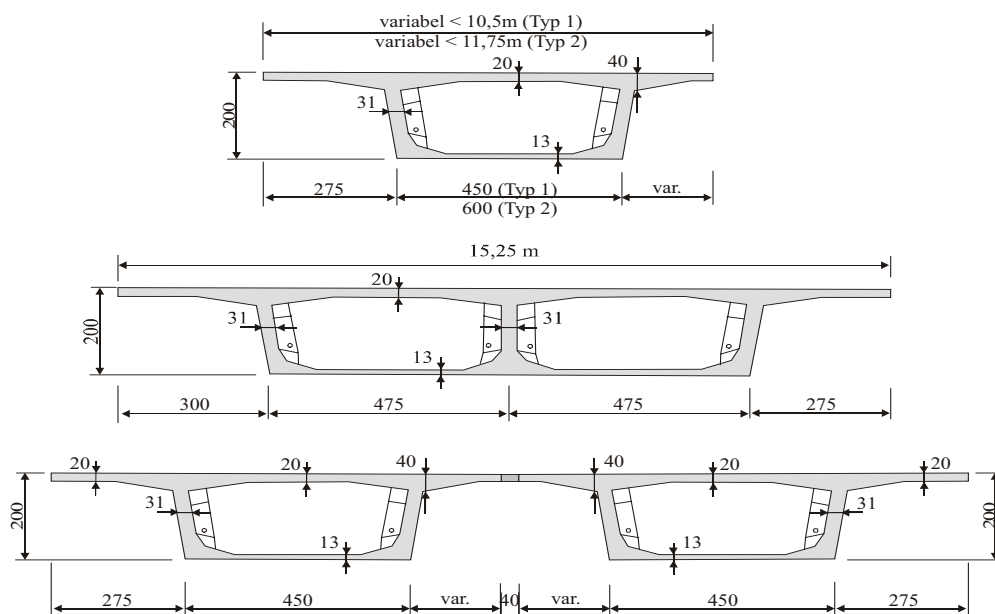


Figure 1.1 Cross-sections of the Seine bridge at Choisy-le-Roi in France

Segmental hollow box girder bridges have gained great acceptance throughout the world and the instance of use of this type of construction have increased rapidly in the recent years [100]. In Germany the first segmental bridge over the River Lech was built in 1968. In 1999 the 'Deutscher Beton-Verein' published the first recommendations for the design of hollow box girder segmental bridges [13].

In this thesis the term segmental bridge refers to a structure, which consists of prefabricated segments with hollow box girder cross-section that are stressed together by tendons.



Figure 1.2 Segmental hollow box girder bridge (SES Bangkok)

The main advantages of this type of construction are as follows:

- ⚡ due to mass production in a precast yard it has the potential for achieving high quality and high strength concrete
- ⚡ appearance: arbitrary shape of segment, coloured concrete surface
- ⚡ short construction time because segments are prefabricated while the substructure is being built – no need of in-situ concrete
- ⚡ no need of falsework (but erection truss required)
- ⚡ the possibility of change of curvature in horizontal and vertical directions of the structure and also for roadway super elevation
- ⚡ the effect of creep and shrinkage will be less since the precast segments will have appropriate age before erection and stressing longitudinally

- ⊘ the construction is not affected by weather conditions (dry joints)
- ⊘ the traffic is not disturbed by the construction
- ⊘ the dead load of the structure is reduced due to hollow box section and external prestressing
- ⊘ it is economical as it requires less mild reinforcement
- ⊘ full prestressed structure – no tensile stresses under serviceability loads; higher fatigue strength
- ⊘ easy transportation of prefabricated elements - small segments in relation to long Ebeams

The disadvantages for this type of construction are:

- ⊘ careful geometry control is required during production of segments
- ⊘ development of new design method
- ⊘ extra cost for prestressing and erection truss
- ⊘ careful alignment control during erection
- ⊘ safety (e.g. in case of fire)
- ⊘ joints between segments

1.1.1 Prestressing

Segmental bridges can be prestressed internally, externally or a combination of the two. Cracks that have reached the internal tendons in the joint have caused serious serviceability problems in the past. These cracks cannot be limited since there is no mild reinforcement that crosses the joint. For this reason, nowadays mainly external prestressing, where the tendons are located inside the hollow box but outside the concrete, is used in segmental construction (Fig. 1.3). Therefore in this thesis only this type of tendon layout will be treated.



Figure 1.3 Externally prestressed segmental bridge (SES Bangkok)–pier segment

The advantages of external prestressing are as follows:

- ⌘ inspection and replacement of tendons is possible
- ⌘ easier installation of longitudinal tendons
- ⌘ good corrosion protection of post-tension cables
- ⌘ less dead load since no tendons are located in the webs (thinner webs)
- ⌘ grouting is easier due to the straight alignment
- ⌘ less friction (no wobble losses)
- ⌘ prestressing force can be modified after construction due to extra ducts

The disadvantages of external prestressing are as follows:

- ⌘ additional mild reinforcement required as the increase of tendon stress $\div \omega_p$ is small under ultimate loads
- ⌘ additional cost for duct, anchorage, deviators
- ⌘ polygonal tendon layout
- ⌘ deviators and eccentric anchorage for post-tensioning forces required

1.1.2 Construction – Assembling of segments

From the beginning, post-tensioned segmental box girder bridges have been refined and modified in many different ways. Segments can be precast or cast-in-

place; precasting can be done with short line or long line casting beds. Erection can be done by balanced cantilever construction method, progressive placement method or span-by-span construction method (Fig. 1.4).

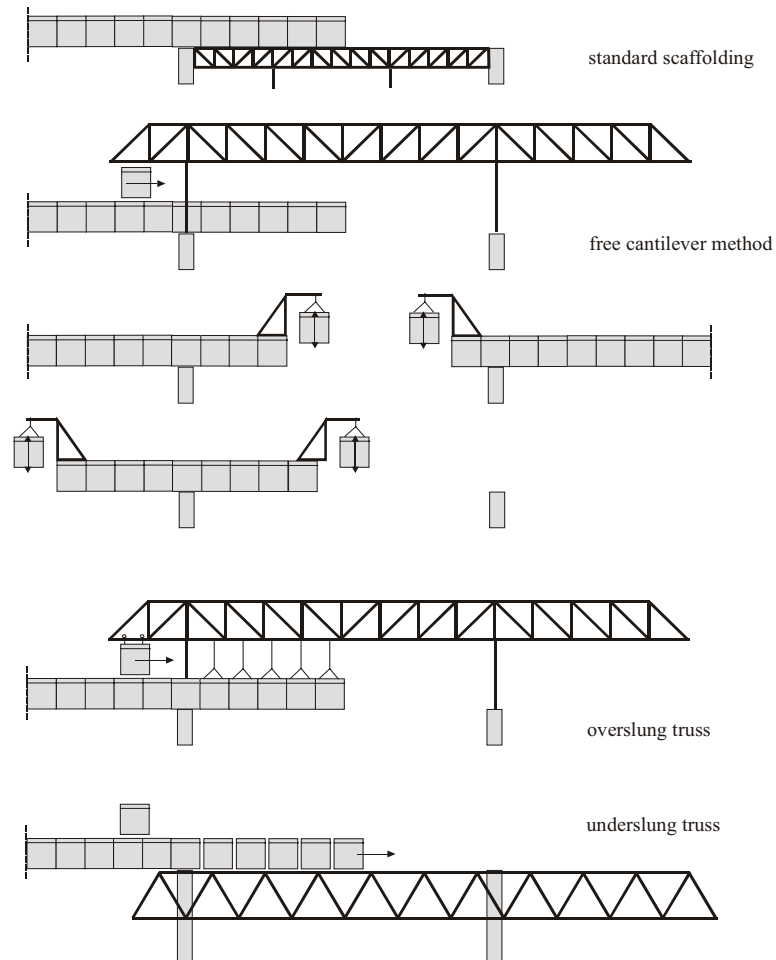


Figure 1.4 Construction methods

The term “balanced cantilever construction” describes phase construction of bridge superstructure. The construction starts from the piers cantilevering out to both sides in such a way that each phase is tied to the previous one by post tensioning tendons, incorporated to permanent structure, so that each base serves as a construction base for the following one [1a].

The progressive method, “the step-by-step erection” process is derived from cantilever construction, where segments are placed in a successive cantilever fashion. The construction starts at one end and proceeds continuously to the other

end. The method is valid for both precast and cast-in-place segments. This construction method has been used for the “Ile de Ré Bridge” [8, 9] in France. Due to excessive high cantilever bending moments the section has to be fixed over the permanent pier during construction. To reduce this load either a temporary bent or a temporary movable tower-stay assembly can be used. The cantilever method is mostly used for very long spans.

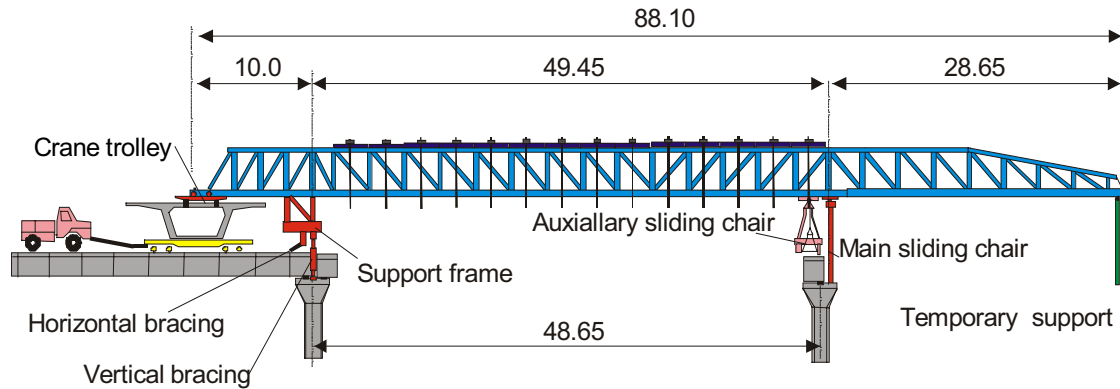


Figure 1.5 Span by span method of construction (overslung truss)



Figure 1.6 Segmental bridge constructions in Bangkok

For long viaducts, which have numerous, but relatively short spans ($l < 50$ m) the assembling of segments is mostly done by means of an erection girder over or under the superstructure. An overslung truss does not reduce the clearance underneath the construction and therefore the traffic is not disturbed (Fig. 1.6). It is more flexible than an underslung truss. It was initially developed as a cast-in-place method of construction on formwork. With the span by span method, the precast elements are placed and adjusted on a steel erection girder spanning from pier to pier, then post-tensioned together in one operation. Although both the cast-in-place and precast span-by-span construction methods continue to be used, precast segmental has become the method of choice for most applications [1a]. Further information about history and construction of segmental bridges can be read in references [10-12, 29, 41, 46, 57-58, 60-99].

1.1.3 Typical segmental hollow box girder bridge

Fig.1.7 shows the segmental bridge that had been constructed in Bangkok, Thailand [29]. This standard structure will be used as the reference structure for the numerical investigation. So, it will be described below in detail.



Figure 1.7 Standard span $l = 43.25$ m of the Second Stage Expressway (SES)

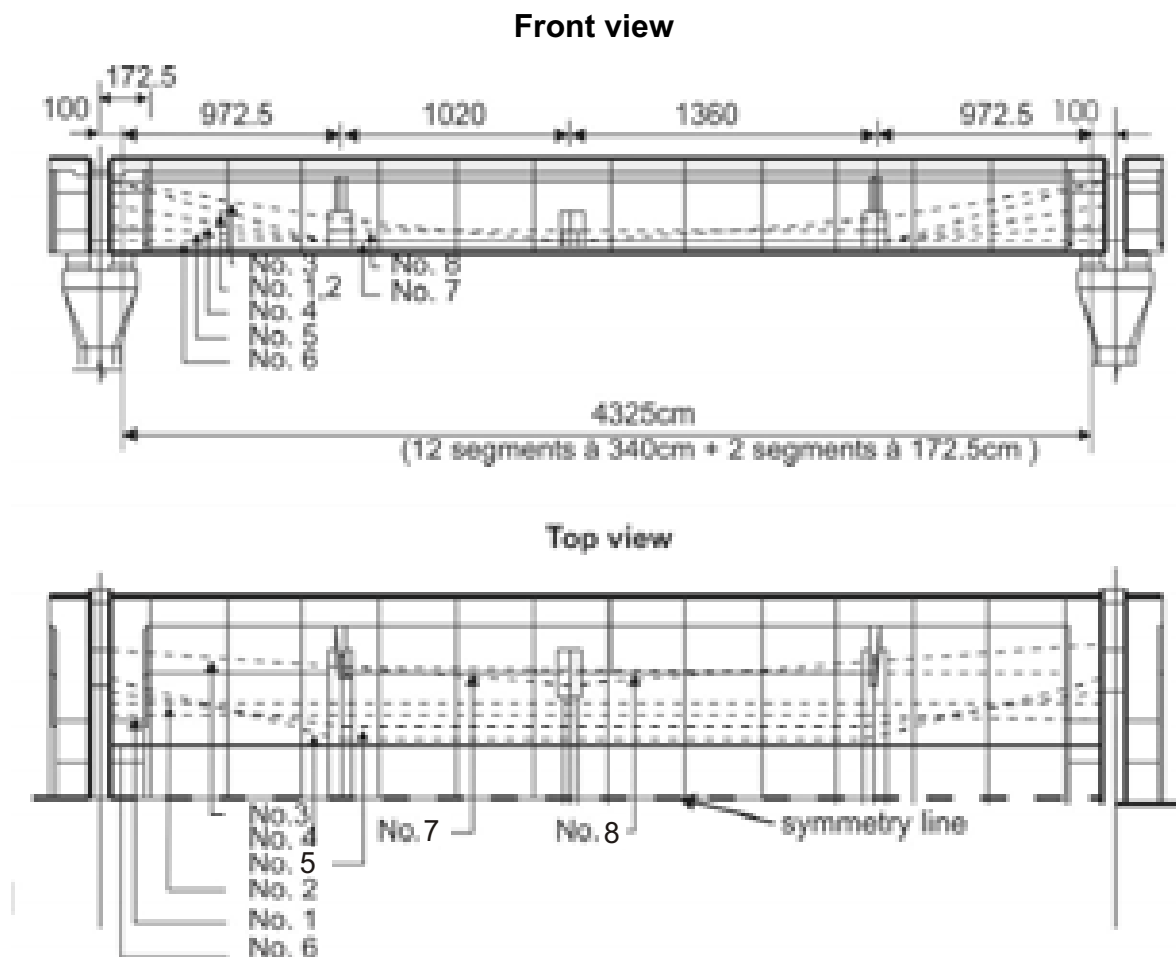


Figure 1.8 Tendon layout of a standard span segmental bridge (SES Bangkok)

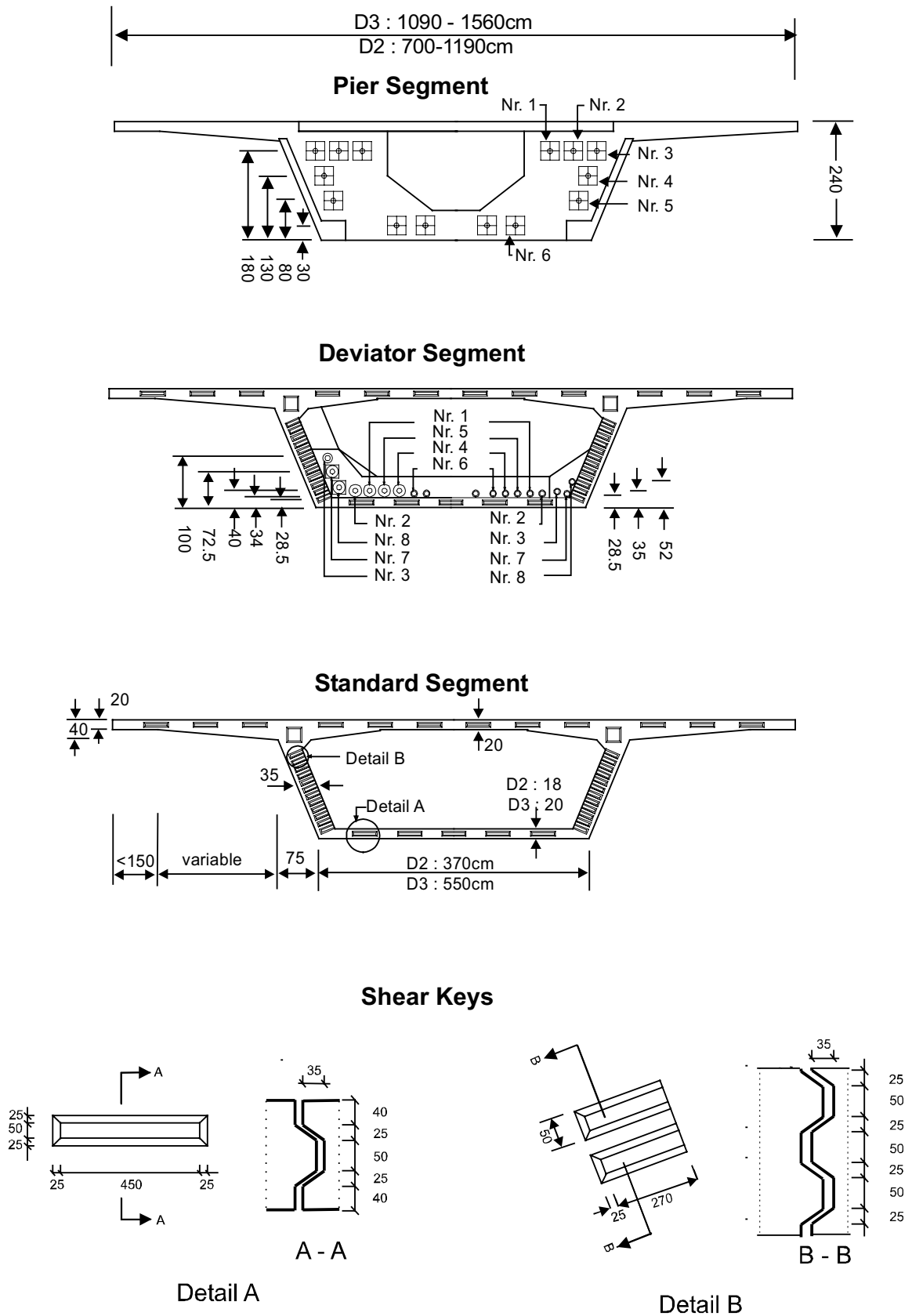


Figure 1.9 Segment types (SES Bangkok)

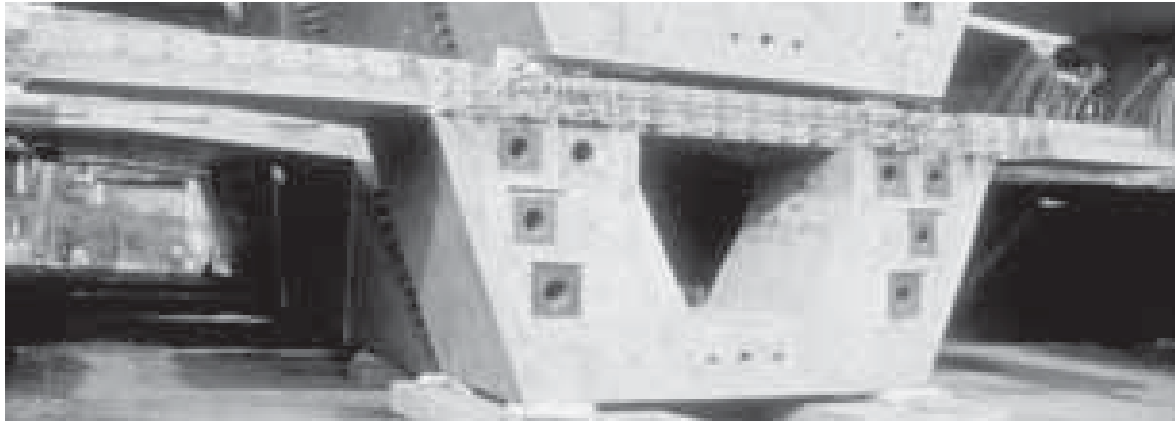


Figure 1.10 Pier segment

Segment types

Due to the external prestressing three different types of segments are required (Fig. 1.9, 1.10):

- ⚡ Pier segment: A thick diaphragm is needed to stiffen the webs for carrying the shear force to the bearings and for the anchorage of the external tendons. Eccentric forces must be considered since the tendons are not anchored directly to the webs.
- ⚡ Deviator segment: At this element the tendons are deviated. This results in high vertical forces, which have to be carried to the webs. The HDPE ducts are placed close to the web. This arrangement reduces the stresses at the bottom slab due to deviator forces. The minimum radius (R_{\min}) of curvature of tendon in this area has to be limited with regard to additional stresses and fatigue of the HDPE ducts. For normal tendon sizes it is approximately equal to 5 ÷ 6 m. Various types of deviators are being built (Fig. 1.11). Corbels are mostly used in the span whereas diaphragms are useful over the piers.
- ⚡ Standard segment: Neither tendon anchorage nor coupling is carried out. So, the thickness of the webs can be reduced to 35 cm or less depending on the shear force. This minimizes the dead load of the segment.

Shear keys are supposed to carry the shear forces at the joints and to assist the assemblage of the segments.

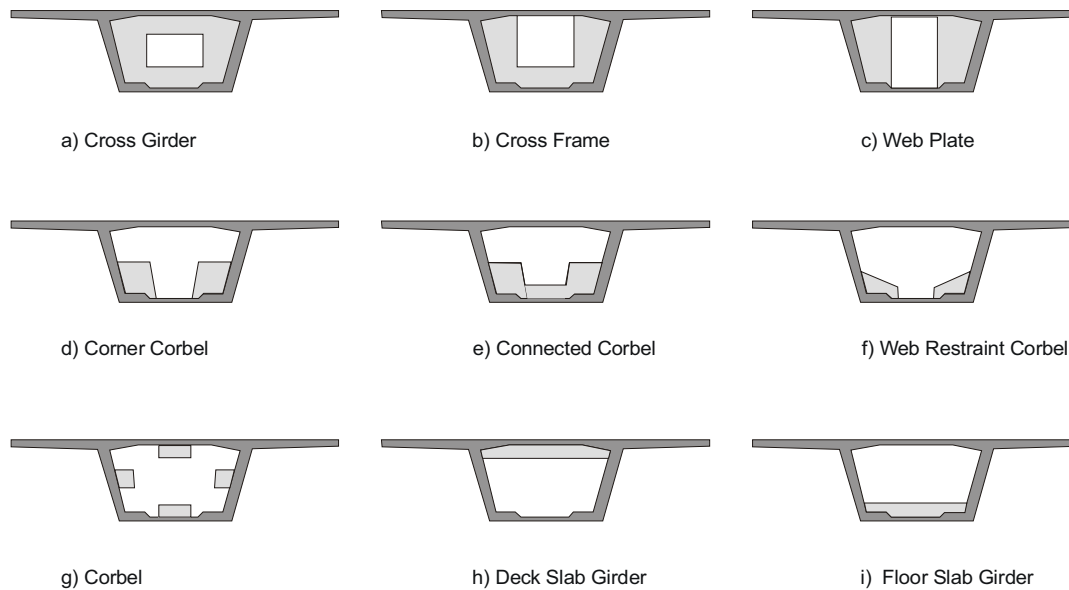


Figure 1.11 Different types of diaphragms and deviators [25]

1.2 Research objectives

The objectives of the research are as follows:

1. To analyse the stresses on the first joint

The unreinforced joints between the segments must always be under compression due to serviceability reasons. Field practice in some segmental bridge construction shows a small opening in the first joint on the flanges of the top slab. So far the distribution of stress in the first joint has not been investigated by scientific research. For this and other investigations a finite element model of the segmental bridge shown in figure 1.6 through 1.9 built up from 14 segments will be developed.

2. To investigate the load paths in the diaphragm

The investigation of force transfer in a diaphragm carried out by Wollmann [4] was based on simple beam theory. The location and magnitude of the resultant forces are obtained by integrating the stress distribution over respective areas. However the stress distribution in the pier segment is complex in nature (discontinuity region) and cracks are sometimes observed here. So simple beam theory, which is based on a linear stress distribution over the depth of the section, should not be applied here. As mentioned by Schlaich [3] “ At statical or geometrical

discontinuities such as point loads or frame corners, corbels, recesses, holes and other openings, the simple beam theory is not applicable.” To trace the complex load paths a three dimensional finite element model of a real pier segment will be developed.

3. To develop new strut-and-tie models for pier segments

The analytic tools that were used by former researchers are not as powerful as the ones available today. So, it is imperative to utilize modern technology to verify previously developed models. In this regard powerful finite element software called Ansys will be used to analyse various models with different boundary conditions and loadings. Finally the results will be compared with models of Schlaich and Wollmann.

1.3 Scope of this dissertation

Some background information for the development of strut-and-tie models, which is needed for the development of accurate models later in Chapter 6, will be given in Chapter 2. Further, the design of the anchorage zone is mentioned. The load paths in a diaphragm are studied in Chapter 3 by means of a plane finite element model. Elastic and inelastic finite element analysis of a shear wall for different loadings and boundary conditions are conducted. These simple plane FE-models are used in practice but in reality the stress distribution is more complex. Therefore a more realistic analysis with a 3-D finite element model of a real segmental bridge is conducted (Chapter 4). These calculations are further used to study the stress distribution in the first joint. A 3-D model of a pier segment with closed and open diaphragm is further used to study the flow of the prestressing force from the diaphragm to the webs and slabs (Chapter 5). In Chapter 6 more accurate strut-and-tied models are developed based on the investigations of Schlaich [3, 7] and Wollmann [4]. Chapter 7 summarizes the main results of the investigations and gives some conclusions.

2 Background information

Bernoulli (B-regions) theory is not applicable at statical or geometrical discontinuities (D-regions) such as point loads or frame corners, corbels, recesses, holes and other openings on structures. Therefore, in practice, procedures that are based on test results, simplified analytical methods and experience from the past are usually applied to cover such cases.

2.1 Strut-and-tie model

A rational approach to design discontinuity regions (D-regions) (Fig. 2.1) is based on truss or strut-and-tie models. Until now truss models were considered by researcher and field engineers as reasonable and appropriate basis for the design of cracked reinforced concrete loaded in bending, shear and torsion. Nevertheless, a design based on this method usually covers certain parts of structure.

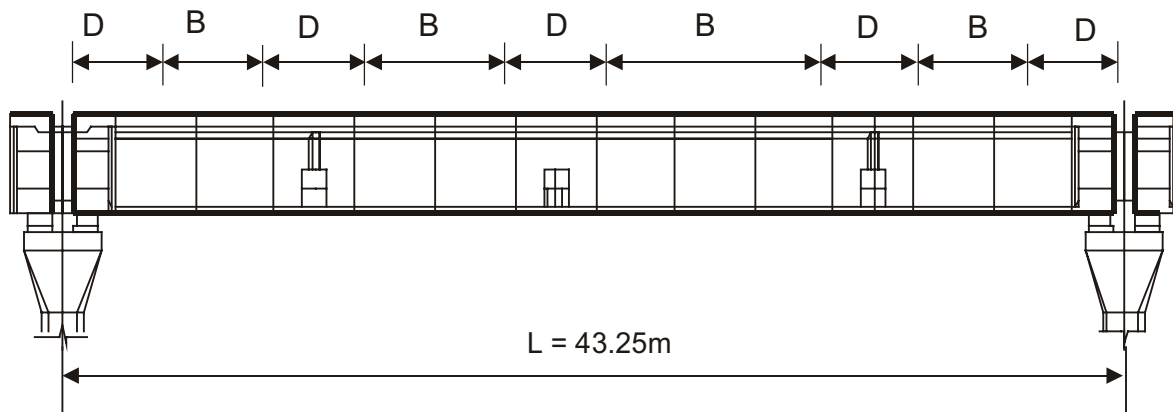


Figure 2.1 D-and-B regions in segmental bridge

Generally it is proposed to design structural concrete and every part of the structure by means of the truss analogy respectively strut-and-tie models. The truss analogy is explained in such a way that reinforced concrete structures carry load through a set of compressive stress fields which are distributed and interconnected by tensile ties. The reinforcing bars, prestressing tendons, or concrete tensile stress fields are considered as ties. It is assumed that the strut-and-tie models condense all stresses in straight compression and tension

members and join them by nodes for analysis. The strut-and-tie model can be developed by following the directions of the forces throughout a structure. To attain a consistent design approach for a structure, the tension and compression members (including their nodes) should be designed with regard to safety and serviceability by uniform design criteria.

Some of the advantages and disadvantages of strut-and-tie model are given below.

Advantages:

- ⚡ the tie forces in the strut-and-tie model can be converted into reinforcement requirements
- ⚡ the actual reinforcement arrangement is seen in the model
- ⚡ strut-and-tie models direct the attention to global load paths
- ⚡ the nodal concept emphasises good detailing
- ⚡ strut-and-tie models can be calculated by hand

Disadvantages:

- ⚡ the concrete tensile strength is neglected (mostly)
- ⚡ development of a strut-and-tie model requires experience
- ⚡ effective concrete compressive strength is selected arbitrarily and is affected by a large number of variables
- ⚡ there is no unique strut-and-tie model solution. This is particularly true for refined models, but is not the case for basic strut-and-tie models. A suitable strut-and tie model is selected by engineering judgement
- ⚡ It requires high ability to visualize spatial relationships
- ⚡ can be used for design of ultimate limit state only, serviceability (crack width) is not considered
- ⚡ load superposition is usually not possible
- ⚡ automatic generation of the truss model by computer programs is only possible in simple cases

2.2 Structure's B- and-D regions

The regions of a structure, in which the Bernoulli hypothesis of a plane strain distribution over the section depth is assumed to be valid, are usually designed with high care and accuracy by standard methods. These regions are named as B-regions (where B stands for Bernoulli). Their internal state of stress is easily derived from the sectional forces (bending and torsional moments, shear and axial force).

For uncracked sections, these stresses are calculated with help of sectional properties like cross sectional areas and moments of inertia. If tensile stresses exceed the tensile strength of concrete, the truss model or its variations apply.

The above methods are not applicable to all other regions where the strain distribution is significantly non-linear, e.g. near concentrated loads, corners, bends, openings and other discontinuities (Fig. 2.2). Such regions are called D-regions (where D stands for discontinuity).

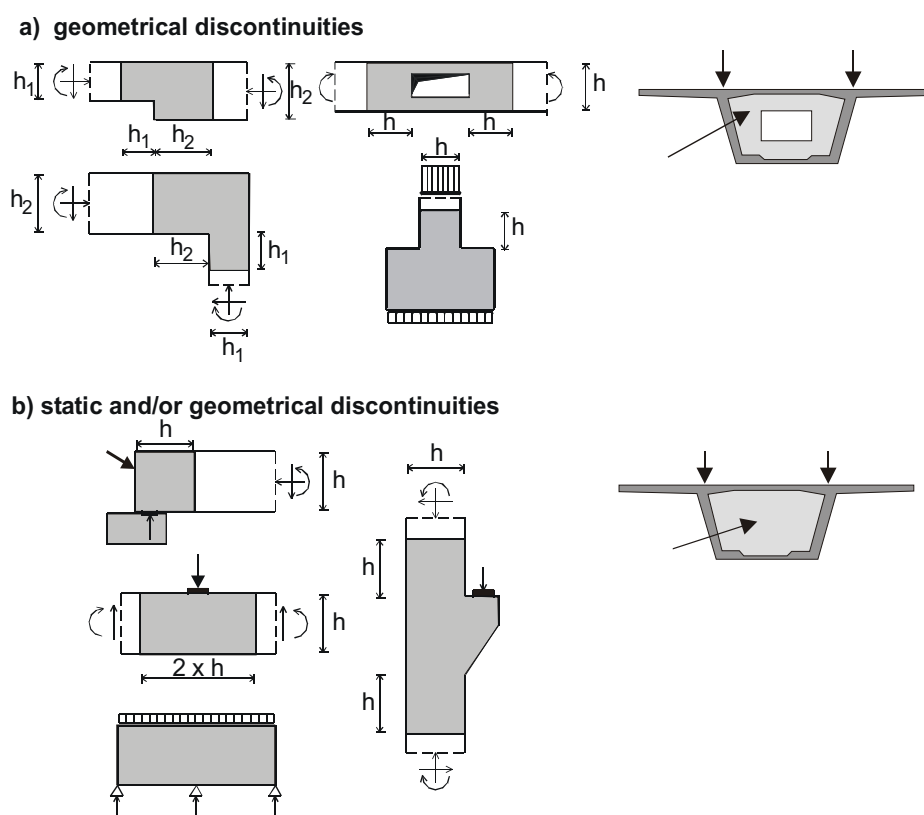


Figure 2.2 D-regions (shaded areas) with non-linear strain distribution

Stress and strain trajectories have smooth patterns in B-regions as compared with their turbulent nature in D-regions (Fig. 2.3). Stress intensities decrease quickly with the distance from the origin of the stress concentration. This behaviour allows the identification of B- and D-regions in a structure.

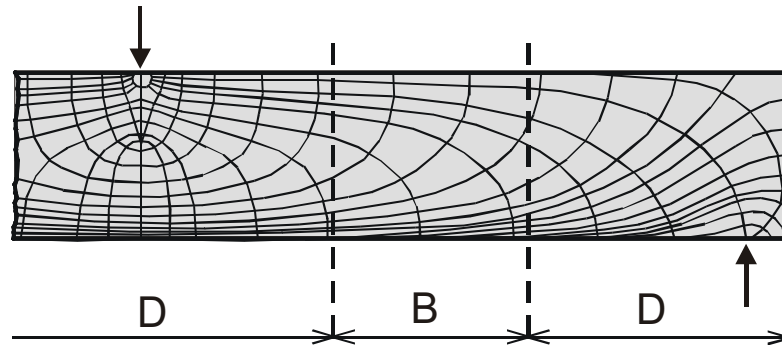


Figure 2.3 Stress trajectories in a B-region and near D-regions [3]

2.3 General design procedure and modeling

The dimensioning of B-regions of the structures can be carried out by the standard B-region models (e.g. the truss model) or standard methods using handbooks or an advanced code of practice. The internal forces at the boundaries of the D-regions are calculated from overall structural analysis and B-region design.

Table 2.1 Analysis leading to stresses or strut-and-tie forces [3]

Structure		Structure consisting of:		
		B- and-D-regions e.g. linear structures, slabs and shell		D-regions only e.g. deep beams
		B-regions	D-regions	D-regions
Analysis		Sectional effects	Boundary forces:	
Overall structural analysis (Table 2) gives		M, N, V, M_T	Sectional effects	Support reactions
Analysis of inner forces or stresses in individ. regions.	State I (uncracked)	Via sectional values A, J	Linear elastic analysis * (with redistributed stress peaks)	
	State II (cracked)	Strut-and-tie-models and /or non-linear stress analysis*		
		Usually truss		

* May be combined with overall analysis

Table 2.2 Overall structural behaviour and method of overall structural analysis of statically indeterminate structures [3]

Limit state	Overall structural behaviour	Corresponding method of analysis of sectional effects and support reactions	
		Most adequate	Acceptable
Serviceability	Essentially uncracked	Linear elastic	-
	Considerably cracked with steel stresses below yield	Nonlinear	Linear elastic (or plastic if design is oriented at elastic behaviour)
Ultimate capacity	Widely cracked, forming plastic hinges	Plastic with limited rotational capacity or elastic with redistribution	Linear elastic or non-linear or perfectly plastic with structural restrictions

In deep beams where the member consists of only one region (D-region), the inner forces or stresses can be determined directly from the applied loads following the principles outlined for D-regions in section 2.4. For statically indeterminate structures however, the support reactions have to be calculated by an overall analysis before the development of strut-and-tie models.

In some cases a non-linear finite element analysis can be applied, but it is difficult to model reinforcement realistically in FEM analysis, so a follow up check with strut-and-tie models is recommended.

2.4 Modeling of individual B- and-D regions

2.4.1 Principles and general design procedures

Standard methods are available for the analysis of the concrete and steel stresses for uncracked B- and D- regions. (Tab.2.1). The elastic linear stress-strain relation may have to be modified by replacing hook's law with a non-linear material behaviour for high compressive stresses (Fig. 2.4).

If the tensile stresses in individual B or D-regions exceeds the tensile strength of the concrete (f_{ct}) the section will likely crack. According to the German Code

For cracked B-regions, the proposed procedure obviously leads to a truss model with inclination of the diagonal struts that are in the direction of the diagonal cracks.

For the D-regions it is necessary to develop a strut-and-tie model for each load case individually. Developing the model in a D-region is more simplified if the elastic stress and principal stress direction are available, e.g. by an elastic finite element analysis, as shown in Fig. 2.5.

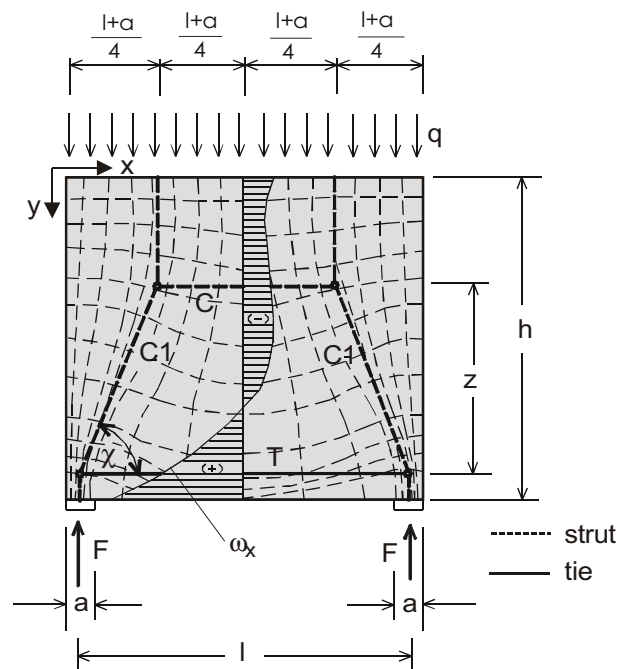


Figure 2.5 Deep beam - a typical D-region elastic stress trajectories, elastic stresses and strut-and-tie model [3]

2.4.2 The load path method

First, all loads and support reactions must be determined to satisfy outer equilibrium of the D-region. For D-regions, the loads are taken from adjacent B-region designs, assuming that a linear distribution of stresses (ω) exists as in the Fig. 2.6 and (q) in Fig. 2.7.

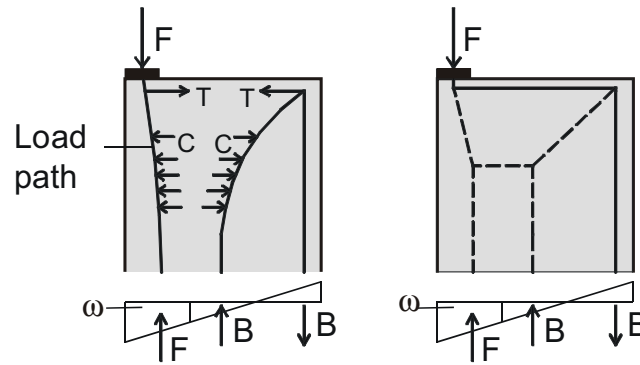


Figure 2.6 Load paths (including a “U-turn”) and strut-and-tie model [3]

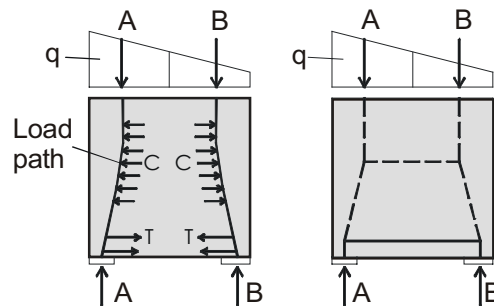


Figure 2.7 Load paths and strut-and-tie model [3]

The stress distribution is subdivided in such a way that the loads on one side of the structure find their counterpart on the other. The load paths connecting the other side start and end at the centre of gravity of the corresponding stress diagrams and have there the direction of applied loads and reactions. They tend to take the shortest possible pathway in the region. Stress concentrations (support reactions and singular forces) are observed near curvatures.

There are some cases where the stress diagram is not completely used up with the load paths as described; it shows a path that is equal in magnitude but with an opposite sign, which enters and leave the structure as a U-turn illustrated by force *B* in Figs. 2.6 & 2.8b.

In the above case, only equilibrium in the direction of the applied loads has been considered. After completing the sketch of all the load paths with smooth curved

polygon, the struts and ties must be added as transverse equilibrium acting between nodes, including those of the U-turn.

Proper attention should be given however, for tie forces that seek practical arrangement of reinforcement details (generally parallel to the concrete surface) and of crack distribution requirements.

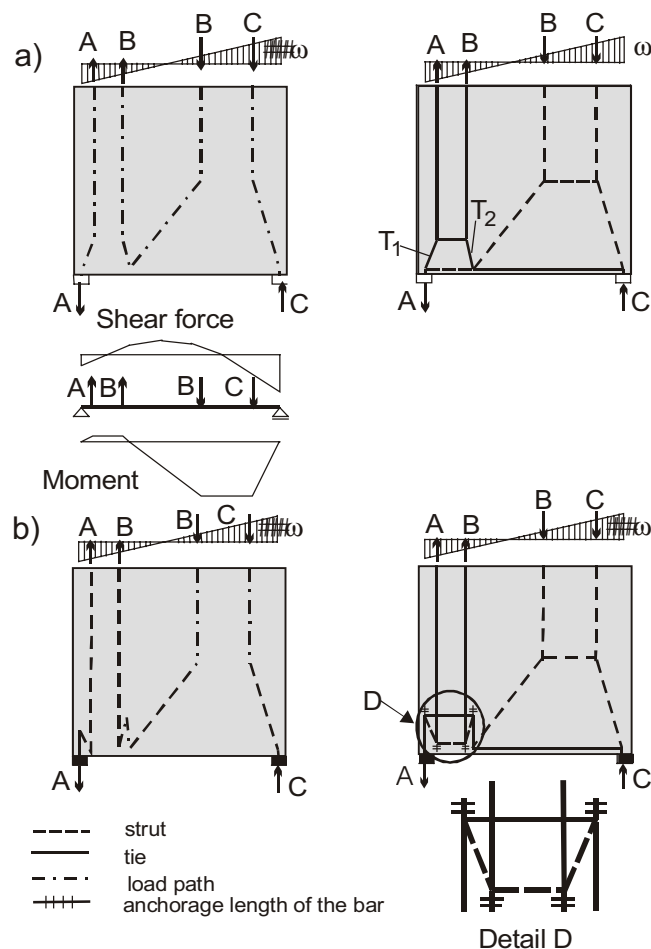


Figure 2.8 Two models for the same load case: (a) requiring oblique reinforcement; (b) for orthogonal reinforcement [3]

A very powerful tool to develop new strut-and-tie model for complicated cases is the combination of an elastic finite element analysis with the load path method. This combined approach is applied in Figures 2.9. & 2.10.

In Fig. 2.9 the vertical stress and ties are found by the load path method, and as in previous cases the structure is divided into a B-region and a D-region. The lower part of the D-region is loaded by the stresses (ω) from the adjacent B-region.

These stresses are then resolved into four components; the two compressive forces $C_3 + C_4 = F$, which gives two equal forces T_2 and C_2 . By adjusting the vertical load components in its appropriate locations, transverse stresses are generated.

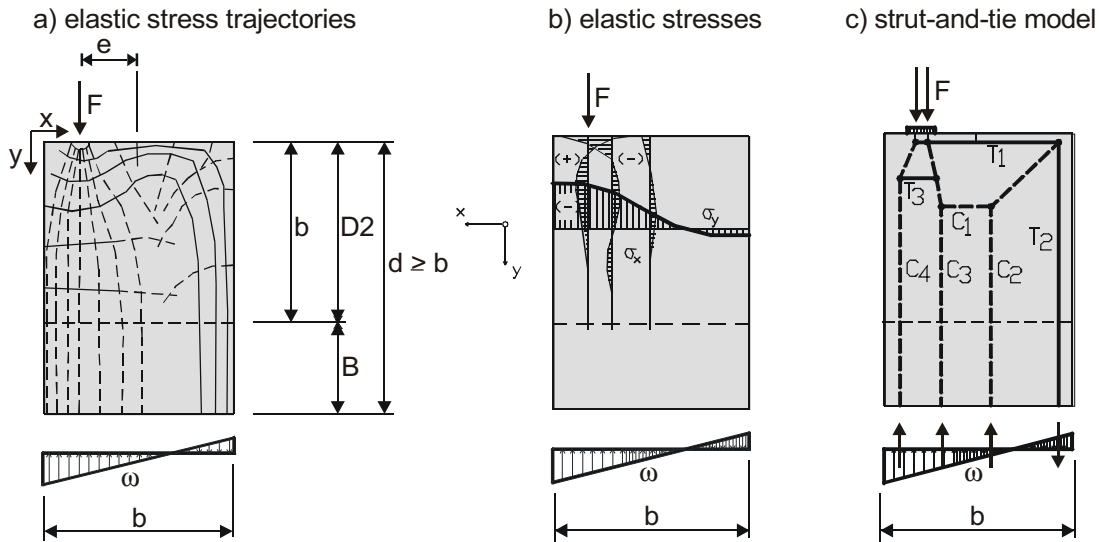


Figure 2.9 A typical D-region [3]

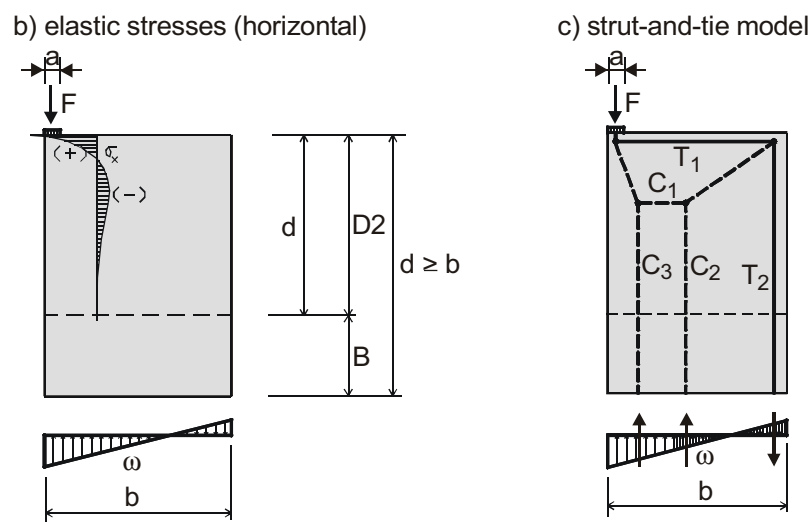


Figure 2.10 Special case of the D-region in Fig. 2.9 with the load at the corner [3]

The corresponding horizontal struts and ties are located at the centre of gravity of stress diagrams in given structures, which are derived from an elastic analysis (Fig. 2.9b). The nodes from the vertical struts also determine the position of the diagonal struts (Fig. 2.9c). The example in Fig. 2.10 shows that the tie T_3 of the

Fig. 2.9c disappears, if the load F moves towards the left and right upper corner of the D-region.

To develop strut-and-tie models a set of rules shown in table 2.3 should be followed. By applying the rules of this table, it is possible to develop basic and refined strut-and-tie models. The basic load path satisfies only equilibrium conditions and material strength limitations. They represent a lower bound solution to the failure load for a structure made of perfectly plastic material. Reinforced concrete is not however, a perfectly plastic material, so some improvement must be made to its limited ductility. This is carried out by rules 3 to 6 in table 2.3, which satisfy compatibility requirements in the strut-and-tie model. Rules 7 and 8 are applied to cracked concrete: tensile forces are carried by reinforcement (rule 7), and load paths in compression are stiffer than load path in tension (rule 8) (Fig. 2.11). By applying rules 3 to 8, the actual state of stress in the structure is better approximated by the strut-and-tie model and the procedure is more independent from the assumption of perfectly plastic material.

Table 2.3 Rules for the development of strut-and-tie models (STM) [4]

Rule	Requirements	
1	Satisfy equilibrium conditions	basic STM
2	Satisfy material strength limitations	
3	Satisfy simple beam theory at the boundaries of the D-region (anchorage zone)	refined STM
4	Select angle between struts and ties larger than 25 degrees	
5	Orient the geometry of the strut-and-tie model on the linear-elastic stress trajectories	
6	Split struts carrying large compression forces into a number of sub-struts.	
7	Keep practical reinforcement arrangements in the mind when selecting the orientation of the ties	
8	Avoid inefficient load paths	

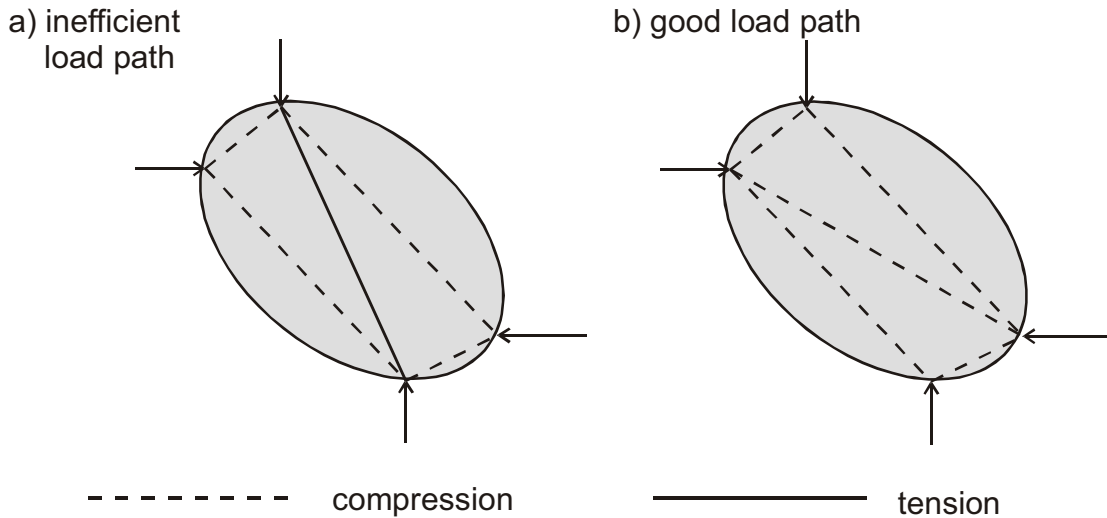


Figure 2.11 Efficient and inefficient load paths in strut-and-tie models [4]

2.4.3 Model selection

Several different strut-and-tie models can be found for one load case as shown in Fig. 2.8 for a deep beam. However criteria's have to be found to select the most appropriate model for design. The left part of Figs. 2.8a and 2.8b shows how they were connected to the overall sectional effects of the D-regions. The practical arrangement of reinforcement for ties T_1 and T_2 in Fig. 2.8a would be difficult because it requires inclined reinforcement. So, from the practical point of view, a tie arrangement as shown in Fig. 2.8b that can be satisfied by an orthogonal reinforcement is a better solution.

Another criterion for optimising and selecting a suitable strut-and-tie model is the principle of minimum strain energy. Since the strains in the struts are usually much smaller than those in the ties, the concrete struts can be neglected. This results in the following criterion:

$$\sum_i F_i l_i \epsilon_{mi} \mid \text{Minimum} \dots\dots\dots (2.1)$$

- Where: F_i = force in strut or tie i
 l_i = length of member i
 ϵ_{mi} = mean strain of member i

It should be kept in mind that representing a continuous structure by individual straight lines is an approximation in itself and so, it opens the chance for selection of different models. Also, individual input such as the size of the strut, tie or nodes is always different. An engineer with some experience in strut-and-tie modelling however will always find a satisfactory solution.

2.5 Dimensioning of struts, ties and nodes

2.5.1 Definitions and general rule

Dimensioning is sizing and reinforcing the individual struts and ties for the forces they carry and also ensuring the load transfer between them by checking the node regions. Nodes are parts of strut-and-tie models where the compression and/or tension members meet each other. The flow of force in the nodal region is greatly affected by details of the node chosen. Therefore, it is necessary to check whether the strut-and-tie model chosen initially is still valid after detailing or needs correction. Thus, modelling and dimensioning is in principle an iterative process.

There are basically three types of struts and ties to be dimensioned:

- C_c Concrete struts in compression
- T_c Concrete ties in tension without reinforcement
- T_s Ties in tension with reinforcement (mild steel reinforcement or prestressing steel)

There are essentially four types of nodes depending on the combination of the struts C and ties T (Fig. 2.12).

- CCC-nodes (compression – compression – compression nodes)
- CCT-nodes (compression – compression – tension nodes)
- CTT-nodes (compression – tension – tension nodes)
- TTT-nodes (tension – tension – tension nodes)

The principle remains the same if more than three struts and ties meet.

2.5.2 Struts and ties

The struts in the model are resultant of the stress fields and are considered as straight. All the curvatures or deviations of the forces are assumed to be concentrated in the nodes. This is indeed an idealization of the reality. By doing

so, doubts can arise whether in a highly stressed structure some tensile forces are sufficiently considered. The straight lengths of the struts can be reduced either by refining the model itself or by smearing (spreading) the node over a substantial length of the strut (Fig. 2.12).

Strut-and-tie model, stress fields and corresponding reinforcements are shown below.

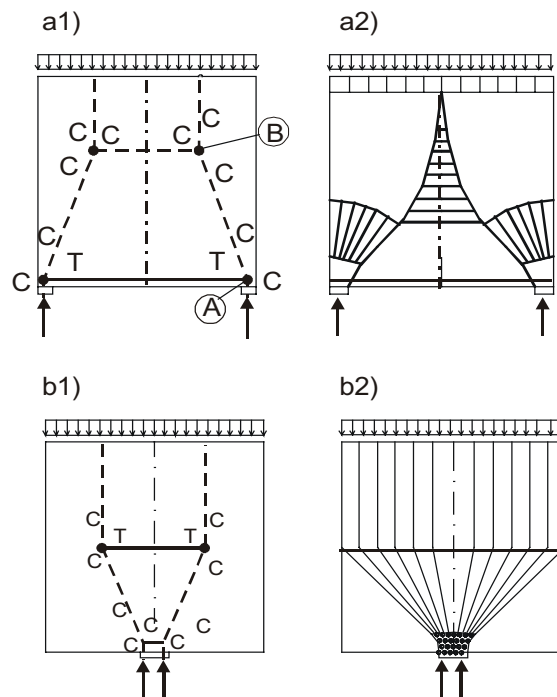


Figure 2.12 a1) and b1) Strut-and-tie models, nodes and corresponding reinforcement a2) and b2) their stress fields [3]

To cover all cases of compression fields including those of the B-regions, three typical configurations are sufficient (Fig. 2.13):

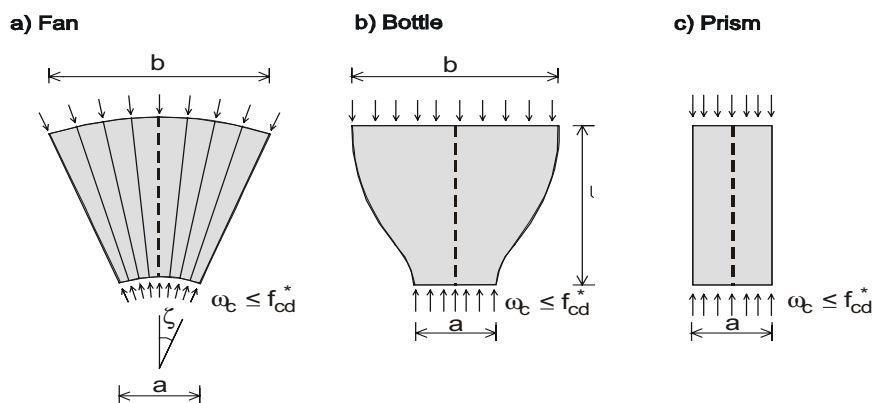


Figure 2.13 The basic compression fields [3]

For practical purposes, the following simplified strength values of allowable compressive stress f_{cd}^* are proposed for dimensioning all types of struts and nodes:

$f_{cd}^* | 1.0f_{cd}$: for undistributed and uniaxial state of compressive stress as shown
in Fig. 2.13c

$f_{cd}^* | 0.8f_{cd}$:if tensile strains in the cross direction or transverse tensile reinforcement may cause cracking parallel to the strut with normal crack width

$f_{cd}^* | 0.6f_{cd}$:as above for skew cracking or skew reinforcement

$f_{cd}^* | 0.4f_{cd}$:for skew cracks with extraordinary crack width

Compressive stress α_c is checked in the nodes and tie forces are covered by reinforcement.

2.5.3 Nodes

The nodes are defined as the intersection points of three or more straight struts or ties, which in turn represent either straight or curved stress fields or reinforcing bars or tendons. There is an abrupt change in the direction of force at the node. In the actual reinforced concrete structure the deviation covers a certain length and width. The deviation of forces tends to be locally concentrated, if the struts or ties represent a concentrated stress field. Also, the deviation of force is considered to be smeared (spread) over some length, if wide concrete stress fields join each other or with tensile ties that consist of closely distributed reinforcing bars. Thus, in the former case the nodes are called singular (concentrated) nodes, whereas in the latter case they are called smeared (continuous) nodes. Nodes A and B in Fig. 2.12a1 serve as typical examples of both types of nodes.

2.6 Design of diaphragms in bridges and shear walls

Several figures are provided which gives examples of diaphragm areas (Fig. 2.14). Schlaich et. al. [7] state that diaphragms with tendon anchorages are variation of the deep beam problem.

2.6.1 Shear wall with central support – shear loading

Fig. 2.14. shows a prestressed diaphragm of a bridge with one centric bearing. The shear force V_1 carried by the diagonal strut C_1 in the webs of the box girder (Fig. 2.14a) are in this case transferred to central support via prestressed web reinforcement. Mild reinforcement can be used if the tension force T_1 is not too big. According to Schlaich et. al. [3] the following equations can be used to estimate the tension forces:

$$T_1 \approx V_1 / \sin \chi^\circ \approx 1.01 V_1 \dots\dots\dots (2.2)$$

$$T_2 \approx 0.82 \sqrt{2} \sqrt{V_1} \dots\dots\dots (2.3)$$

Please note that equation (2.3) is only a rough approximation because T_2 depends on the geometry of the shear wall. More ‘accurate’ values may be calculated from the strut-and-tie model (Fig. 2.14).

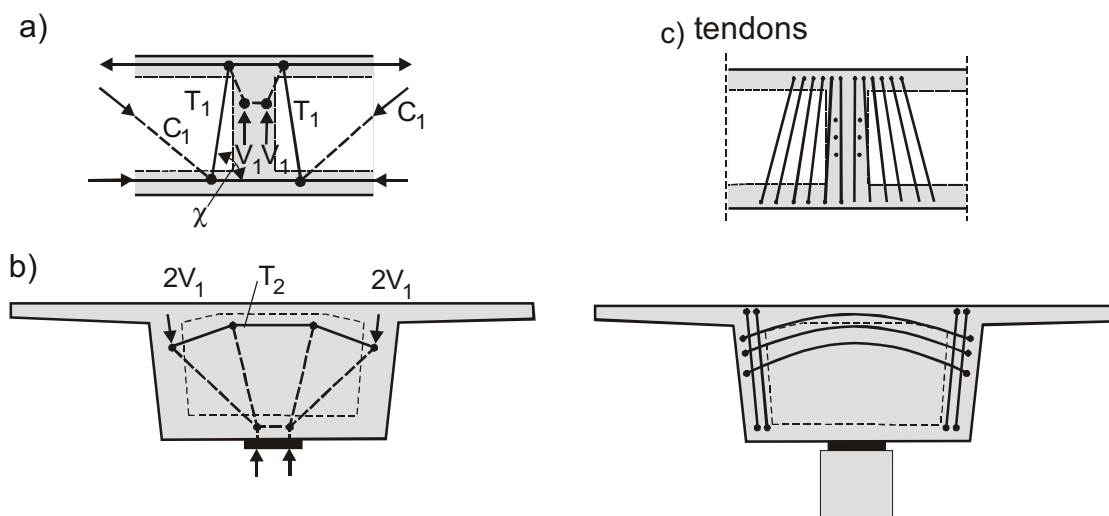


Figure 2.14 Diaphragm strut-and-tie models [7]

2.6.2 Shear wall with two supports and without opening

In the strut-and-tie model shown in figure 2.15 Schlaich assumes that the resultant shear force almost acts at the mid height of the web and thus compression struts flow directly to the supports. Also, the flow of forces caused by a torsional moment is shown. This model will be verified in Chapter 3. The following relations are given to evaluate the forces:

Over all support reaction $A = V$ (equilibrium)

Reaction due to V : $V_v \mid \frac{A}{2 \beta h}$ (force per length)..... (2.4)

Reaction due to T : $V_t = \frac{M_t}{2 A_k} \mid \frac{M_t}{2 \beta_o 2 b_u \beta h}$ (force per length)..... (2.5)

Tie force: $T_1 - V_t \beta_o$ (2.6)

$$T_2 - V_t \left(\frac{2 \beta_o h}{b_o 2 b_u} \right) \dots\dots\dots (2.7)$$

A check for concrete compressive stresses should be conducted at the supports.

The relation is given by:

$$\omega_{max} \mid \frac{V/2 + M_t/2b_u}{A_b} \dots\dots\dots (2.8)$$

Where A_b is the area of the bearing.

Further the tension ties have to be designed.

Reinforcement: $reqA_{s1} \mid \frac{T_1}{\omega_s}$ and $reqA_{s2} \mid \frac{T_2}{\omega_s}$ (2.9)

$\omega_s \{ f_{yd}$ due to crack width requirement.

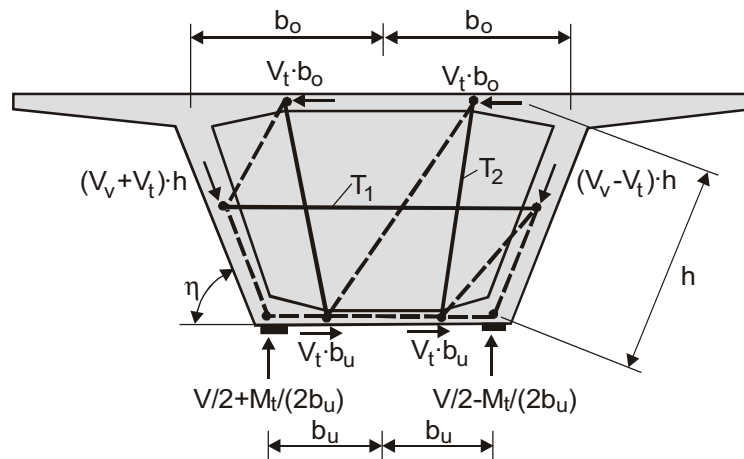


Figure 2.15 Diaphragm strut-and-tie model for shear and torsional moment [7]

2.6.3 Shear wall with two supports and opening under pure shear

The following equations are given to calculate the internal forces and stresses of a diaphragm under pure shear.

The overall support reaction F_b is equal to the shear force V (equilibrium)

$$\text{Forces in terms of } V: V_v \mid \frac{F_b}{2} \frac{h}{h} \dots\dots\dots (2.10)$$

$$\text{Tie forces: } T_1 - F_b \left(\frac{a}{h_1} \frac{2}{2} \frac{c}{h_2} \right) \dots\dots\dots (2.11)$$

$$T_2 - F_b \left(\frac{2a}{h_1} \frac{4c}{h_2} \right) \dots\dots\dots (2.12)$$

The concrete compressive stresses should be checked at the supports.

$$\text{For maximum compressive stress: } \omega_{max} \mid \frac{F_b / 2}{A_b} \dots\dots\dots (2.13)$$

$$\text{For tension reinforcement: } A_{s1} \mid \frac{T_1}{\omega_s} \text{ resp. } A_{s2} \mid \frac{T_2}{\omega_s} \dots\dots\dots (2.14)$$

- Where: A_b is an area of concrete in contact with support
- c is width of bearing plate
- a is the distance from the web centre to mid of the bearing plate

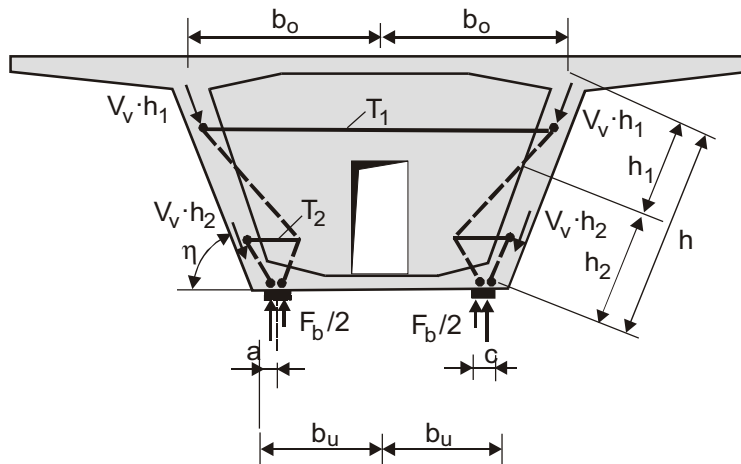


Figure 2.16 Strut-and-tie model of diaphragm with opening under pure shear [7]

The location of the horizontal tie T_1 in Fig. 2.16 is based on engineering practice and has not been checked so far. As the forces in any strut-and-tie model are dependent from the geometry of the truss model, FE-analysis will be conducted (chapter 4) to verify this assumption.

2.7 Strut-and-tie model for anchorage regions

It is relatively easy to guess the flow of force and to develop strut-and-tie models in two-dimensional problems. For simple structures and loadings, considering a sufficient number of two dimensional sub models can solve the problems in a three-dimensional member. The complex geometry (3-D) of the diaphragm however, requires a spatial strut-and-tie model. This increases its complexity and makes it more difficult to find a close solution that matches the finite element result in reality.

Nevertheless, based on engineering practice and numerical analysis the load paths in three-dimensional end diaphragms can be simplified by accurate strut-and-tie models [4]. These load paths, which will be described in the following sections, are called tripod model, corbel action, and frame action. They are used to model the flow of forces in a diaphragm loaded by external anchorage forces.

2.7.1 The tripod model

Fig. 2.17 below shows a load path where the anchorage force P is resisted by three inclined struts. Deep beam action generates the tensile force T_1 . Additional tensile forces (T_2 , T_3) are required across the flange-web corners for equilibrium.

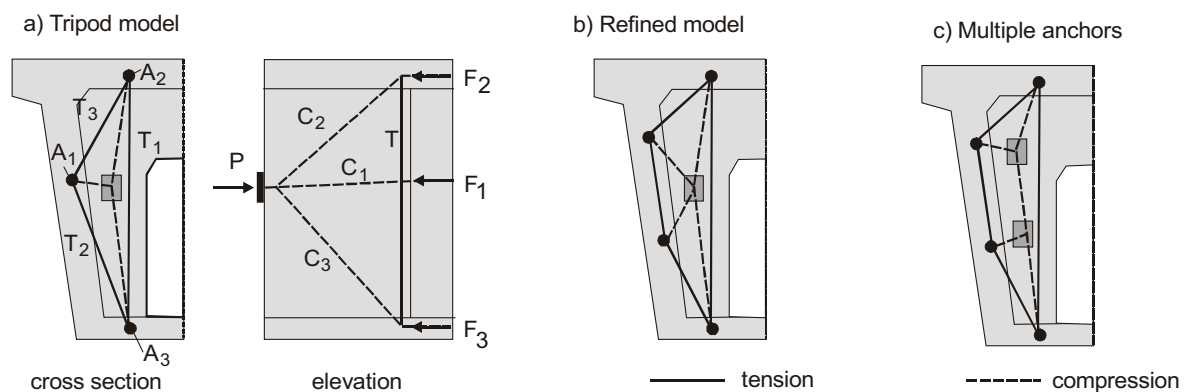


Figure 2.17 Tripod models [4]

The tensile force T_1 requires nodes in the flanges of the cross section (nodes A_2 and A_3) (Fig. 2.17a). Therefore, reinforcement provided to resist this tensile force must be anchored into the flanges. A more refined strut-and-tie model is necessary to capture the bursting force in the web (Fig. 2.17b). If several anchor forces act on the diaphragm, either individual tripod models can be superimposed or an overall strut-and-tie model can be developed (Fig. 2.17c). It should be noted that each tendon is stressed separately.

2.7.2 Corbel action

The transfer of the force from the diaphragm into the web is illustrated by the corbel action (Fig. 2.18). The load path shown in Fig. 2.18a must be completed to satisfy equilibrium conditions. The tripod model discussed in section 2.7.1 does not capture corbel action.

In columns the effect of a corbel is to introduce a bending moment into the column as shown in Fig. 2.18b. The corresponding effect in a diaphragm section is bending of the web in its thin direction. This bending moment is subsequently transferred to the flanges. An alternative and more efficient load path is shown in Fig. 2.18c. The deviation force C_1 and C_2 at levels 1 and 2 in Fig. 2.18a are transferred by vertical trusses to the flanges (truss 1 at level 1, truss 2 at level 2).

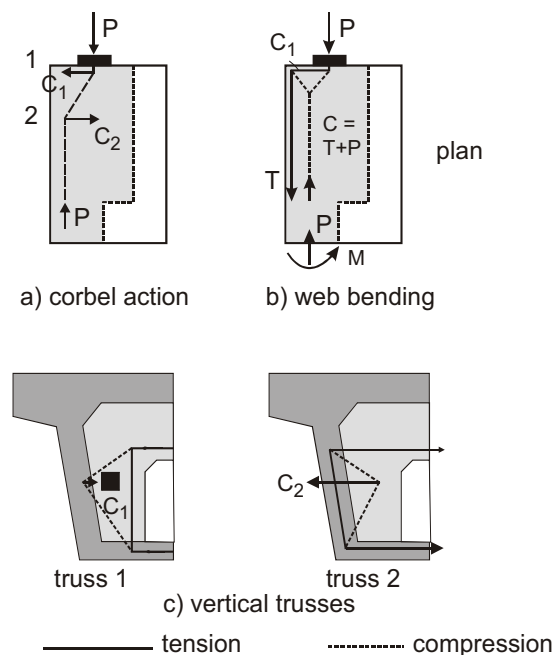


Figure 2.18 Corbel action [4]

2.7.3 Frame action

The transverse components of forces C_1 , C_2 , and C_3 (Fig. 2.17) are carried by frame action of the flanges and webs ahead of the diaphragm and are shown in Fig. 2.19. This load path is not as stiff as other load paths available. So, small portion of transverse tensile forces will be carried by frame action. However, it does explain cracks along the flange-web intersection ahead of the diaphragm, which were observed in the bridge structure of Washington D.C.'s rapid transit system [12, 26].

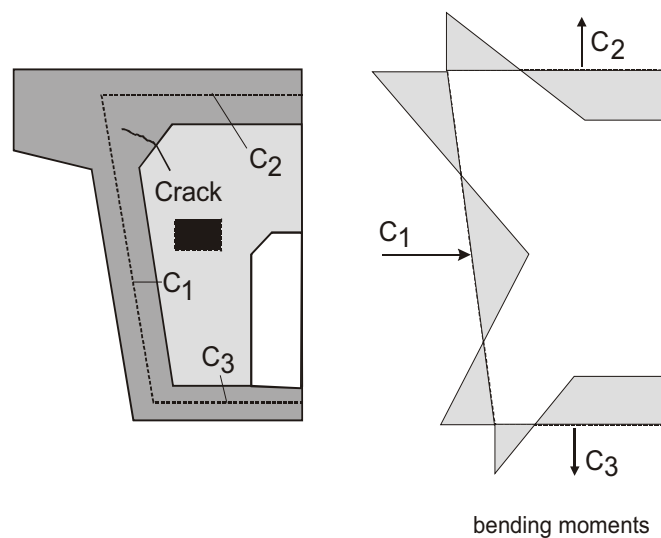


Figure 2.19 Frame action [4]

2.7.4 Extent of the D-region

The extent of the D-region can be taken as approximately equal to the largest cross-sectional dimension ahead of the end of diaphragm according to the hypothesis of St. Venant. The introduction of tendon force and geometric discontinuities results in the disturbance of axial-flexure stress in a D region.

To determine the location of nodes A_1 , A_2 , and A_3 in Fig. 2.17, some help can be obtained from the following considerations. Spreading of the forces in the flanges and web can only occur after these forces actually reach them. Before this spreading, only the part of the cross-section immediately adjacent to the

diaphragm is effective in carrying the anchorage force (hatched area in Fig. 2.20). However the exact locations of nodes were not determined by Wollmann.

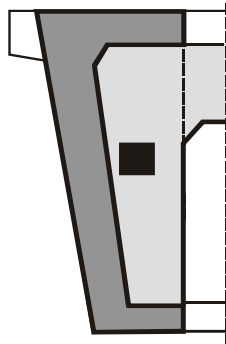
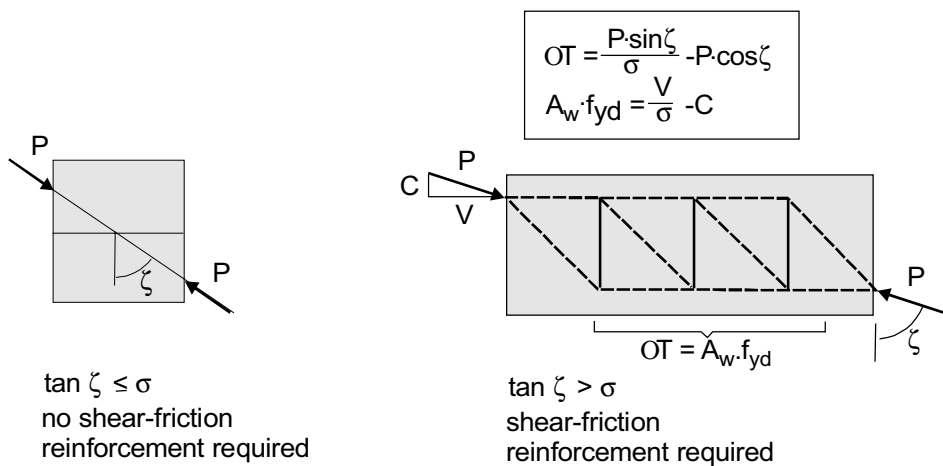


Figure 2.20 Effective cross-section ahead of diaphragm [4, Fig. 5.2]

2.7.5 Shear-friction

Shear transfer and transfer of forces in shear friction between diaphragm and adjacent web result in large inclined tensile stresses at the interface of the diaphragm and flanges. While developing strut-and-tie models the effects from shear-friction can be determined by limiting the angle ζ between compression struts and the direction normal to the critical section for shear friction (Fig. 2.21). AASHTO provides values for the coefficient of friction $\sigma = 1.4$ for monolithically placed, normal-strength concrete. If $\tan \zeta > \sigma$, shear-friction reinforcement is required. Fig. 2.21 shows a strut-and-tie model that satisfies shear-friction requirements.



EC2 has a different approach to the problem; the shear design value for monolithic joints is calculated according to EC 2 Part 1-3, equation 4.190:

$$v_{Rdj} = k_T \cdot v_{Rd} \cdot \sigma \cdot \omega_N \cdot 2 \cdot \psi \cdot (f_{yd} / \sigma) \cdot (\sin \zeta + 2 \cos \zeta) \cdot \Omega \cdot 0.5 \cdot f_{cd} \quad (2.15)$$

Where:

$k_T = 2.5$ factor for monolithically connected joints

v_{Rd} design value of shear strength according table 4.116 EC 2 Part 1-3
(i.e. $v_{Rd} = 0,34 \text{ MPa}$ for $f_{ck} = 30 \text{ MPa}$)

$\sigma = 1$ coefficient of shear friction (monolithically connected joints)

$\omega_N = \Omega \cdot 0.6 \cdot (f_{cd} / f_{ck})$ stress due to external forces on the joints, positive for compression and negative for tension (with $f_{cd} = f_{ck} / v_c$)

$v = 0.74 \cdot f_{ck} / 200 \leq 0.4$ effectiveness factor acc. to section 4.3.2.3 of EC 2 Part 1-3

$\psi = \frac{A_s}{A_j}$ shear reinforcement ratio

A_s cross-sectional area of steel

A_j area of joint

ζ angle of inclination of shear reinforcement , $45^\circ \leq \zeta \leq 90^\circ$

The shear stress in the joint is equal to (EC2, part 1-3, eq. 4.189):

$$v_{Sdj} = \eta \cdot V_{Sd} / (z \cdot b_j) \quad (2.15a)$$

2.7.6 Skew reinforcement

A reinforcement arrangement following the tensile forces T_2 and T_3 of the tripod model (Fig. 2.17) would require inclined reinforcement across the flange-web corners. However, usually a grid of horizontal reinforcement and reinforcement parallel to the web is preferred. Fig. 2.22 shows how a single tie can be replaced by a system of orthogonal struts and ties. The angle between struts and ties should not be less than 25 degree ($\tan \eta > 0.5$).

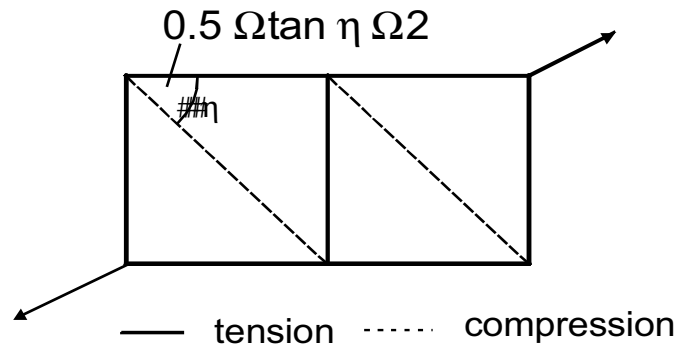


Figure 2.22 Skew reinforcement [4]

2.7.7 Strut-and-tie model of Neuser

Neuser [25] has investigated the load transfer in deviators and anchorage blocks of external prestressed bridges. His strut-and-tie model (Fig. 2.23) is similar to the tripod model (Fig. 2.17) except that no tensile forces T_3 and T_2 are required.

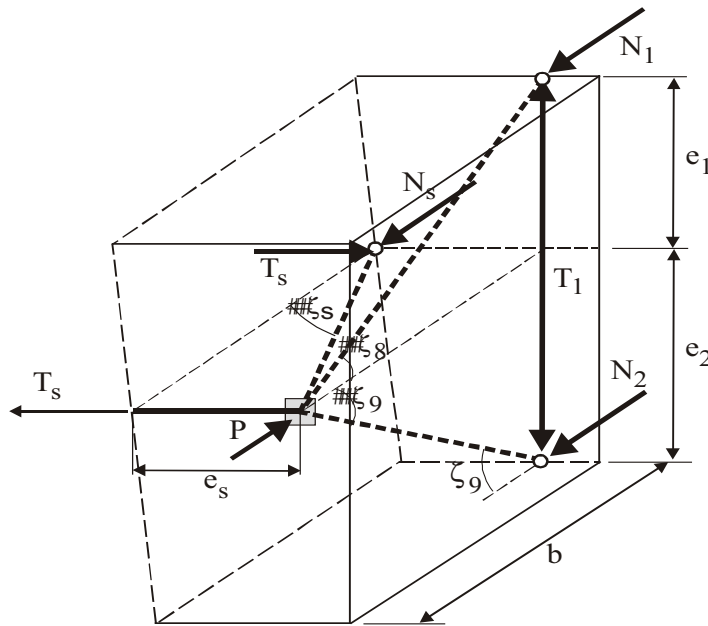


Figure 2.23 Strut-and-tie model of Neuser [25]

The forces can be calculated with the following equations.

$$N_s \mid P \left[\frac{\rho_1}{\rho_1 + 2\rho_2} \right] \dots \dots \dots (2.16)$$

$$T_s \mid N_s \tan \zeta_s \mid P \left[\frac{\rho_1}{\rho_1 + 2\rho_2} \right] \tan \zeta_s \dots \dots \dots (2.17)$$

$$N_1 | / P 4 N_s 0 \left(\frac{e_2}{e_1 2 e_2} \right) | P \left(\frac{\rho_1}{\rho_1 2 \rho_2} \right) \left(\frac{1}{12 \frac{e_1}{e_2}} \right) \dots \dots \dots (2.18)$$

$$N_2 | / P 4 N_s 0 \left(\frac{e_1}{e_1 2 e_2} \right) | P \left(\frac{\rho_1}{\rho_1 2 \rho_2} \right) \left(\frac{1}{12 \frac{e_2}{e_1}} \right) \dots \dots \dots (2.19)$$

$$T_1 | N_1 \tan \zeta_1 | P \left(\frac{\rho_1}{\rho_1 2 \rho_2} \right) \left(\frac{1}{12 \frac{e_1}{e_2}} \right) \tan \zeta_1 \dots \dots \dots (2.20)$$

$$\rho_1 | \frac{e_1}{e_s} \left(\frac{1}{\xi \tan^2 \zeta_s 2 \frac{1}{\cos^2 \zeta_s \sin \zeta_s}} \right) \dots \dots \dots (2.21)$$

$$\rho_2 | \frac{\left(\frac{\rho_1}{\rho_1 2 \rho_2} \right) \left(\frac{e_1}{e_2} \right)^2}{\frac{1}{\cos^2 \zeta_1 \sin \zeta_1} 2 \frac{e_1}{e_2} \left(\frac{1}{\cos^2 \zeta_2 \sin \zeta_2} \right)} \dots \dots \dots (2.22)$$

where:

P horizontal prestressing force

N_s normal force in the web due to P

N_1 normal force in the top slab due to P

N_2 normal force in the bottom slab due to P

T_s tensile force due to corbel action

T_1 tensile force due to splitting forces

e_s distance between load and web

e_1, e_2 distance between load and slabs, where $e_1 \Omega e_2$

$\zeta_s, \zeta_1, \zeta_2$ angle with: $\tan \zeta_1 | e_1 / b$; $\tan \zeta_2 | e_2 / b$; $\tan \zeta_s | e_s / b$ where $e_1 \Omega e_2$

$\xi | \frac{E_c A_c}{E_s A_s}$ stiffness ratio between struts and ties

The stiffness ratio ξ may be taken as 1.0. The value does not have a significant influence on the results.

Further information about strut-and-tie models can be read in references [32-40, 42-43, 45]

2.8 Design of anchorage zone

2.8.1 General

Anchorage zones for post-tensioning tendons are regions of complex stresses. The post tensioned anchorage zone may be considered as being composed of two zones (Fig. 2.24).

The *local* zone is the region immediately surrounding each anchorage device. It can be cylindrical or prismatic with transverse dimensions approximately equal to the sum of the width of the anchorage plate plus the manufacture's specified minimum side or edge cover. The length of the local zone is defined as the length of the anchorage device plus an additional distance in front of the anchor equal to at least the lateral dimension of the anchor.

The *general* zone is the region in front of the anchor, which extends along the tendon axis for a distance equal to the overall depth of the member. The height of the general zone is taken as the overall depth of the member.

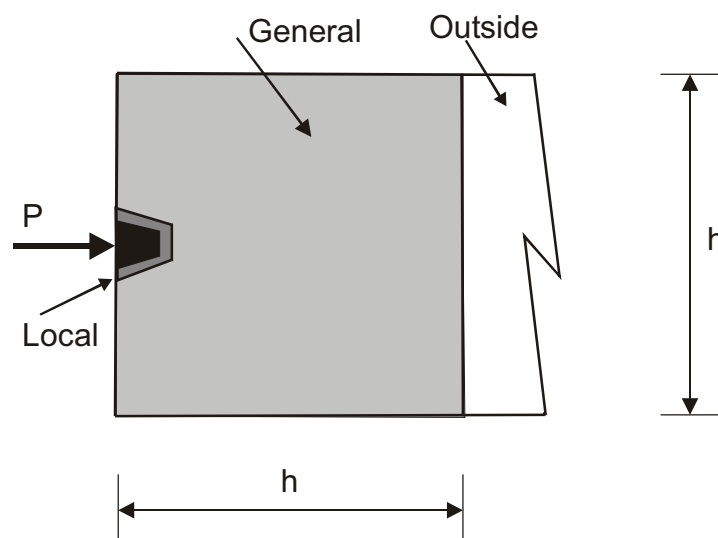


Figure 2.24 Subdivision of anchorage zone [5]

Design and specification of required reinforcements in the general zones are the responsibility of the design engineer. Proper installation of reinforcements is the responsibility of the constructor.

The reinforcements of the local zone, which is under the tendon anchors, must be adequate to transfer the tendon force into the mass of concrete structure. The load can successfully be transferred by either bearing plate type anchors or by special anchorage devices, which in combination with special anchor reinforcement (such as spirals, stirrups or other reinforcement) transfer the local zone loads from the anchors into the general anchorage zone of the structure.

2.8.2 Verification of anchorage design

Anchorage devices and the transfer of forces from the bearing plate to the concrete have to be verified by experiments. It is difficult to model the accurate stress flow in the end zone by numerical analysis due to complex material behaviour and the interaction between anchor plate, the concrete and the reinforcement [23]. Nevertheless empirical formulae are useful for verification of load bearing capacity of the anchorage device before testing and to understand the load transfer mechanisms.

The experimental results on small concrete columns loaded by concentrated forces due to vertical prestressing [20] show that cracks were developed at the centre (Fig. 2.25). Further increase of load creates a wedge under the loading plate that ultimately results in failure of the specimen. The use of spiral reinforcement or stirrups can prevent this failure. This leads to a triaxial state of concrete stresses, and as a result, the bearing capacity of the concrete increases. The verification of resistance force on loaded area can be done approximately by the formulae given in DIN 1045, 10.7 and EC2, 5.4.8.1 whereas the influence of spiral and stirrups steel is approximated by the model given in CEB Model Code 90.

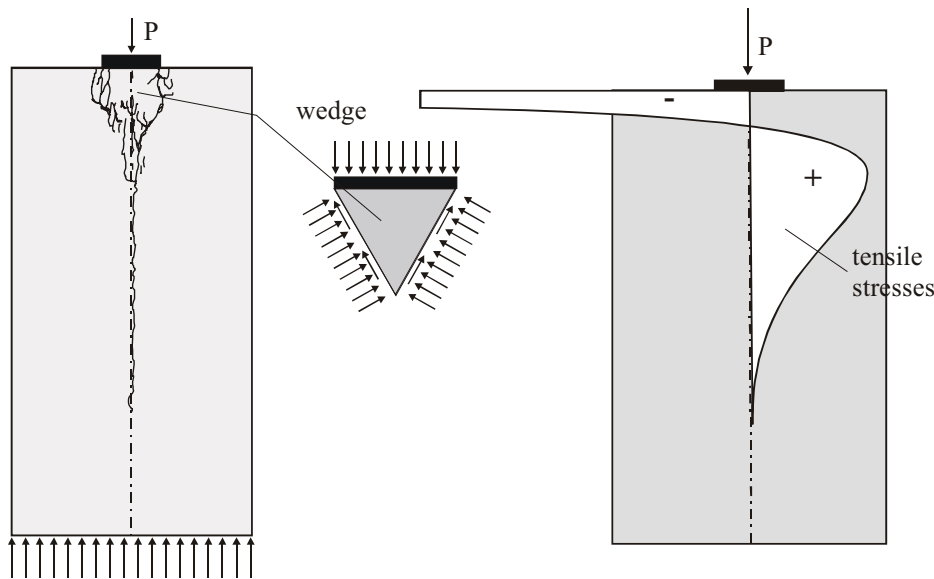


Figure 2.25 Crack and tensile splitting stress on deep beam [20]

The following explanations are given to study the principle structural load behaviour of the concrete in an anchorage region. In Europe only these equations are not enough for design of the anchorage zones, but test must be done to check the bearing capacity.

2.8.3 Concentrated forces

For uniform distribution of loaded area A_{c0} (Fig. 2.26) on unreinforced normal concrete the concentrated resistance force can be determined as follows (DIN 1045-1, 10.7 and EC2 part 1):

$$F_{Rdu} | A_{c0} (f_{cd} \sqrt[3]{A_{c1} / A_{c0}} \Omega 3.0 (f_{cd} \sqrt[3]{A_{c0}} \text{ (DIN 1045-1, Eq. 116) (2.23)$$

or

$$F_{Rdu} | A_{c0} (f_{cd} \sqrt[3]{A_{c1} / A_{c0}} \Omega 3.3 (f_{cd} \sqrt[3]{A_{c0}} \text{ (EC 2, Eq. 5.22)$$

Where:

$A_{c0} | b_1 \hat{a}_1$ loaded area

$A_{c1} | b_2 \hat{a}_2$ maximum area corresponding geometrically to A_{c0} , having the same centre of gravity, which it is possible to inscribe in the total area A_c , situated on the same plane as the loaded area.

$f_{cd} | f_{ck} / \nu_c$ (EC) resp. $f_{cd} | \zeta (f_{ck} / \nu_c$ (DIN 1045-1)

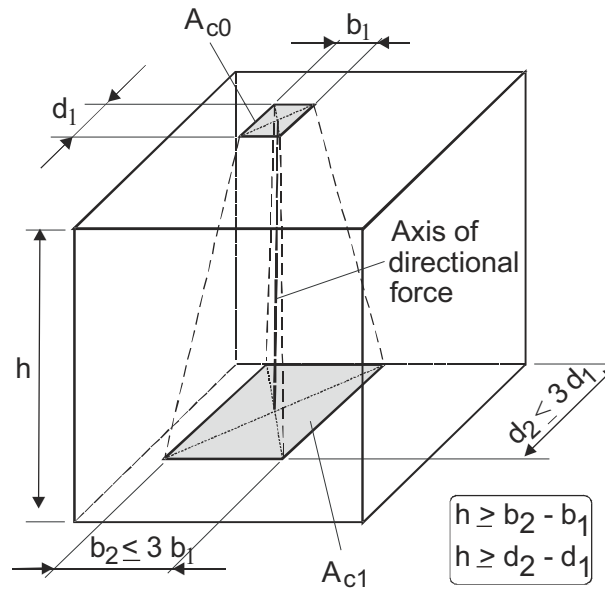


Figure 2.26 Area A_{c1} by concentrated force [19]

2.8.4 Practical modeling

Equation 2.23 has to be modified to consider the influence of the spiral or stirrups reinforcement in the local zone behind the anchorage plate [16, 22]. Due to confined reinforcement the lateral strain under the loaded area is hindered. This results in a triaxial state of concrete stresses which in turn increases the compressive strength of concrete from f_{cd} to f_{cd}^* . Furthermore, it is assumed in the following that the spiral or stirrup reinforcement in ultimate limit state achieves the design yield strength f_{yd} .

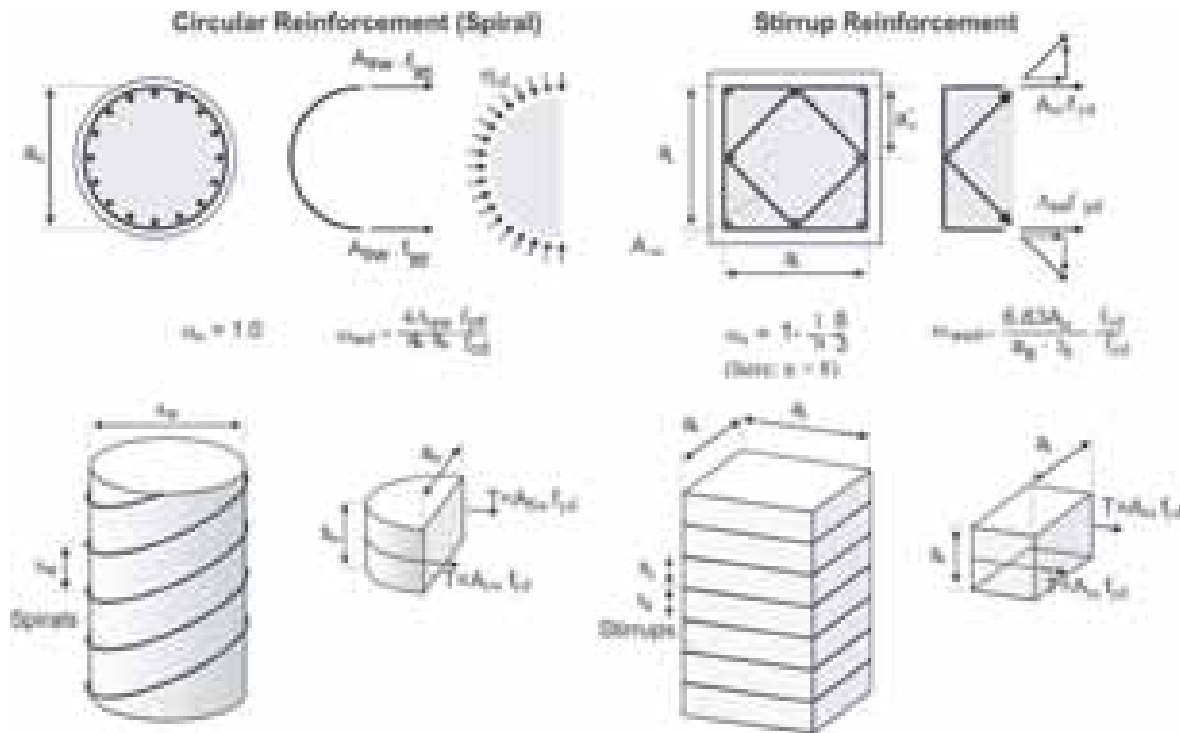


Figure 2.27 Forces in spiral and rectangular stirrup reinforcement

Force in the reinforcement: $F_{sd} = \omega_{sd} A_s = f_{yd} A_{sw}$ (2.24)

- with: A_{ss}, A_{sw} area of spiral or stirrup steel
- s_s, s_w spacing of stirrup or height of spiral steel
- a_w diameter of spiral steel

In the following only circular reinforcement is considered:

The corresponding concrete compressive force: $F_{cd} = 0.5 \omega_{cd} A_w$ (2.25)

By considering the spacing of spiral steel the equations in (2.24) and (2.25) are converted to:

$$f_{yd} A_{sw} = 0.5 \omega_{cd} A_w / s_w \quad \text{and} \quad \omega_{cd} = \frac{2 f_{yd} A_{sw}}{a_w s_w} \dots\dots\dots (2.26)$$

Volumetric mechanical ratio of confining steel ω_{wd} is defined as follows:

$$\omega_{wd} = \frac{W_{s,trans}}{W_{c,cf}} = \frac{f_{yd}}{f_{cd}} = \frac{4 A_{sw} f_{yd}}{a_w s_w f_{cd}} \dots\dots\dots (2.27)$$

Then equation 2.26 becomes:

$$\omega_{cd} | 0.5 \bar{\omega}_{wd} f_{cd} \dots\dots\dots (2.28)$$

Taking into account the non-uniformity of distribution of these confining stresses, the effective lateral stress may be approximated by the expression:

$$\frac{\omega_{cd,2}}{f_{cd}} - \frac{\omega_{cd,3}}{f_{cd}} | 0.5 \zeta_n \zeta_s \bar{\omega}_{wd} \dots\dots\dots (2.29)$$

Where:

$W_{s,trans}$ Volume of transverse reinforcement

$W_{c,cf}$ Volume of confined concrete

ζ_s Reduction factor expressing the effective concrete area in elevation for spiral steel s_w and vertical spacing s_s

$$\zeta_s = \left(\frac{s_w}{a_w} \right)^2 \text{ where } s_w \leq 0.5 a_w \dots\dots\dots (2.30)$$

ζ_n Reduction factor expressing the effective concrete area in plan for reinforcement in shear

For circular stirrup and spiral steel: $\zeta_n = 1$

For rectangular stirrup in two layers as seen in Fig. 2.27

$$\zeta_n = 1 - 4 \frac{n (a'_s)^2 / 6}{a_s^2} | 1 - 4 \frac{1}{n} \frac{8}{3} \dots\dots\dots (2.31)$$

$$\bar{\omega}_{w,s} | \frac{6.83 A_{ss}}{a_s s_s} \frac{f_{yd}}{f_{cd}} \dots\dots\dots (2.32)$$

n = number of longitudinal steel

The above equations show clearly that a circular or spiral reinforcements are considerably more favorable than stirrup reinforcements. There is a relation between load distribution and distribution of longitudinal reinforcements in the end zone. The provided longitudinal reinforcement in an anchorage zone however, is not sufficient enough to distribute the transverse force. So, spiral reinforcements with their limited spacing are important to achieve uniform stress distribution.

The following linearized approximation can be used to determine the triaxial concrete compressive stress f_{cd}^* [16]:

$$f_{cd}^* | f_{cd} \left(12.5 \cdot \left(\frac{\omega_{cd,2}}{f_{cd}} \right)^0 \right) \quad \text{for } \frac{\omega_2}{f_{cd}} \leq 0.05 \dots\dots\dots (2.33)$$

$$f_{cd}^* | f_{cd} \left(1.125 \cdot 2.25 \cdot \left(\frac{\omega_{cd,2}}{f_{cd}} \right)^0 \right) \quad \text{for } \frac{\omega_2}{f_{cd}} > 0.05 \dots\dots\dots (2.34)$$

Substituting equation 2.29 into 2.33 and 2.34

$$f_{cd}^* | f_{cd} \left(12.25 \cdot \zeta_n \cdot \zeta_s \cdot \left(\frac{\omega_{wd}}{f_{cd}} \right) \right) \quad \text{for } \frac{\omega_{cd,2}}{f_{cd}} \leq 0.05 \dots\dots\dots (2.35)$$

$$f_{cd}^* | f_{cd} \left(1.125 \cdot 2.125 \cdot \zeta_n \cdot \zeta_s \cdot \left(\frac{\omega_{wd}}{f_{cd}} \right) \right) \quad \text{for } \frac{\omega_{cd,2}}{f_{cd}} > 0.05 \dots\dots\dots (2.36)$$

There is high stress under the anchor plate. Therefore only equation 2.36 is relevant for design of anchorage regions. Accordingly the maximum concentrated resistance force F_{Rdu} is:

$$F_{Rdu} | A_{c0} \left(f_{cd}^* \cdot \sqrt{A_{c1} / A_{c0}} \right) | A_{c0} \left(f_{cd} \cdot \left(1.125 \cdot 2.125 \cdot \zeta_n \cdot \zeta_s \cdot \left(\frac{\omega_{wd}}{f_{cd}} \right) \right) \cdot \sqrt{A_{c1} / A_{c0}} \right) \dots\dots\dots (2.37)$$

Hereby area A_{c1} should be enclosed by transverse reinforcement. A_{c0} is the loaded area. Equation 2.37 and the experimental results of Rostasy et. al. [22] are in good agreement.

The load bearing capacity of the anchorage device according to equation 2.37 is about 50% higher than the usual failure load of the tendons which are anchored. Hence, a failure of the anchorage area is excluded.

The experimental results by Wurm and Daschner [21] show that the tensile force in the spirals is near the ultimate state by a far greater amount than the sum of transverse stresses calculated e.g. by strut-and-tie models. The above-mentioned equations only consider the stresses and not the cracking in concrete. A numerical determination of the cracks resulting from a prestressing force is still not possible. So, it is important to verify anchorage devices by experiment.

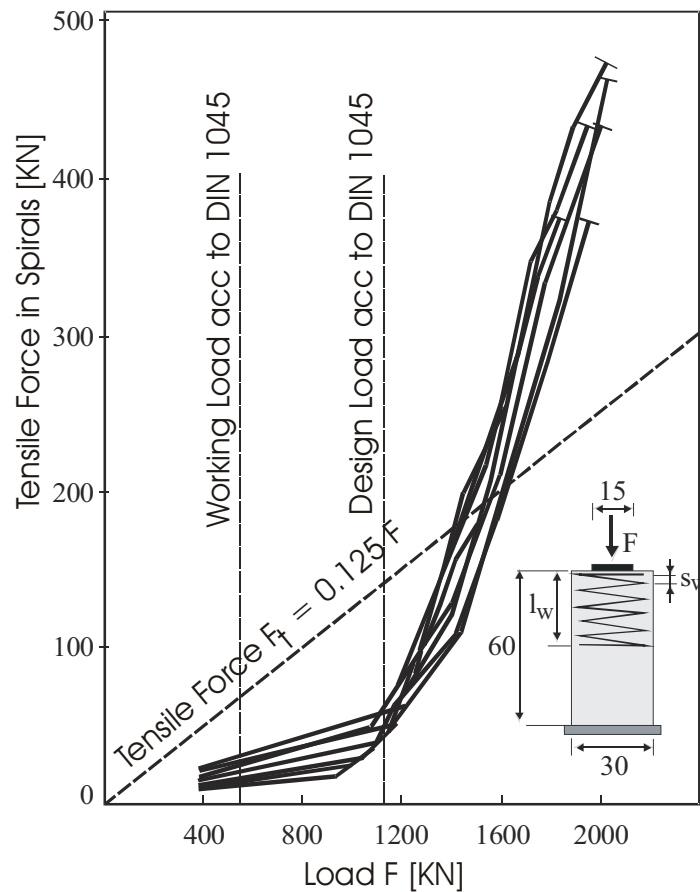


Figure 2.28 Tensile force in spiral reinforcement according to Daschner [21]

Nevertheless, equations mentioned above are helpful to estimate the required modifications of an anchorage device (e.g. size of the anchorage plate) and the spiral reinforcement, if the values of prestressing force are increased slightly over the approved value. The relevant equations have been published by the German ‘Institut für Bautechnik’ [28].

2.8.5 Design of anchorage zone according to CEB-FIP

Current design codes in some countries, while specifying the anchorage zone stresses, usually make recommendations in terms of allowable bearing stresses. In other specifications emphasis is placed on the bursting stress distribution.

Mörsch was the first [102] to publish a model to estimate the distribution of forces in a plane specimen loaded by a single load (Fig. 2.29). The local bursting force is assumed to be equal to:

$$F_{bs} = 0.25 \hat{P} \left(14 \frac{a_0}{h} \right) \dots\dots\dots (2.38)$$

Leonhardt [15] suggested the same factor of 0.25 but the recommendation of CEB-FIP Model Code 78 gives a value of 0.3. Furthermore the bursting force F_{bs} is dependant on the geometric enlargement side (Fig. 2.26) or diameter of loaded area a_1 and not on the depth of the section h . This results in

$$F_{bs} = 0.3 \left(P \left(1 + 4 \frac{a_0}{a_1} \right) \right) \dots \dots \dots (2.39)$$

Where:

- F_{bs} total bursting (tensile) force
- P the applied normal force, e.g. prestressing force
- a_0 diameter or length of side of loaded area
- a_1 diameter or length of side of geometric enlargement of loaded area (symmetric prism theorem) (Fig. 2.30)
- h overall depth of section

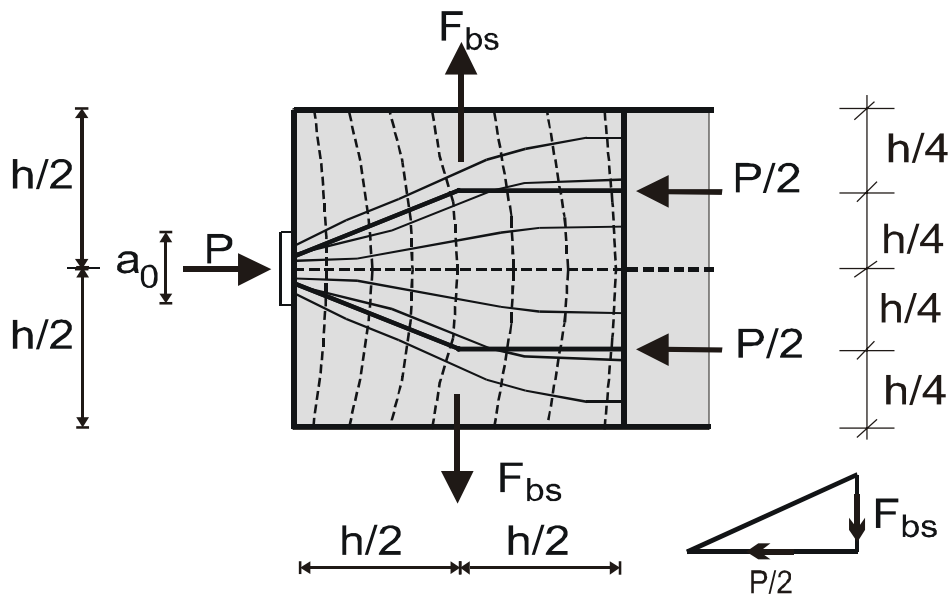


Figure 2.29 Simplified equilibrium of force according to Mörsch [102]

The differences between the various models demonstrate the great uncertainty of these approaches.

CEB-FIP Model Code 87 [16a] contains the same formula as suggested by Leonhardt.

$$F_{std} = 0.3 \left(F_{sdu} \left(1 + 4 \frac{a_0}{a_1} \right) \right) \dots \dots \dots (2.40)$$

F_{sdu} is the ultimate prestressing force and not the design value. A safety factor of 1.35 has to be used.

$$F_{sdu} | 1.35 \omega_{po} A_p \Omega f_{pk} A_p \dots\dots\dots (2.41)$$

According to the CEB-FIP Model Code 87, the corresponding transverse tensile forces may be assumed to be constant over the distance between $0.1a_1$ and a_1 (Fig. 2.30) and may be calculated in each direction.

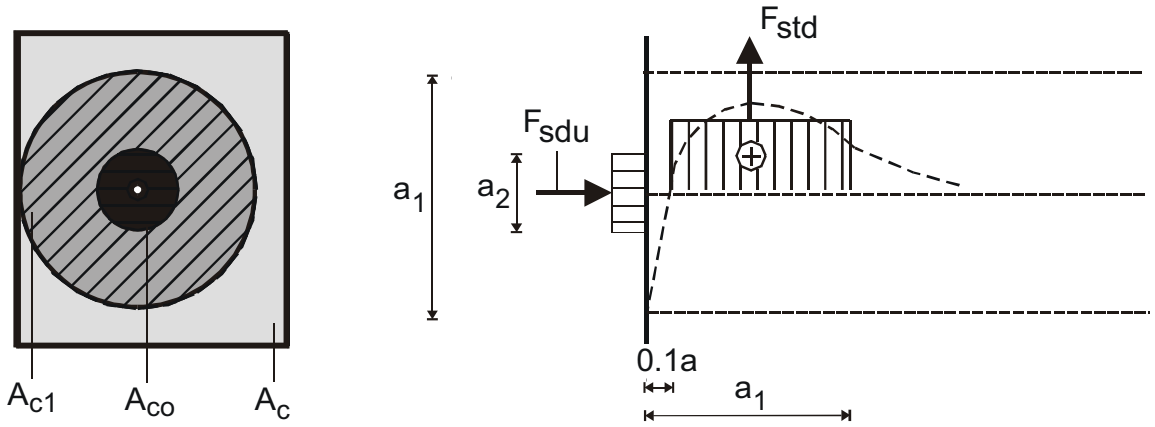


Figure 2.30 Definitions for the CEB-FIP regulations [15]

Furthermore the CEB-FIP model code 87 prescribes that for the case of a reasonably uniform distribution of the applied pressure, i.e. uniform stress under the anchorage device, the local resisting force shall be determined as follows (detailed explanation see section 2.8.4):

$$F_{Rdu} | f_{cd} A_{co} \sqrt{A_{cl} / A_{co}} \Omega 3.3 f_{cd} A_{co} \dots\dots\dots (2.42)$$

where:

- f_{cd} design strength of concrete
- A_{co} loaded area
- A_{cl} maximum area corresponding geometrical to A_{co} , having the same centre of gravity, which it is possible to inscribe in the total area A_c , situated in the same plane as the loaded area
- F_{Rdu} concentrated resistance force on area A_{co}

Since the coefficient of safety applicable to concrete v_c is usually equal to 1.5, i.e.

$f_{cd} = f_{ck}/1.5$ the CEB-FIP model code 87 formula can be transcribed to:

$$\omega_c \Omega \frac{F_{Rdu}}{A_{co}} \leq 0.67 f_{ck} \sqrt{A_{cl} / A_{co}} \Omega 2.2 f_{ck} \dots \dots \dots (2.43)$$

2.8.6 Design of anchorage zones according to AASHTO guide specification

2.8.6.1 Permissible anchorage stresses

The permissible bearing stress under the anchorage plate and at any section within the anchorage zone behind the plate in accordance with AASHTO [5] guide specification section 9.2.3 are as follows:

(a) At application of post-tensioning force

$$f_{cp} \leq 0.8 f_{ci} \sqrt{A'_c / A_c} \Omega 1.25 f_{ci} \quad (\text{AASHTO}) \dots \dots \dots (2.44)$$

(b) At service load

$$f_{cp} \leq 0.6 f'_c \sqrt{A'_c / A_c} \Omega 1.25 f'_c \quad (\text{AASHTO}) \dots \dots \dots (2.45)$$

Where:

f_{ci} compressive stress of concrete at time of initial prestress

f'_c specified compressive strength of concrete

f_{cp} permissible concrete compressive stress under anchorage

A'_c maximum area of the portion of the concrete anchorage surface that is geometrically similar to and concentric with the bearing area of the tendon anchorage

A_c bearing area of tendon anchorage

The stresses calculated at application of the post-tensioning force and at service load shall be limited to 5000 psi (34.5 MPa) and 6250 psi (43.1 MPa) respectively, as absolute maximum values even if the concrete strength is in excess of 4000 psi (27.6 MPa) at transfer (load application) and 5000 psi (34.5 MPa) at 28 days.

Significant differences in the permissible bearing stress between AASHTO and CEB-FIP can be observed (eq. 2.43 – 2.45)

2.8.6.2 Forces and reinforcement

The distribution of forces and the reinforcement required to provide the necessary general zone tensile capacity to resist the bursting forces of the anchorage may be determined by using strut-and-tie models. The total bursting force F_{bst} for an individual anchorage should be taken in accordance with AASHTO guide specification section 14.2 as:

$$F_{bst} = 0.30 \left(1.4 \frac{d_a}{d_{sp}} \right) P_j \quad \dots\dots\dots (2.46)$$

Where:

F_{bst} total bursting force (tensile) due to tendon anchorage

d_a depth of anchor plate

d_{sp} total depth of symmetric concrete prism above and below the anchor plate
(also assumed to be the length of the anchorage zone)

P_j tendon jacking force

The above equation is similar to that of the CEB-FIP Model Code (see eq. 2.39)

The local zone shall be reinforced for the bursting and post-tensioning forces. The reinforcement may consist of stirrups, ties, spirals, or combination of these. The general zone shall be reinforced with stirrups or ties to resist bursting forces and the total post-tensioning forces anchored at a section. Reinforcement for bursting forces shall be designed for maximum jacking forces at time of stressing with $f_{s,max} = 0.6f_{sy}$. The steel stress ω_s shall not exceed 60 kips (414 MPa). Post-tensioning may be provided to supplement reinforcement restraint against anchorage bursting or directional forces.

Further information about anchorage zones can be read in references [44, 47, 48, 50, 54, 59]

3. Stresses in shear wall analysed by finite element method

The main purpose of the following investigations is to find out the load paths in a shear wall and diaphragm. Previously Schlaich et. al. [3 ,7] conducted such a type of research, but the analytic tool that was used by him was not as sophisticated as the ones available today. So, it is imperative to utilize modern technology to verify previously developed models. In this regard the powerful, general purpose finite element software called “Ansys” will be used to analyse various models of shear walls and diaphragms with different boundary conditions and loadings. The numerical results will be compared with the models developed by Schlaich.

First 2-D finite element analysis of diaphragms will be presented. Plane shear wall models are used for practical design. Then the results of a complex 3-D model will be shown.

3.1 Modeling

For the following elastic and material non-linear analysis of 2-dimensional shear walls, the volume element called “solid65” was selected. A volume element was used for the investigations instead of a plane shell element, as material non-linear analysis will be conducted. The shear walls or diaphragms are calculated in practice mostly by 2-dimensional models. For the elastic analysis the following material parameters were used:

$$\begin{aligned} \text{concrete: } & f_{ck} = 58.5 \text{ N/mm}^2, f_{ctm} = 4.4 \text{ N/mm}^2 \\ & E_c = 43000 \text{ N/mm}^2, \nu = 0.2 \text{ (poisson ratio)}, \\ \text{steel: } & E_s = 200,000 \text{ N/mm}^2, f_{yk} = 550 \text{ N/mm}^2 \end{aligned}$$

These above listed material parameters were taken from the full-scale test of a segmental bridge conducted by Takebayashi et. al. in Bangkok [6]. Further the non-linear stress-strain diagram of concrete in accordance with EC2 part 1, 4.2.1.3.3(5) and for steel EC2, 4.2.2.3.2(5) were used (Fig. 3.1).

In compression zone the failure criterion of William and Warnke (Fig. 3.2) is implemented. They have developed triaxial model for failure surface and material

property of concrete. Fig. 3.3 depicts the 3-D failure surface for states of stresses that are biaxial.

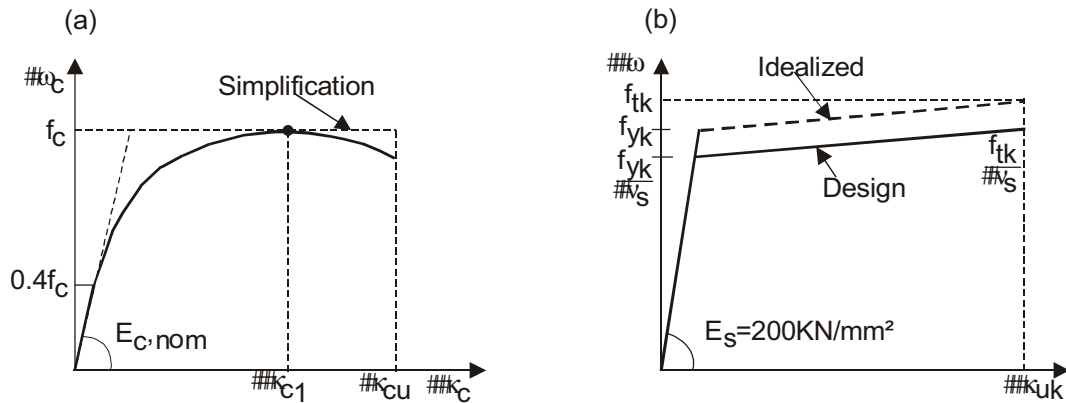


Figure 3.1 Stress-strain diagram (a) concrete according to EC2 Fig. 4.1 and (b) steel according to EC2 Fig. 4.5 [18]

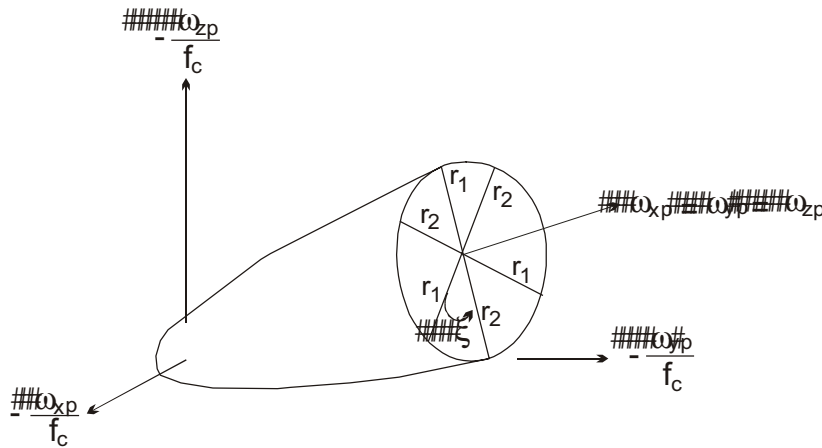


Figure 3.2 3-D failure surface in principal stress space-triaxial state [17]

The criterion for failure of concrete due to a multiaxial stress state can be expressed in the form

$$\frac{F}{f_c} 4 S \geq 0 \dots\dots\dots (3.1)$$

Where: F = a function of principal stress state ($\omega_{xp}, \omega_{yp}, \omega_{zp}$)

S = failure surface expressed in terms of principal stresses and five input

Parameters $f_t, f_c, f_{cb}, f_1, f_2$ in table 4.7.1 reference [17]

f_c = uniaxial crushing strength

$\omega_{xp}, \omega_{yp}, \omega_{zp}$ = stresses in principal directions

If equation (3.1) is not satisfied, there will be no cracking or crushing. Otherwise, the material will crack if any principal stress is tensile and crushing will happen if all principal stresses are compressive. Detail explanations are given in reference [17].

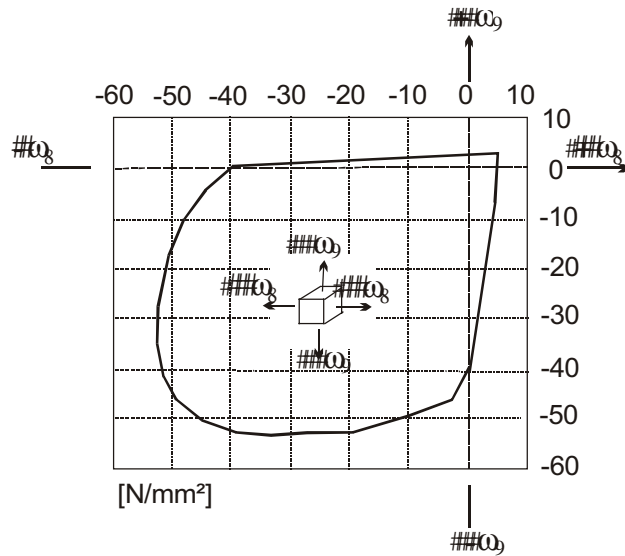


Figure 3.3 Failure surface for biaxial state of stress for concrete

$$f_{ck} = 40 \text{ N/mm}^2 \quad [17]$$

Various types of shear walls were selected (Fig. 3.4):

- # shear wall with two supports and closed diaphragm
- # shear wall with central support and closed diaphragm
- # shear wall with two supports and open diaphragm

The width of each bearing is 50 cm for the shear wall with two supports and 70 cm in case of central support like in the real segmental bridge (Fig. 3.4).

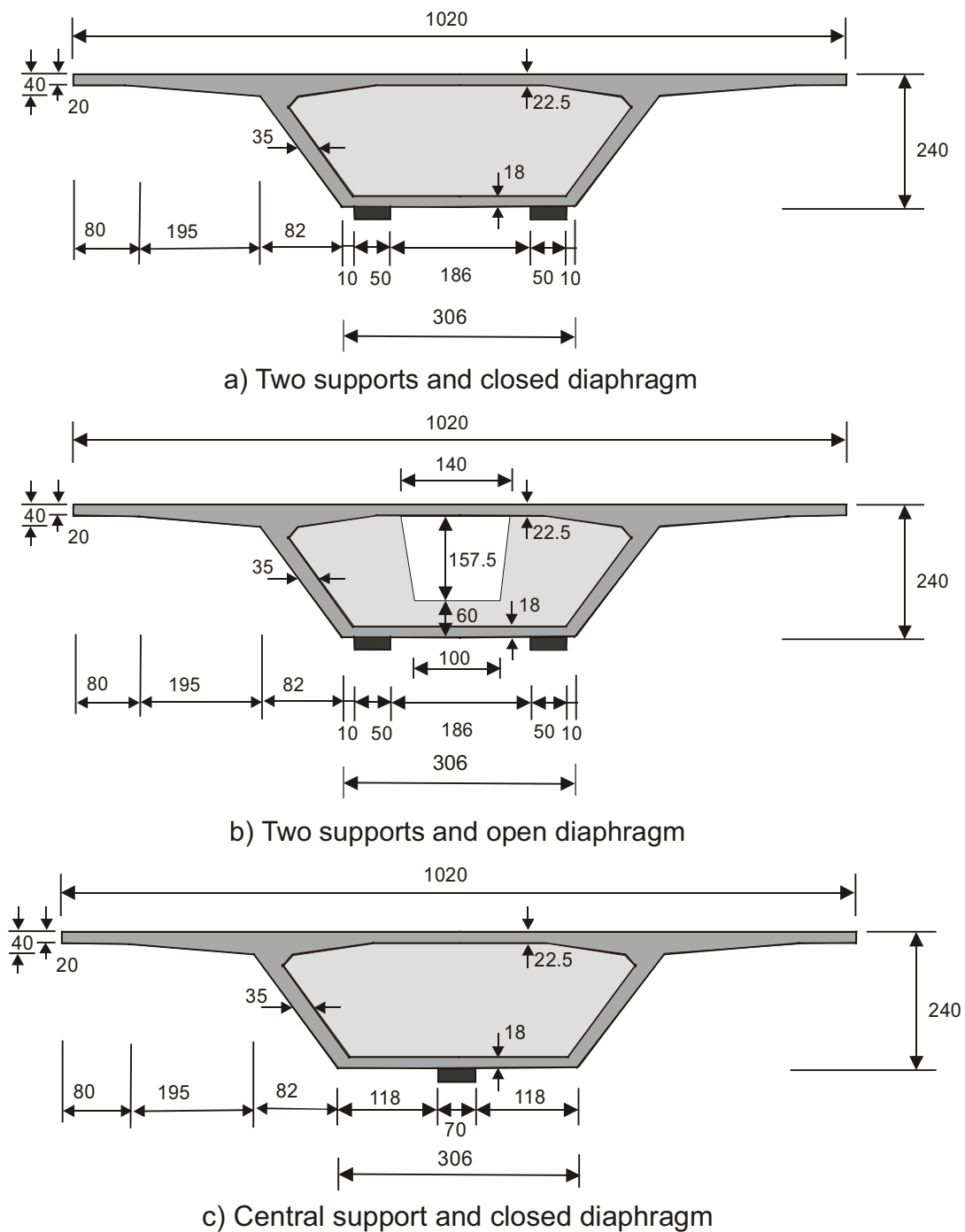


Figure 3.4 Shear wall models for analysis

In accordance with the segmental bridge built in Bangkok the shear wall has a width of 10.2 m, 2.4 m depth and 0.75 m thickness. The finite element meshes of a shear wall without opening and with opening are shown in Figs. 3.5 and 3.6 respectively.

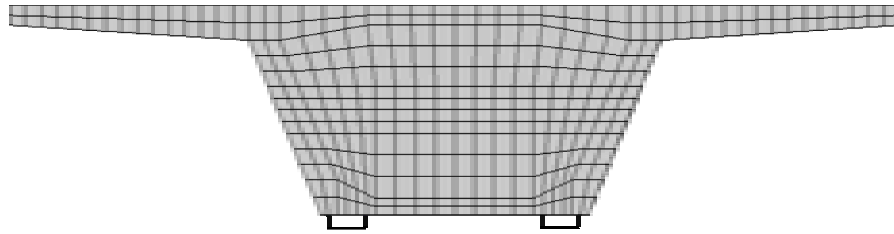


Figure 3.5 Shear wall without opening – Finite element mesh

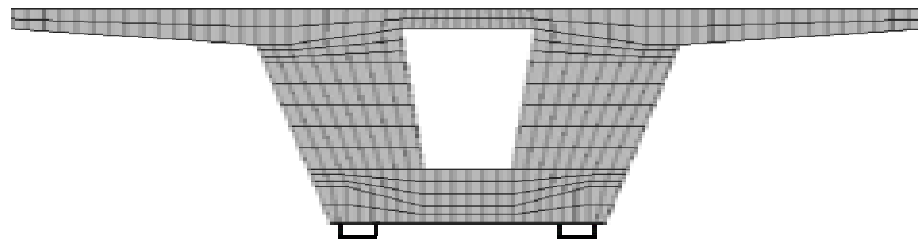


Figure 3.6 Shear wall with opening – Finite element mesh

For both elastic and material non-linear analysis, three different loading conditions were considered namely “bending”, “shear” and “torsion”. The loads were applied directly on top of the web. The 3D-analysis of a whole span of a segmental bridge for permanent loads was conducted to verify this simplification (for details see chapter 4). One result of this analysis is presented here. Fig. 3.7 shows the principal stress distribution. The inner part of the diaphragm has minor compressive stress. From this it is possible to conclude that the major portion of the load of the bridge pass through the webs to the supports. Next the 3D analysis showed (see also Fig. 4.15) that the major vertical load form the superstructure acts at top of the diaphragm. So, the simplification of load arrangement on top of the webs (Figs, 3.10 to 3.12) is acceptable. Based on this result, representative load models were developed for a shear wall with open and closed diaphragm in the following chapter.

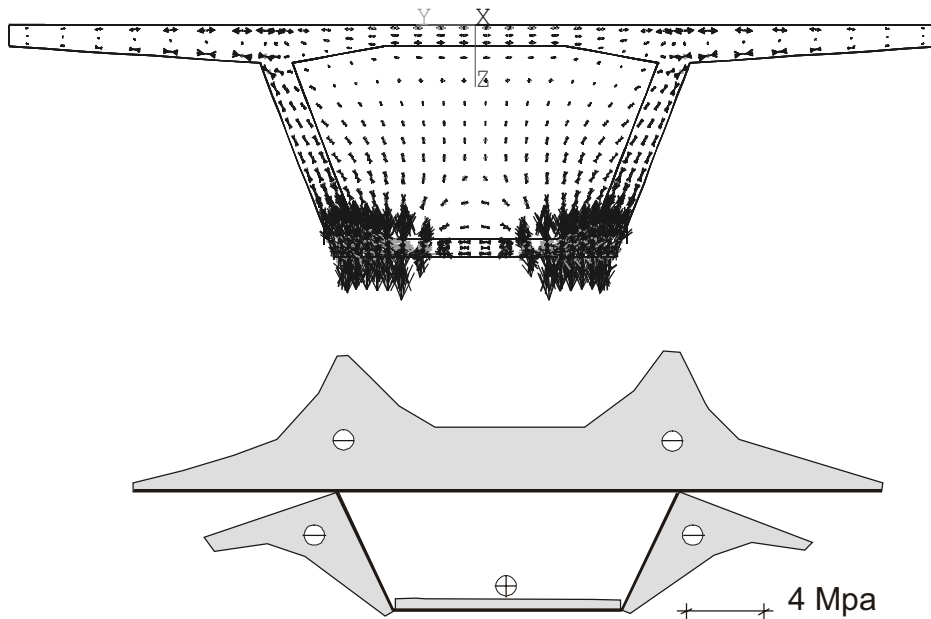


Figure 3.7 Side view of principal stress diagram (top) and vertical stress distribution in the first joint for permanent loading (3D analysis)

3.2 Evaluation of load arrangement

First the support forces resulting from the dead load (self weight and imposed loads) are calculated from the real segmental bridge shown in (Figs. 1.7 and 1.9) that has a span length of $l = 43.25$ m, depth of $h = 2.4$ m and a carriageway width of $w = 10.2$ m. The width w of notional lanes on that carriageway (in general 3.0 m) and the greatest possible whole (integer) number n_1 of such lanes are given in Tab. 3.1. This table determines the width and number of notional lanes for vertical live load models shown in Figs. 3.8 and 3.9.

Only load model 1 is used in the following in accordance with the German Regulations. The other load models of EC 1-3 are not applied in Germany. Load model 1 comprised of concentrated and uniformly distributed loads that includes the effect from traffic of trucks and cars (Fig. 3.8). The basic values of this load model are given in Tab. 3.2.

Table 3.1 Number n_1 and width of lanes w (EC 1-3 Tab. 4.1)

Carriageway Width w	Number of notional lanes	Width of a notional lane	Width of remaining area
$w \{ 5.4m$	$n_1 \mid 1$	$3 m$	$w - 3 m$
$5.4m \leq w \{ 6m$	$n_1 \mid 2$	$w/2$	0
$6m \leq w$	$n_1 \mid \text{Int}(w/3)$	$3 m$	$w - 3 n_1$

Table 3.2 Basic values of Q_{ik} and q_{ik} for load model 1 (EC1-3 Tab. 4.2)

Position	Double axle Q_{ik} (KN)	Uniformly distributed load q_{ik} (KN/m ²)
Lane 1	300	9.0
Lane 2	200	2.5
Lane 3	100	2.5
Other lane	0	2.5
Remaining area	0	2.5

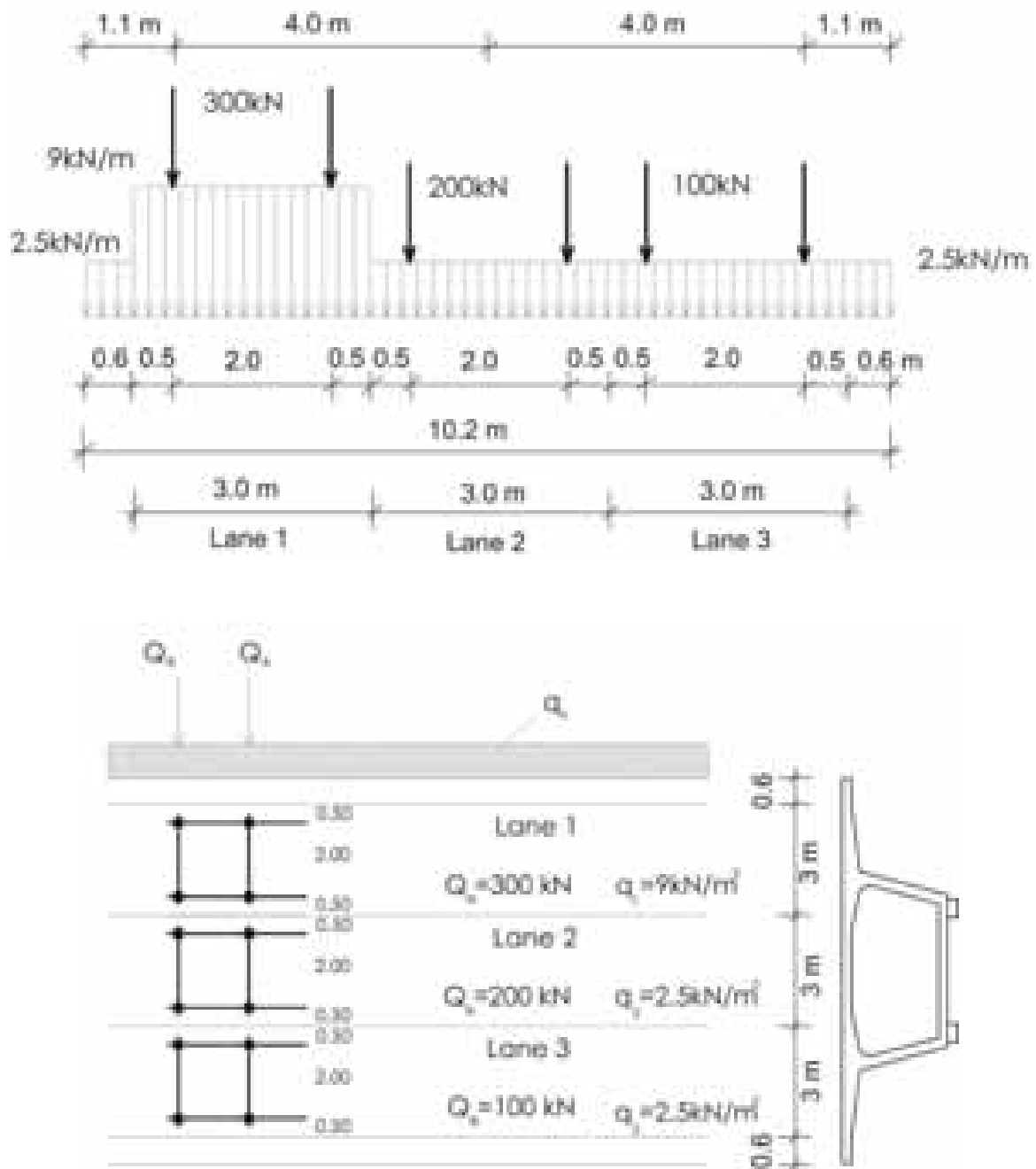


Figure 3.8 Traffic live load arrangement acc. EC1-3 Fig. 4.2 – max shear

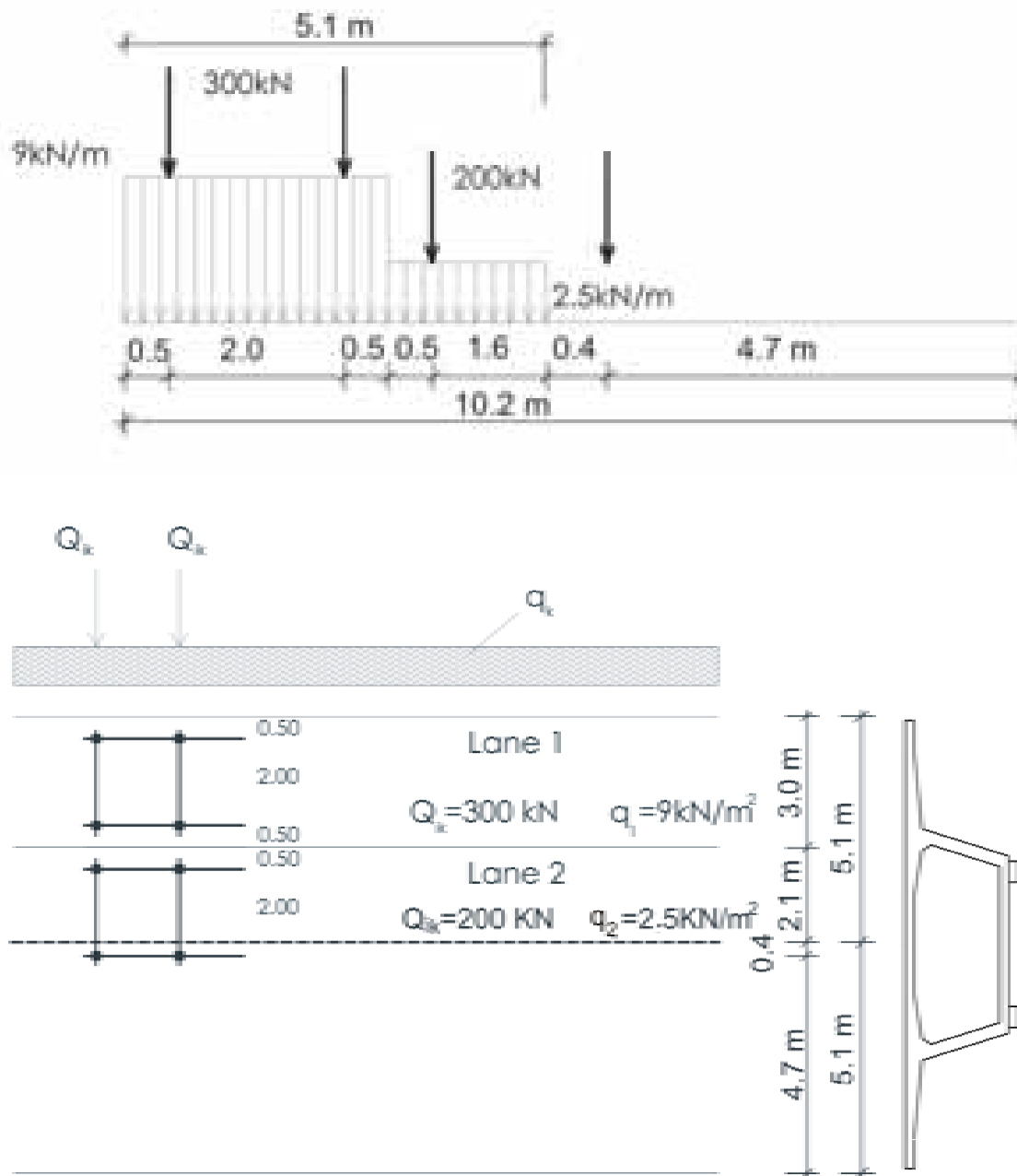


Figure 3.9 Traffic live load arrangement acc. EC1-3, Fig. 4.5 – max torsion

Four different load cases are considered:

- LC1 dead load ($g = 158.23 \text{ kN/m}$)
- LC2 traffic live load model 1 for max shear (Fig. 3.8)
- LC3 traffic live load model 1 for max torsion (Fig. 3.9)
- LC4 vertical prestressing load

The vertical component (V_p) from prestressing force after stressing P_{m0} , which acts at the deviators, was calculated according to the following equation ($\omega_{pm0} | 1275 MN/m^2, A_p | 0.0266m^2, 4P_{m0} | \omega_{pm0} (A_p | 33.915MN)$):

$$V_p | 4P_{m0} \tan \zeta \dots\dots\dots (3.2)$$

These load cases are combined in most unfavourable manner.

The whole bridge has to be analysed to determine the relevant loads for the diaphragm. Structural analysis of a bridge has to be conducted in transverse and longitudinal directions to determine the internal forces and moments for the superstructure of a hollow box girder segmental bridge. Statically the transverse direction may be considered as a frame system and a beam represents longitudinal direction. The calculated values of the vertical forces and torsion moments that should be carried by one shear wall are given in table 3.3.

Table 3.3 Support reactions and torsional moment per pier (characteristic values)

Load combinations	Vertical force (MN)	Torsional moment (MNm)
LC1 + LC4 (Permanent loads)	$V_b = 2.23$	0.00
LC1 + LC2 + LC4 (Maximum shear)	$V_s = 5.14$	4.61
LC1 + LC3 + LC4 (Maximum torsion)	$V_t = 4.47$	6.11

Table 3.3 shows that load combination LC1 + LC2 + LC4 gives maximum vertical force and LC1 + LC3 + LC4 gives maximum torsional moment. As it has been mentioned before the shear wall is loaded directly on top of the diagonal sides, but the challenge is how to apply the loads for max shear and max torsion in order to give the magnitude of vertical force and torsion. A reasonable approximation is used. The following load combination should be considered in ultimate limit state:

$$1.35(G_k + \div G_k + Q_k) + 1.0P \dots\dots\dots (3.3)$$

Where:

- G_k self weight
- $\div G_k$ imposed load
- Q_k variable live load
- P prestressing loads

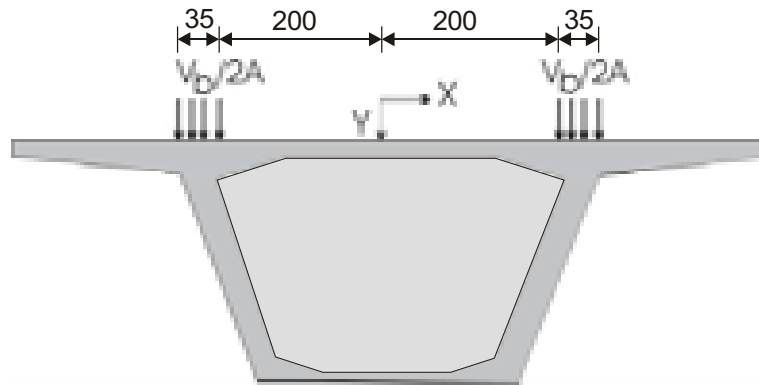


Figure 3.10 Load arrangement for permanent loads

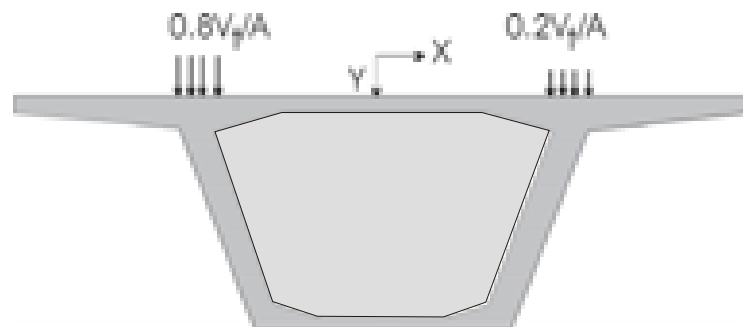


Figure 3.11 Load arrangement for max. torsion

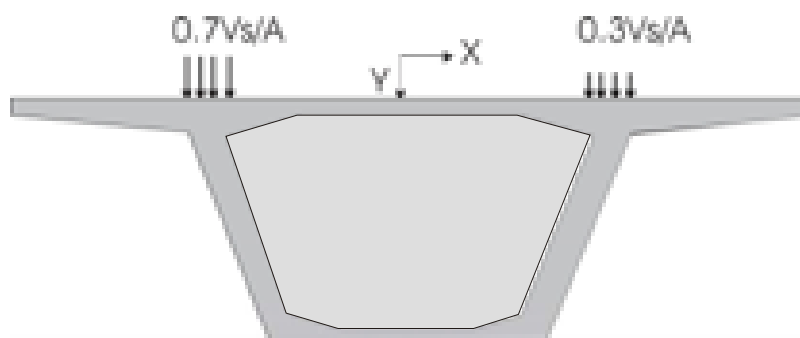


Figure 3.12 Load arrangement for max. shear

Where:

V_b	vertical force due to permanent loads
V_t	vertical load for maximum torsion
V_s	vertical load for maximum shear
A	loaded area

3.3 Elastic and inelastic analysis

A shear wall (geometry see Fig. 3.4) with open and closed diaphragm was analysed and the results were compared with the strut-and-tie model of Schlaich et. al. [7]. The horizontal (ω_x) and vertical (ω_y) stresses are plotted. Among three types of loadings, only two cases, namely permanent loads and maximum shear are described below. The results for maximum torsion have not been included in this thesis due to the similarity with results for maximum shear. The inelastic analysis has been done only to show the principal load bearing behaviour. For comparison of the numerical values of Schlaich's model with that of finite element analysis see appendix C.

3.3.1 Evaluation of results for permanent loads

3.3.1.1 Shear wall with two supports and without opening

Horizontal stress ω_x : It is seen from the Fig. 3.13 that the top of the diaphragm has the greatest tensile stresses ($\omega_x \Omega 1.9 \text{ N/mm}^2$) as compared to the other parts of the diaphragm. The tension decreases from top approximately to the middle height of the shear wall. In the upper region the stress is approximately parallel to the top surface and then it shows an arch shape. The lower half of the shear wall is in full compression in horizontal direction.

Vertical stress ω_y : The top of the diaphragm is in full tension ($\omega_y \Omega 0.35 \text{ N/mm}^2$). The vertical stress distribution looks like a deformed V-shape up to 2/3 height of the shear wall (Fig. 3.15). In general, one can observe that the main load path

follows the diagonal sides but it extends deep into the shear wall with mild compression.

The principal stress diagram shown in Fig. 3.14 shows tension on the top of diaphragm and compression on diagonal sides.



Figure 3.13 Horizontal stress ω_x

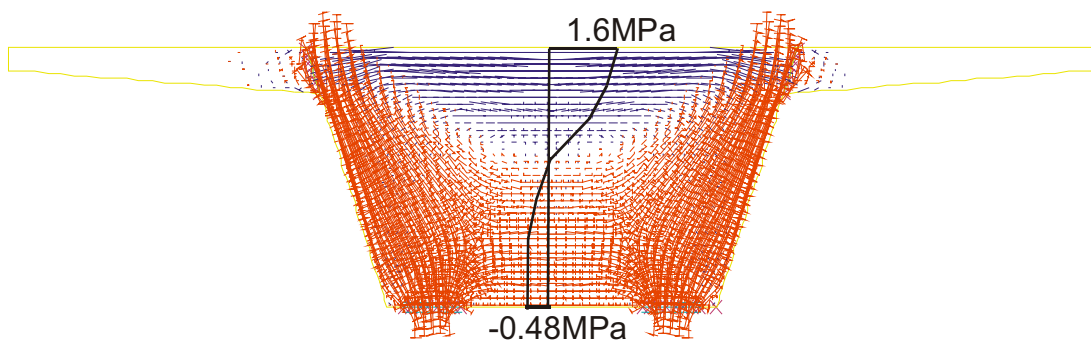


Figure 3.14 Principal stress diagram

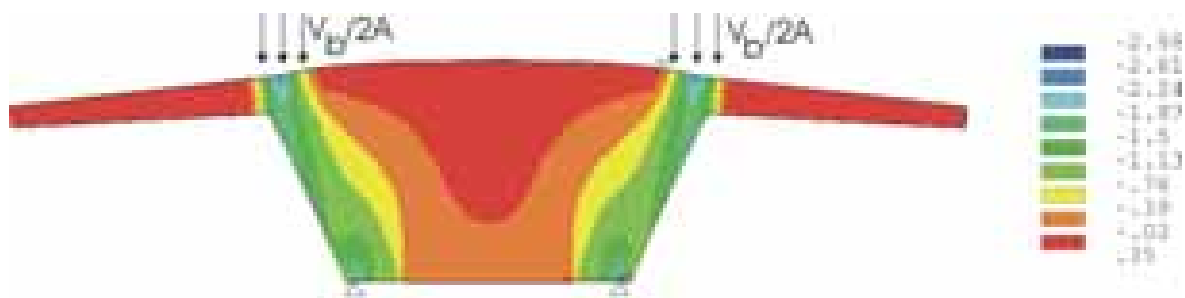


Figure 3.15 Vertical stress ω_y

3.3.1.2 Shear wall with two supports and with opening

Horizontal stress ω_x : The top of diaphragm is in tension ($\omega_x \approx 1.95 \text{ N/mm}^2$). Tension decreases from top to bottom. Tensile stresses are parallel to top of diaphragm and form a U-shape near the bottom edge of the opening. When the

FE-results are compared with the model developed by Schlaich et. al. (Fig. 3.18), the horizontal stress on top of diaphragm and near its vicinity gives good agreement with tension tie (T_1) of Schlaich's model at the same location. There is, however, no significant tensile stress on the lower part of diaphragm that can prove the importance of tensile tie (T_2) of Schlaich's model. Both diagonal sides and the bottom part of diaphragm are in full horizontal compression (Fig. 3.16).

Vertical stress σ_y : The top of diaphragm shows tensile stresses ($\sigma_y \approx 0.45 \text{ N/mm}^2$) and the tension extends to the vertical boundaries of the opening. This stress distribution reveals that there should be tension ties near the vertical edge of the opening but Schlaich's model (Fig. 3.18) never considers this force. The FE-results demonstrate that the load path follows the diagonal side and mild compression extends deep into the shear wall (Fig. 3.19).

The principal stress diagram in Fig. 3.17 shows tension on top part of diaphragm and vertical edge of opening. Compression is observed on the diagonal sides of the shear wall.

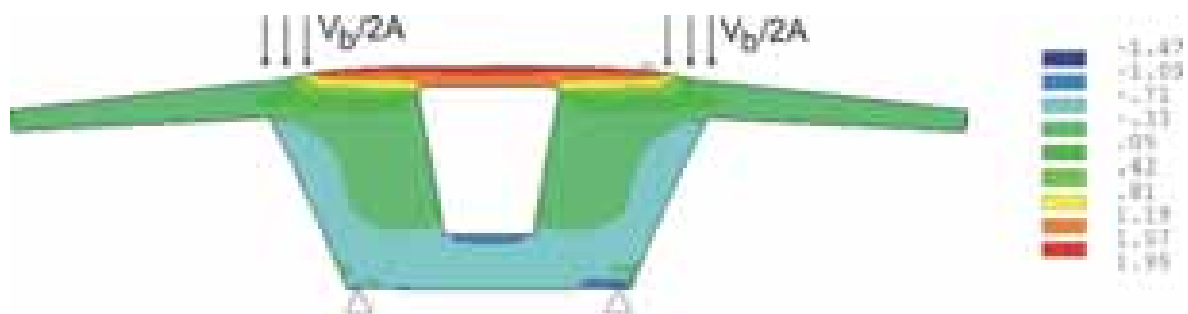


Figure 3.16 Horizontal stress σ_x

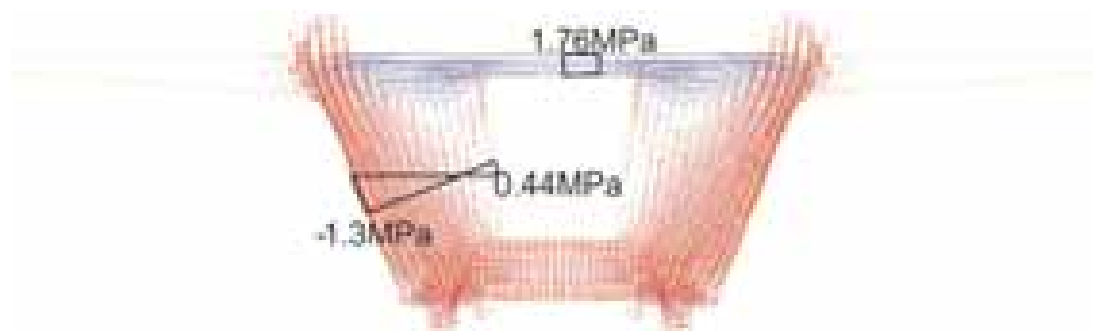


Figure 3.17 Principal stress diagram

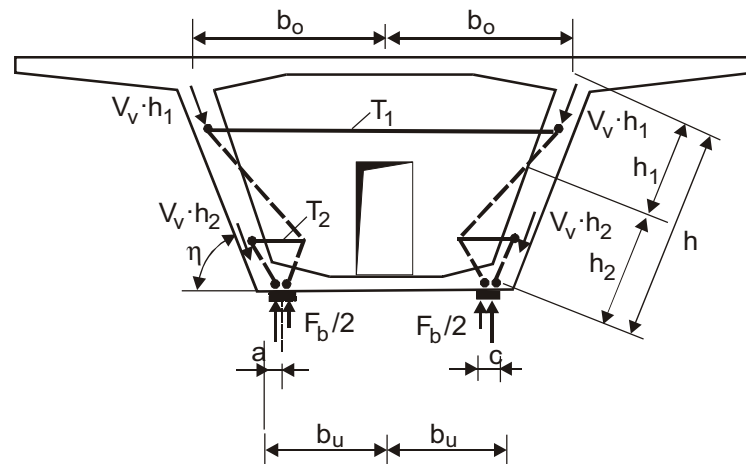


Figure 3.18 Schlaich's strut-and-tie model [7]

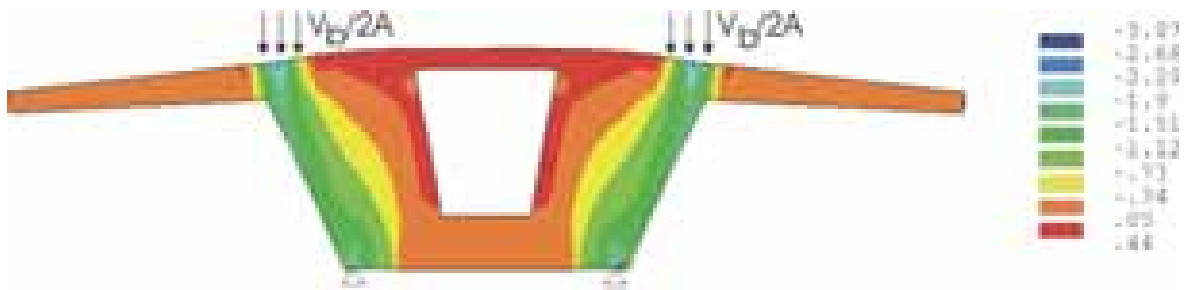


Figure 3.19 Vertical stress ω_y

3.3.1.3 Shear wall with central support and without opening

Horizontal stress ω_x : The magnitude of tensile stress ($\omega_x \approx 2.4 \text{ N/mm}^2$) on top of the diaphragm is high at the midspan and it decreases with increase in depth (Fig. 3.20). The distribution of tensile stresses is somehow curved at the upper part of the diaphragm and gives uniform compression in the lower part of the shear wall except for the greatest compressive stress near the central support. The horizontal stress distribution on top of the diaphragm and in its vicinity is similar to the tensile tie T_2 in Schlaich's model (Fig. 3.22).

Vertical stress ω_y : The segment is in full tension ($\omega_y \approx 0.35 \text{ N/mm}^2$) except for the diagonal sides and the area around the supports. It can be clearly seen that the load path follows the diagonal sides. The compressive stress above the support with inverted U-shape extends almost to $\frac{3}{4}$ height of the shear wall (Fig. 3.23).

Unlike to Schlaich's model (Fig. 3.22) tensile stresses in vertical direction extend from top to bottom of diaphragm. The external loads cause an inclined compression strut to the supports and tension perpendicular to it (e.g. in vertical direction).

Principal stress diagram in Fig. 3.21 shows tension on top of diaphragm and a diagonal tensile stress on lower parts of diaphragm. The bottle shape compressive stress is seen from diagonal sides of diaphragm to central support.



Figure 3.20 Horizontal stress σ_x

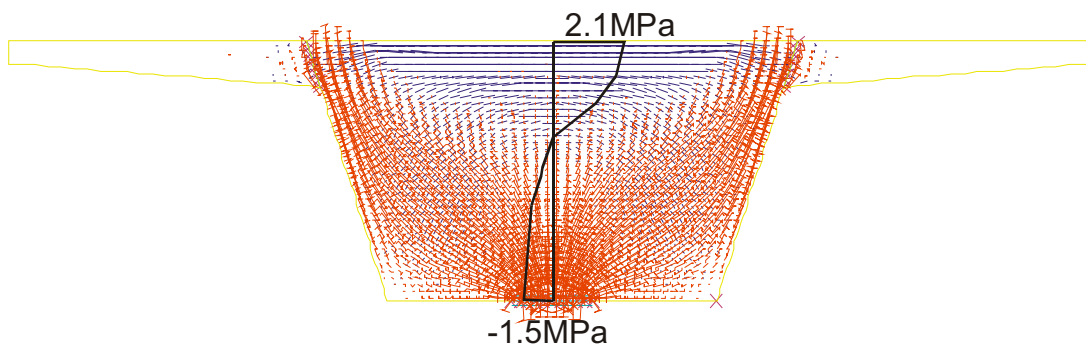


Figure 3.21 Principal stress diagram

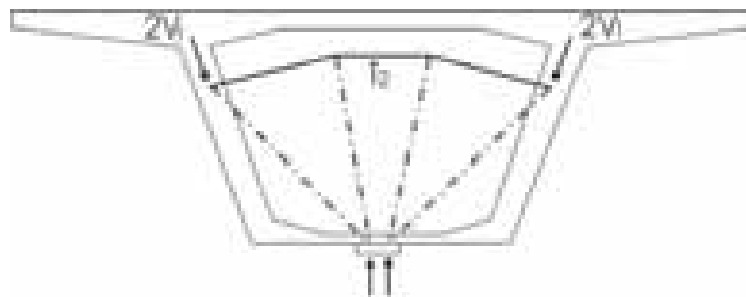


Figure 3.22 Schlaich's strut-and-tie model for diaphragm [7]

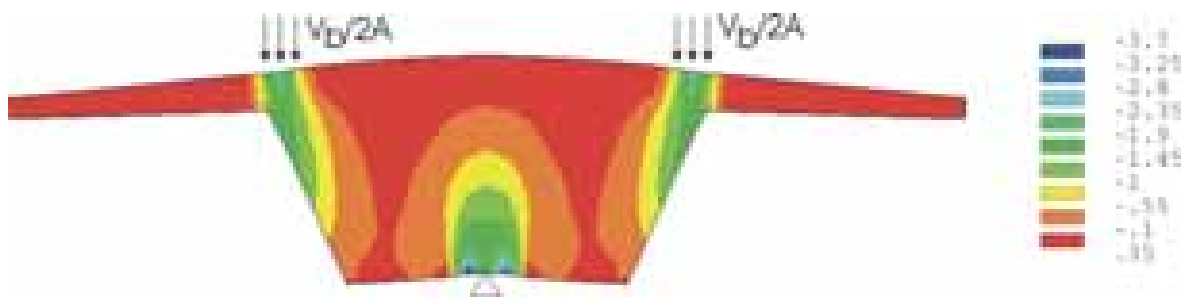


Figure 3. 23 Vertical stress ω_y

3.3.2 Evaluation of results for maximum shear

Here the finite element analysis has been conducted for both elastic and inelastic material behaviour. For elastic analysis, 25% of the total load was applied. When the load crosses this range cracks appear in the diagonal sides. For inelastic analysis the total load was applied. The loading for maximum shear has been done by distributing an appropriate portion of vertical force on top of the diagonal sides that could approximately give the corresponding torsional moment on the shear wall. The provided smeared reinforcement inside the volume elements in horizontal and vertical direction is $20 \text{ cm}^2/\text{m}$. A comparison of the tie forces of Schlaich's model with that of finite element analysis is given in appendix C.

3.3.2.1 Shear wall with two supports and without opening

Horizontal stress ω_x – elastic material behaviour: The tensile stress ($\omega_x \Omega 2 \text{ N/mm}^2$) on top of the diaphragm is greater on one side than the other, due to the unsymmetrical load arrangement for max. shear (Fig. 3.24). The curved shape tensile stress covers about 1/3 depth of the diaphragm from top. The remaining part of the diagonal sides and the diaphragm are in compression. The tensile stress distribution on the diaphragm agrees with horizontal tension tie T_1 of Schlaich et. al. model (Fig. 3.25).

Horizontal stress ω_x – inelastic material behaviour: As compared to that of elastic analysis, the top of the diaphragm has high tension ($\omega_x < 5 \text{ N/mm}^2 - f_{ct}$) on the right side that extends diagonally to left side (Fig. 3.27). The left diagonal side shows high compression in horizontal direction. Approximately the lower 2/3 part of diaphragm is in horizontal compression.

The principal stress diagram (Fig. 3.26) shows high tension on top of diaphragm and moderate tension on the lower part of diaphragm. Compressive stress is greater on the left side than on the right one due to shear load arrangement.

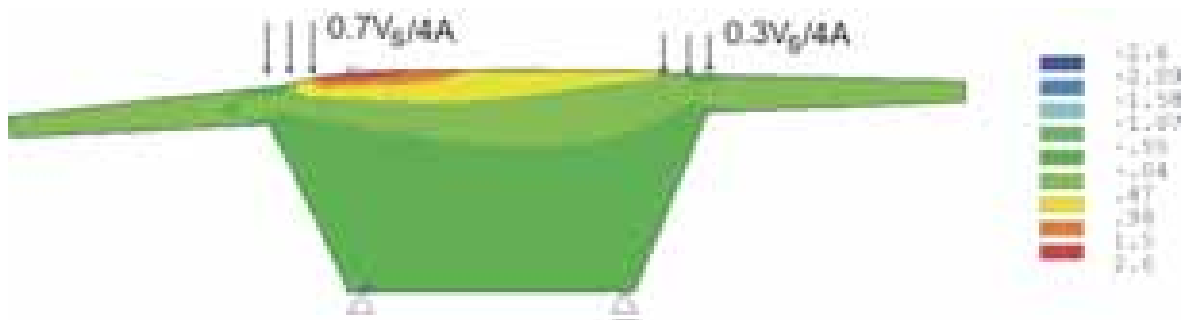


Figure 3. 24 Horizontal stress ω_x - elastic material behaviour

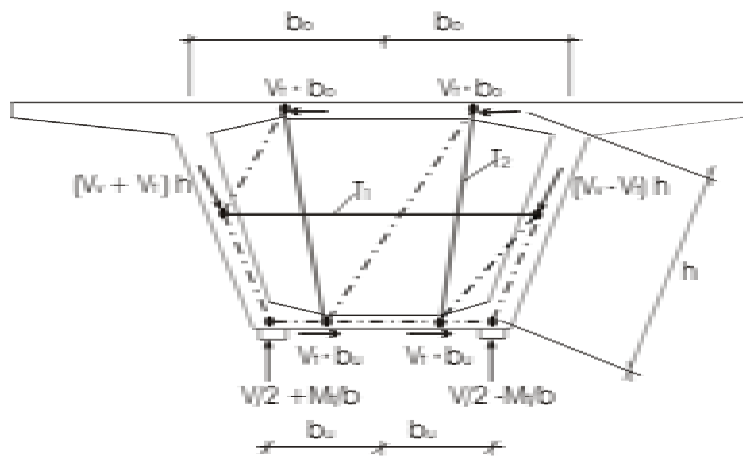


Figure 3. 25 Diaphragm strut-and-tie model for shear and torsion [7]

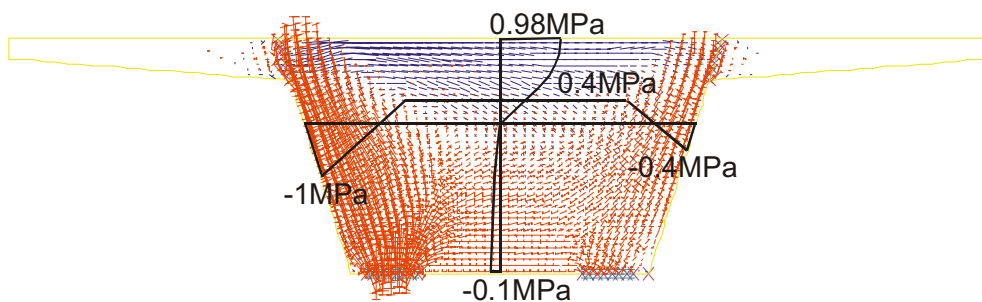


Figure 3. 26 Principal stress diaphragm

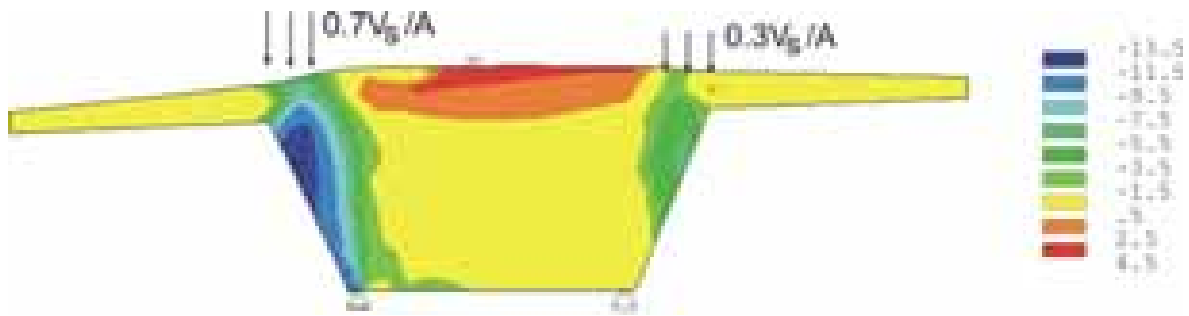


Figure 3.27 Horizontal stress ω_x - inelastic material behaviour

Vertical stress ω_y - elastic material behaviour: Fig. 3.28 shows that the load follows the path from top to bottom and extends into the shear wall like curved shape compressive stress. Due to load arrangement for max shear, distribution of the stress on the left and right diagonal sides is not uniform. The remaining part of the segment is in full tension. The vertical tension that extends from top of diaphragm to bottom is in agreement with the vertical tension tie T_2 of Schlaich's model (Fig. 3.25).

Vertical stress ω_y - inelastic material behaviour: In comparison to the elastic analysis, the compressive stress is highly concentrated on the left side (Fig. 3.29). The compressive stress distribution on both diagonal sides is not uniform due to load arrangement for max shear. From the left diagonal side the load somehow diffuses into the shear wall. A low concentration of compressive stresses can be seen in the right diagonal side. The other parts of shear wall are in full tension in vertical direction.

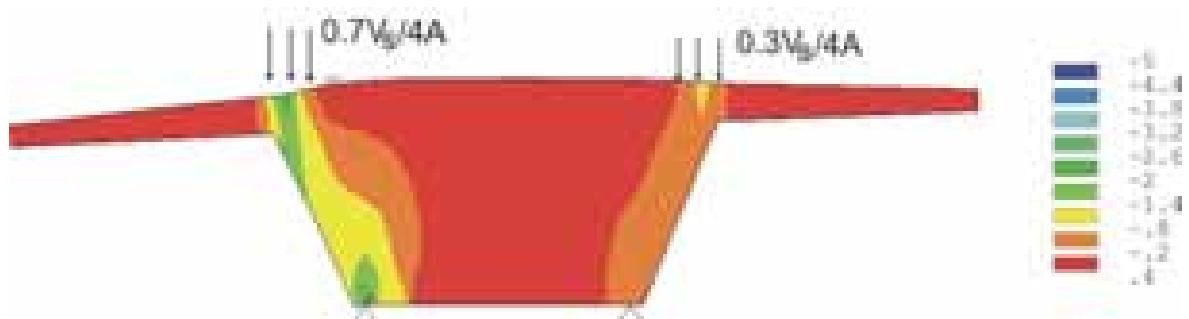


Figure 3.28 Vertical stress ω_y - elastic material behaviour

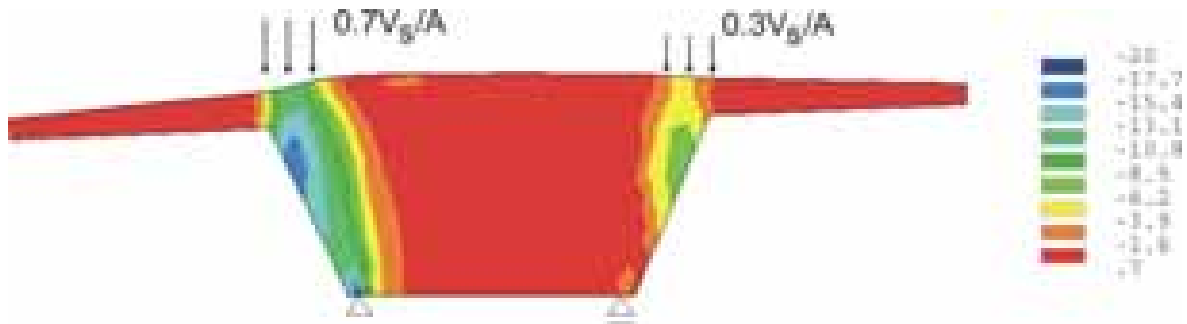


Figure 3.29 Vertical stress ω_y - inelastic material behaviour

3.3.2.2 Shear wall with two supports and with opening

Horizontal stress ω_x – elastic material behaviour: Due to applied load arrangement for max shear, the tension stress on top of the diaphragm is greater on one side and is somehow parallel to each other (Fig. 3.30). It shows minor tension around the vertical edge of the opening. The other part of the shear wall shows non-uniform compression.

Horizontal stress ω_x – inelastic material behaviour: It shows uneven stress distribution in the whole shear wall (Fig. 3.31). But due to load arrangement for max shear, high compressive stresses are seen at the left diagonal side.

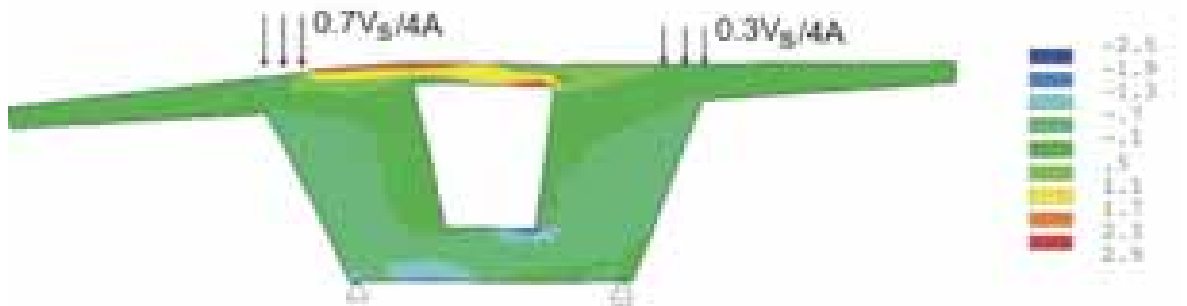


Figure 3.30 Horizontal stress ω_x - elastic material behaviour



Figure 3.31 Horizontal stress ω_x - inelastic material behaviour

Vertical stress ω_y - elastic material behaviour: The tensile stress that starts at top of the diaphragm has a minor depth at the right part of the shear wall (Fig. 3.32). It almost covers the whole depth near the left vertical edge of the opening. The compressive stress diffuses from the left side into the diaphragm.

Vertical stress ω_y - inelastic material behaviour: Due to load arrangement for max shear, the left diagonal side is more compressed than the right one (Fig. 3.33). Some compressive stresses are also seen at the right vertical edge of the opening. The compression is more concentrated at the diagonal side if a nonlinear material behaviour is used than for an elastic material.

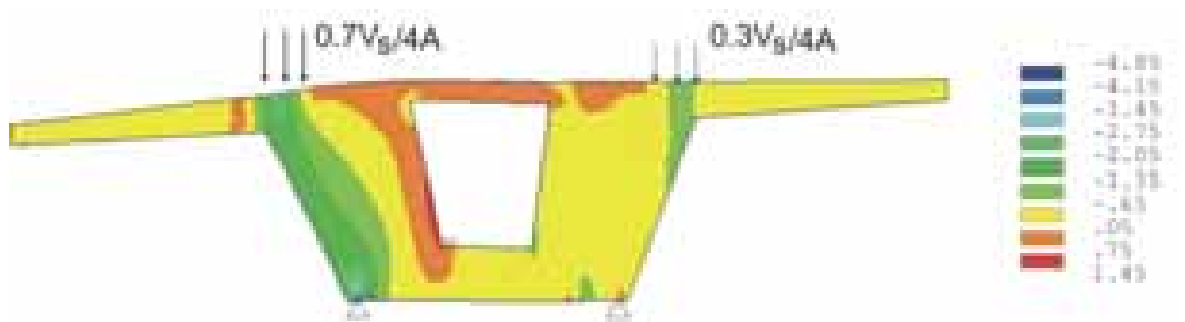


Figure 3.32 Vertical stress ω_y - elastic material behaviour

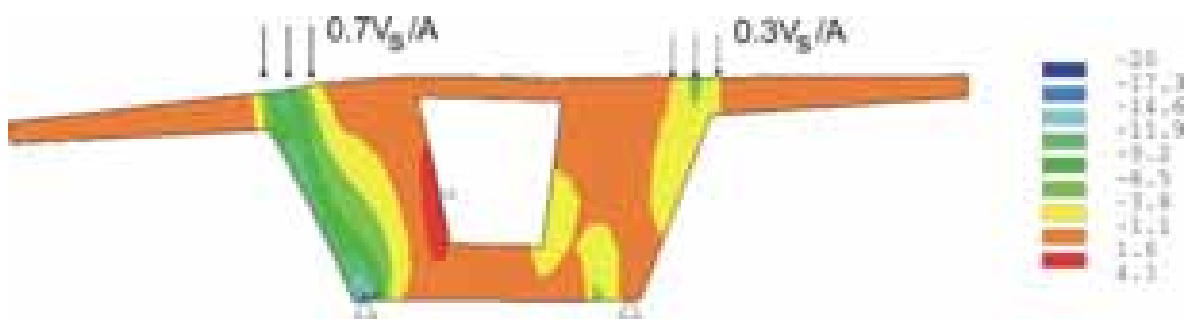


Figure 3.33 Vertical stress ω_y - inelastic material behaviour

3.3.3 Crack formation due to maximum shear loading

3.3.3.1 Shear wall with two supports and without opening

Due to load arrangement for max shear, the crack distribution is not uniform on the diagonal sides and top of diaphragm. The cracks on the left diagonal side cover the whole length whereas it extends only to mid height of the right side (Fig. 3.34). lateral strain that is contributed due to support reactions and vertical forces on top causes the cracks on the diagonal sides. The cracks on the upper left side of

diaphragm are caused by tensile stresses. Due to the smeared crack approach of the finite element model the location, orientation and the sizes of cracks can not be determined exactly in inelastic analysis.

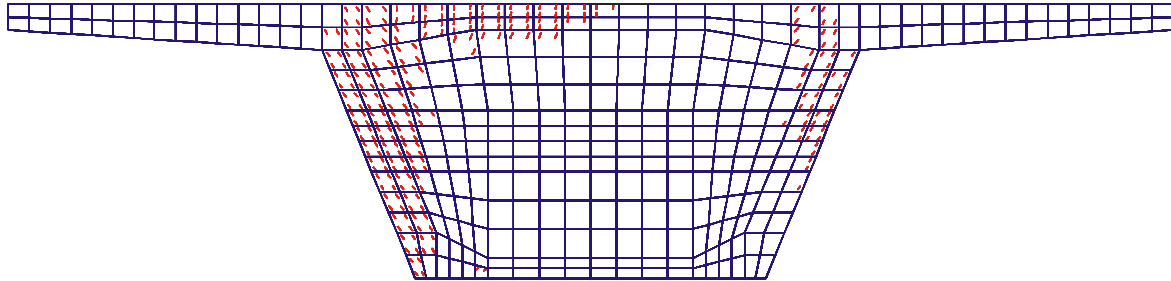


Figure 3.34 Crack distribution

3.3.3.2 Shear wall with two supports and with opening

In contrast to the shear wall without opening, here the cracks cover almost the whole top of the diaphragm and diagonal sides (Fig. 3.35). The high vertical force on top and the support reactions results in lateral strain that causes the cracks on the diagonal sides. The cracks on the top slab are due to tensile stresses. Uplifting action of the diaphragm from external load and support reaction causes cracks on the left part of the opening. There is a high concentration of cracks on the left diagonal side and at the centre of the top of diaphragm.

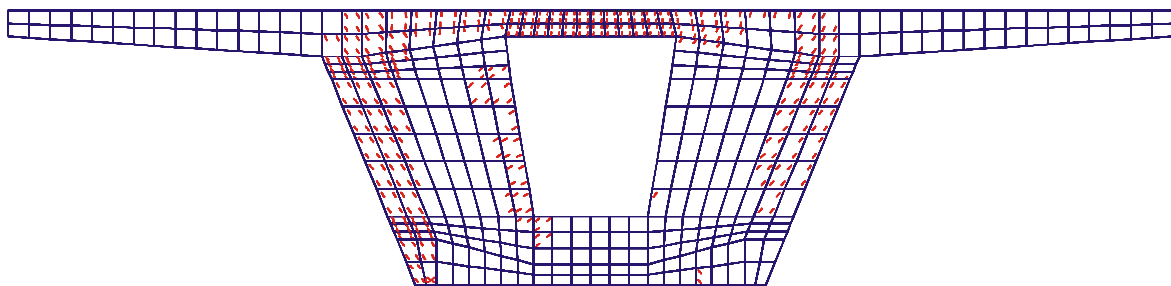


Figure 3.35 Crack distribution

3.3.4 Summary

Generally the load flows from top of the diagonal sides to the supports, however there are some diffusions of the load from the diagonal sides to the adjacent diaphragm. The numerical analysis demonstrate that the strut-and-tie models developed by Schlaich et. al. do not consider all load paths. The results can be summarised as follows:

The model developed for shear wall with two supports and open diaphragm under pure shear has a redundant tie force in the lower part of diaphragm. But it does not capture the tensile force near the opening that extends from top of diaphragm to the bottom as shown in the finite element analysis. So, it should be revised and refined.

The model developed for a shear wall with central support and closed diaphragm shows that there is a sufficient tie force on the upper part of diaphragm, but it does not include the tensile force in diagonal direction caused by vertical load and support reaction shown in finite element result. So, an additional tie force should be added.

The model for shear wall with two supports and closed diaphragm under shear and torsion loading shows a very good agreement with finite element results both in horizontal and vertical directions. Therefore one can conclude that the strut-and-tie models are correct.

A refinement of Schlaich's models will be conducted based on an elastic analysis. This will be described in chapter 6 of this dissertation. The inelastic analysis has been done to study the principle stress distribution of the shear wall under ultimate loads. The results from inelastic analysis cannot be considered for the development of strut-and-tie model due to the difficulty to trace the load paths in side the shear walls.

4 3D-finite element model of an existing segmental bridge

4.1 Modeling

A 2-dimensional analysis of diaphragms done in the previous chapter is a simplification of the real 3-dimensional behaviour of the structure used in practice. For example the loads are applied on top of “webs” of the diaphragm whereas in reality, the vertical forces are somehow distributed over the web area. Furthermore the 3-D behaviour is not considered, like the inclined compression strut due to shear forces. Also the forces for tendons, which are anchored into the diaphragm are ignored. So in this chapter, a 3-D model of a whole segmental bridge will be evaluated and the forces and stresses in the pier segment will be analysed.

Another purpose of the 3-D analysis is the calculation of the stresses in the first joint. A field practice in some of segmental bridge construction shows that there was opening of the first joint on the flanges of the top slab. So far the stresses on the first joint has not been investigated by scientific research. For this purpose and other investigations, a 3-D finite element model of a 43.25 m long segmental bridge was developed based on a standard span constructed in Bangkok as Second Stage Expressway (Figs. 1.7-1.9, and 4.2). The bridge consists of 12 segments having uniform length of 3.4 m (9 standard and 3 deviator segments) each and 2 pier segments each with 1.5 m (diaphragm thickness 1m). The first two and the last two segments in pier regions are modelled by 3-D volume elements (solid65) but the rest of the segments are modelled by 2-D plane shell elements (shell43) for reasons of simplicity (Fig. 4.1).

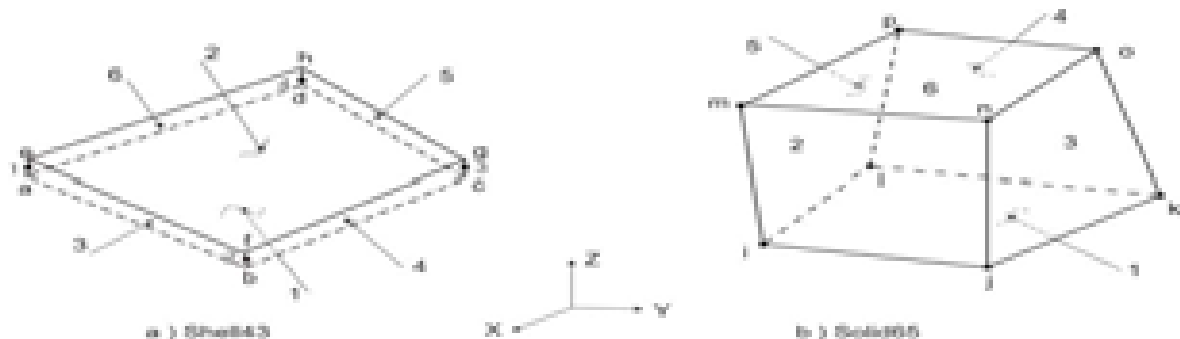


Figure 4.1 Types of elements [17]

The joints between two segments are modelled by contact elements called 'contact52' to consider the opening of the dry (not glued), unreinforced joints. The nodes at the joints between the 3-D and 2-D elements are rigidly coupled.

The external tendons are modelled by 'link8' element. These elements are attached to the deviators in y- and z-directions (Fig. 4.2) but are free to move in longitudinal direction. They are fixed in all directions where the anchorage plate is located. Tendon elements are coupled to four nodes of a concrete element for simplicity to avoid the modelling of the anchor plate and all related problems.

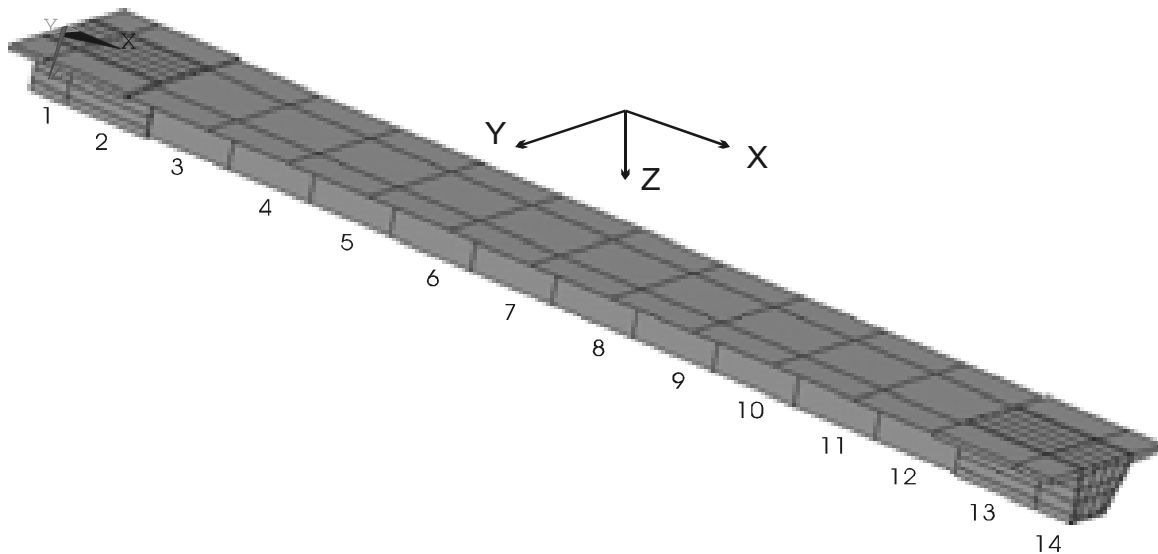


Figure 4.2 Segment arrangement

Solid65-volume element has eight nodes. Each node has three degrees of freedom (translations in the nodal x, y, and z directions) (Fig. 4.1). As mentioned above, two pier and standard segments are modelled by volume elements.

The 3-D finite element model of pier and standard segments are shown in Figs. 4.3 through 4.5.

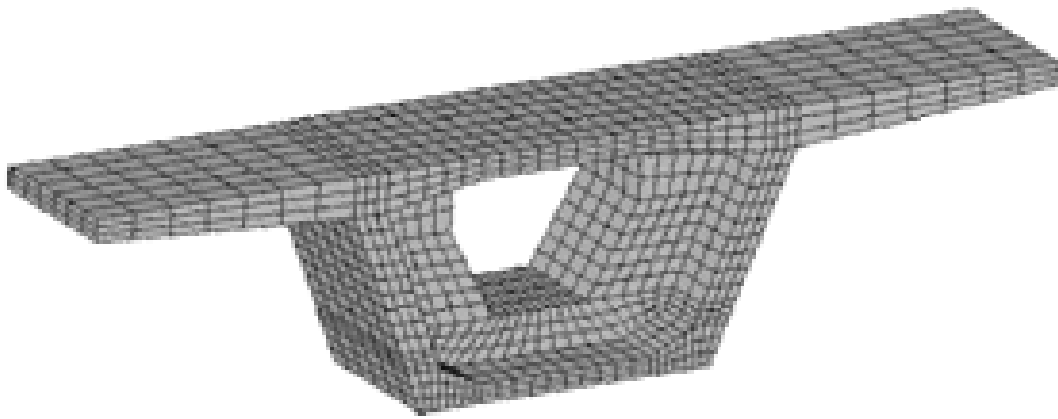


Figure 4.3 Pier segment with open diaphragm

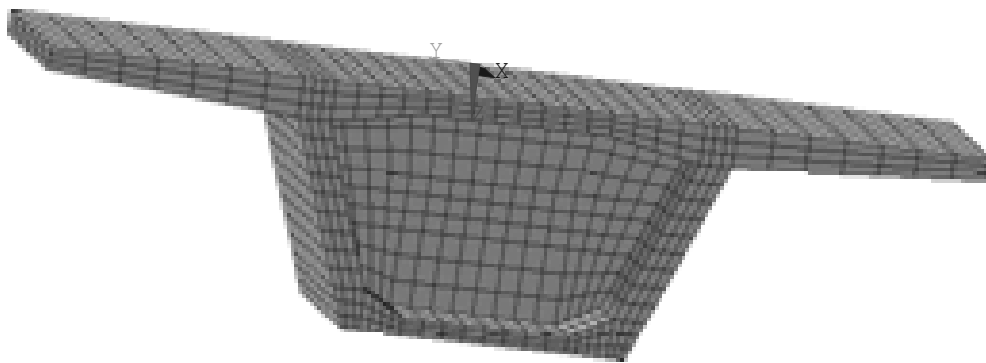


Figure 4.4 Pier segment with closed diaphragm

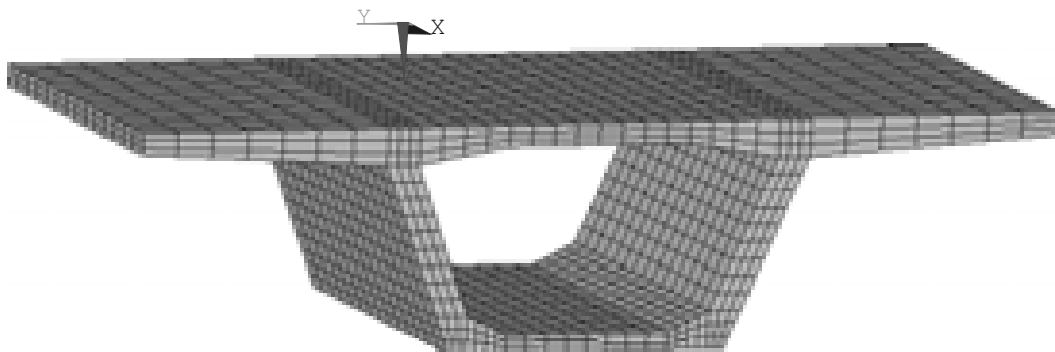


Figure 4.5 Standard segment

The plane “Shell43”-element has 4 nodes with six degrees of freedom at each node: translations in the nodal x, y, and z-directions and rotations about the nodal x, y and z-axes. The deformation shapes are linear in both in-plane directions. Segments 3 up to 12 are modelled by 2D-plane element ‘shell43’.

The finite element mesh of the whole superstructure is shown below

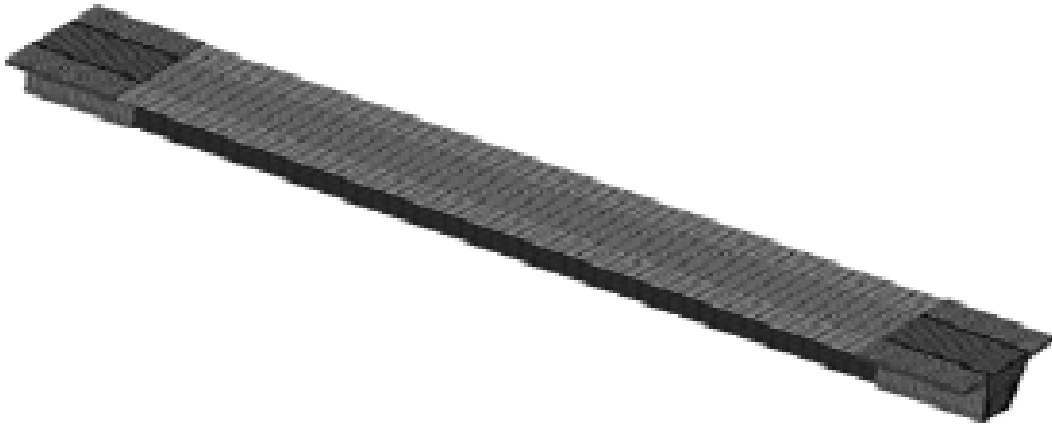


Figure 4.6 Finite element model of the superstructure

The “Contact52” element has been selected to model the dry joint between two segments. Basically it represents two surfaces that can form break or physical contact and may slide relative to each other. The element has an ability to support only compression in the direction normal to the surfaces and shear (coulomb friction) in the tangential direction. The element has three degrees of freedom at each node: translations in the nodal x, y, and z directions.

First the element is preloaded in normal direction and the gap specification is given as a tool to avoid numerical instabilities. A specified stiffness acts in the normal and tangential directions when the gap is closed and not sliding.

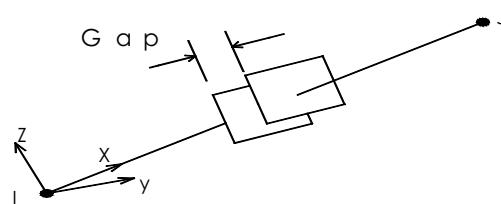


Figure 4.7 3-D point to point contact element [17]

The geometry, node locations and local coordinate system for this element are shown in Fig. 4.7. The element has two nodes, two types of stiffnesses; normal stiffness (KN) and sticking stiffness (KS), an initial gap or interference (GAP), and an initial element status that determines whether the gap is closed and sliding or closed and not sliding or open.

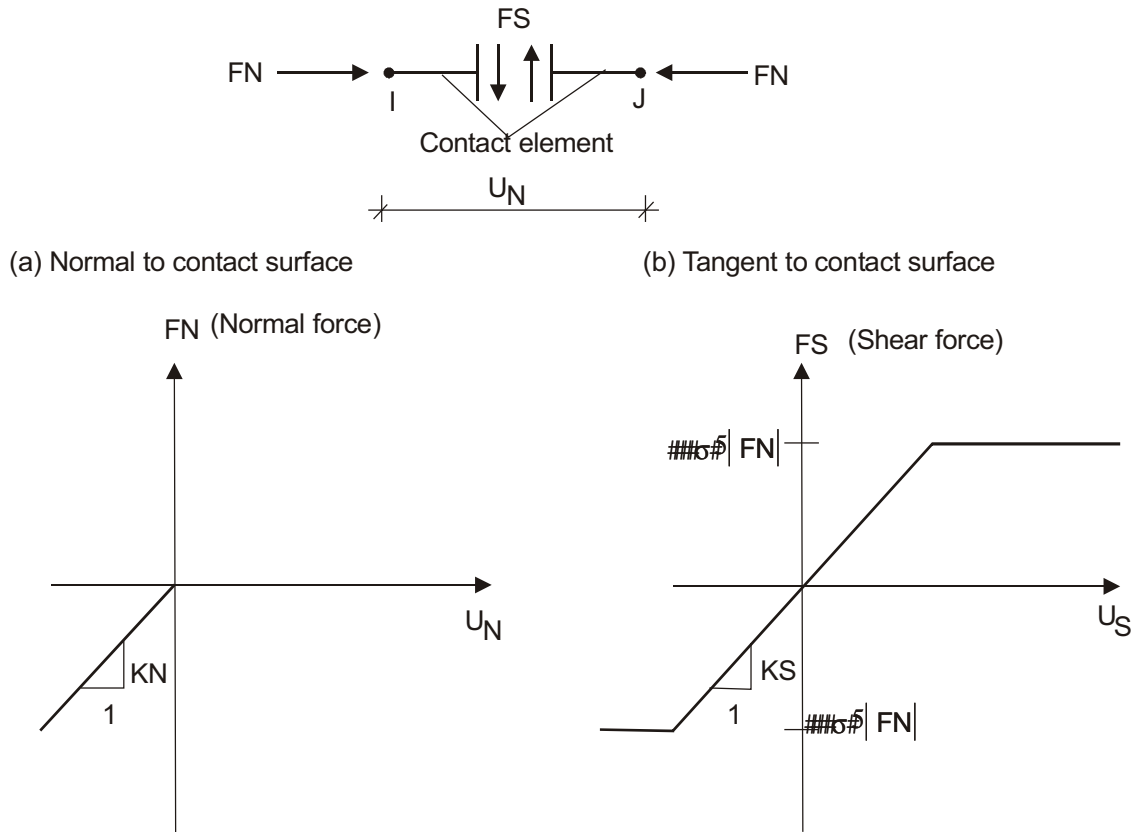


Figure 4.8 Force-deflection relationship of “Contact52” element [17]

As mentioned before, 3 different ‘material’ parameters (KN , KS , GAP) are required. KN should be large enough to keep the model from over penetration, but it should not be so large that it causes ill conditioning. For the most contact analyses, values for KN can be estimated as follows:

$$KN = f (E h) \dots\dots\dots (4.1)$$

Where:

f = Factor that controls contact compatibility. This factor will usually be between 0.01 and 100; $f = 1$ is the default value.

E = Young’s Modulus of the concrete

h = Characteristic contact “length”. The value, which has to be used, depends on the particular geometry of the problem: In 3-D configurations, h should be equal to a typical target length (that is, the square root of the target area) or a typical element size.

Table 4.1 Material parameters used in FE-analysis

Friction coefficient σ	Normal stiffness KN	Sticking stiffness KS
0.7	$E_c h $ 1.032E10 ⁸ N/mm	1500 N/mm

Link8 element is a three-dimensional spar that can be used in a variety of engineering applications. It may be applied for a truss element, a cable element, a link element, a spring element, etc. In this analysis it is used as a cable element to represent the tendons. The spar element is assumed as uniaxial tension-compression element with three degrees of freedom at each node: translations in the nodal x, y, and z-directions. As a pin-jointed structure, no bending of the element is considered. Plasticity, creep, swelling and stress stiffening capabilities are included but not considered in the analysis.

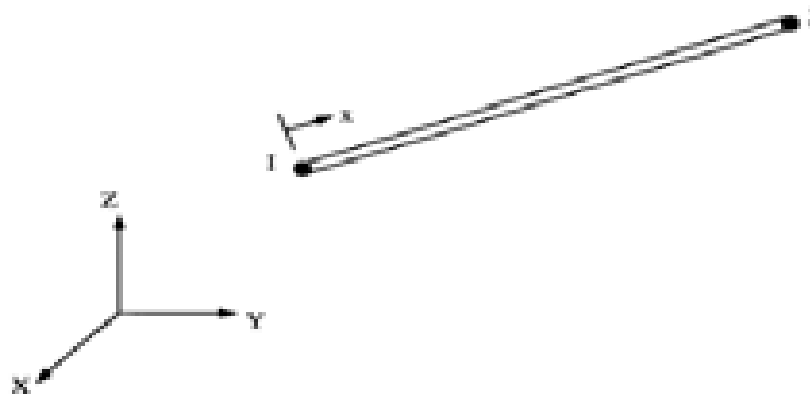


Figure 4.9 “Link8” 3-D spar element [17]

4.2 Verification

Due to geometrical and material non-linearities, verification of the model is very important. The results of the FE-analysis are compared with data from a full-scale destructive test of a precast segmental hollow box girder bridge with dry joints and external tendon carried out by Takebayashi et al [6]. The externally prestressed segmental bridge had a span length of $l = 43.25 \text{ m}$. The test was conducted before the construction of the Second Stage Expressway System (SES), which consist of approximately 32 km of elevated roads in the city of Bangkok (Thailand). The purpose of the test was to study the deformation characteristics such as deflection, joint opening, tendon slip at deviators, concrete and tendon strains at various load stages.

The test span was designed in accordance with the specification in AASHTO: the standard specifications for highway bridges of 1983 [30] and the guide specification for segmental bridges of 1989 [5]. The deck was 10.2 m wide and consisted of 14 segments (Figs. 1.7 to 1.9). The external tendons were formed from 12k15 or 19k15 strands grade 1770/1860 protected by high density polyethylene ducts (HDPE) and cement grout.

Steel billets were used as the imposed load for the test. They were stacked up in two-load area (A and B) so that the top slab at the mid span area could be monitored conveniently (Fig. 4.10). Each billet was 347 kg, and five were handled at a time by crane.

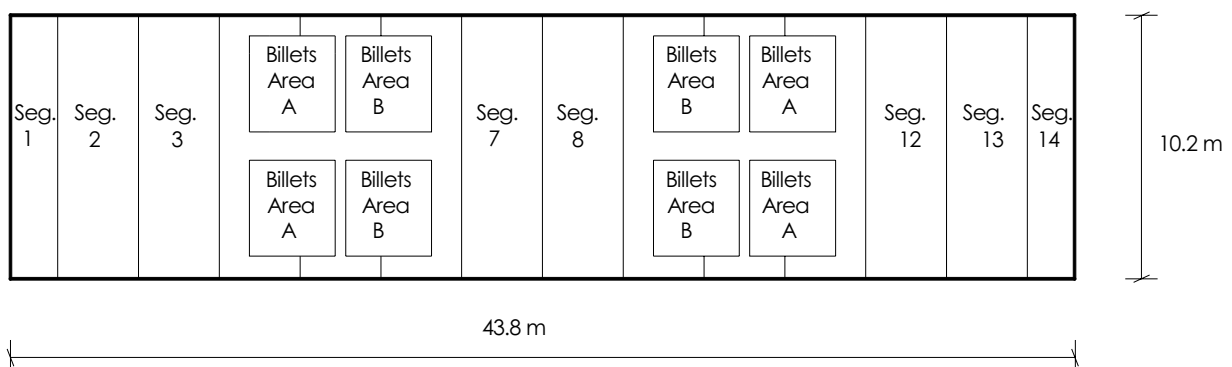


Figure 4.10 Loading arrangement: top view [6]

The evaluation for deflection of the test and FE-calculation is shown in Fig. 4.11. As long as all joints are closed, the first part of deflection curve is linear. But when the joints start to open, an abrupt change of the slope can be observed.

From Fig. 4.11 it can be seen that the mid span deflection of FE-calculation shows very good agreement with test result. So, it can be concluded that the developed FE-model of the segmental bridge can simulate the real behaviour of the segmental bridge. Therefore it will be used to analyse different load cases.

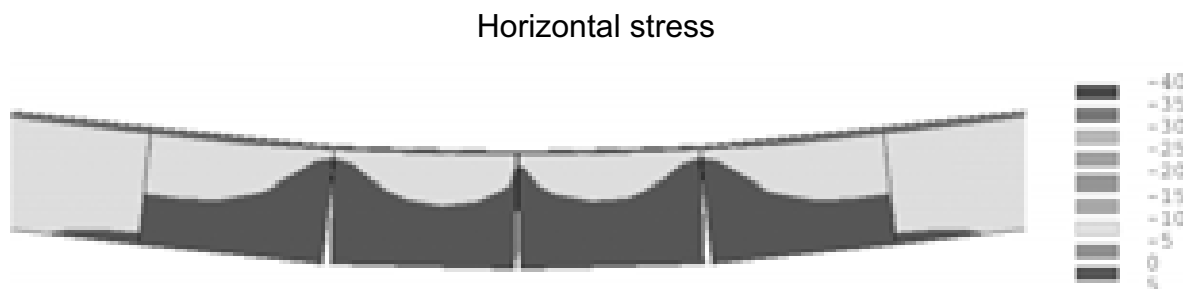
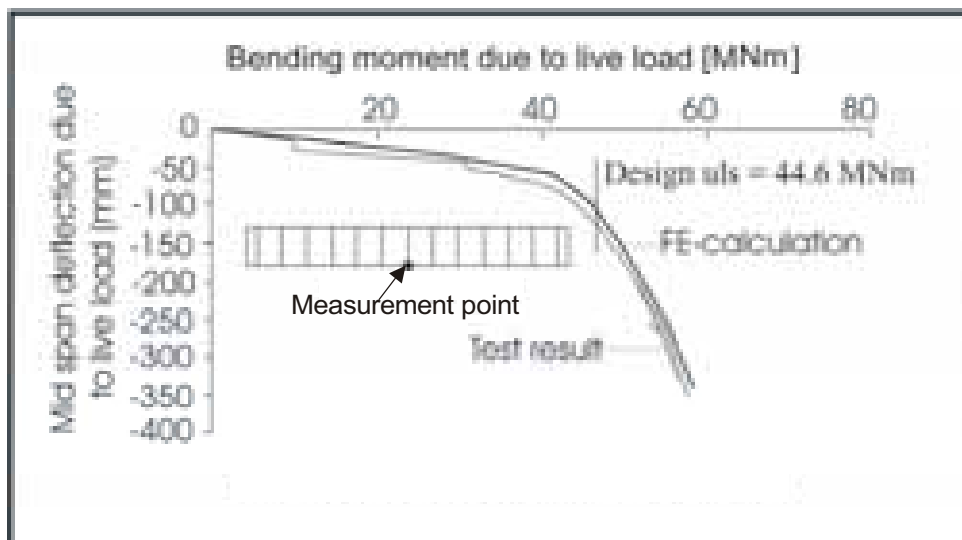


Figure 4.11 Comparison between test and FE-results resp. joint opening

4.3 Dimensions, loads and prestressing

- Dimensions of the structure (Figs. 1.7 to 1.9)

The measurements are taken from the segmental bridge that had been constructed for test in Bangkok. ($l = 43.25$ m, $w = 10.2$ m and $h = 2.4$ m.)

- Loads

The following different types of loading were used for the analysis: self weight ($g_{1k} = 123.93 \text{ KN/m}$), imposed loads (asphalt pavement, cap and railing) ($g_{2k} = 34.3 \text{ KN/m}$) and live load. The vertical live load was evaluated by selecting load model 1 according to EC 1-3, 4.3.2. The number of notional lanes n_l were determined according to EC 1-3, 4.2.3 (Tab. 3.1). For the given carriage way width of $w = 10.2 \text{ m}$ and width of a notional lane of 3 m , the number of notional lanes becomes $n_l = \text{Int}(w/3) = 3$. The width of the remaining area is $10.2 - 3 \times 3 = 1.2 \text{ m}$.

The same load combinations for maximum torsion and maximum shear are taken as in the case of the 2-D analysis (Figs. 3.8 and 3.9). Thus the load arrangement in transverse direction is given. The longitudinal load arrangement of the bridge is shown in Fig. 4.12. The double axle loads (Q_{ik}) have been distributed uniformly over an area of 7.2 m width and 1.6 m length for simplicity.

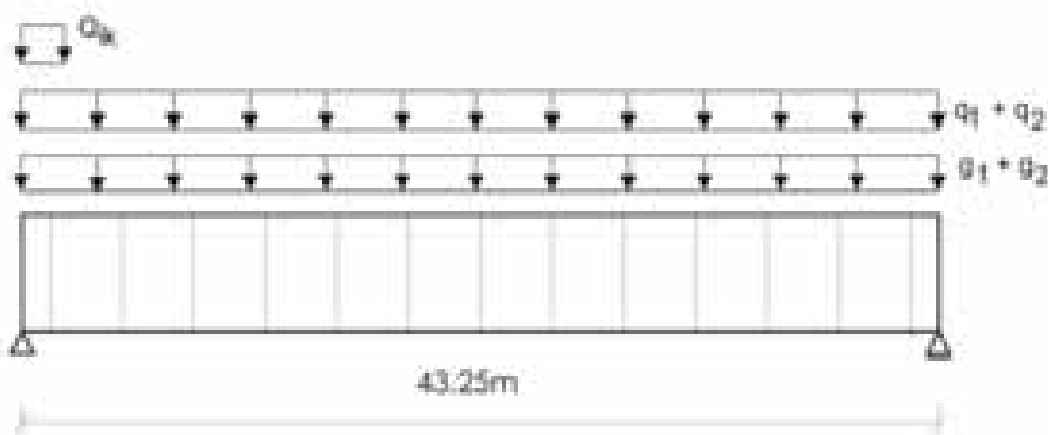


Figure 4.12 Load arrangement in longitudinal direction (max shear)

- Prestressing

The arrangement of tendons inside the hollow box was in accordance with Second Stage Expressway in Bangkok (Fig. 1.8). Internal prestressing usually brings a big corrosion problem in the joints of the segments, so the prestressing was conducted externally. Here the tendons were externally covered by HDPE ducts and cement mortar was injected inside the duct to

avoid steel corrosion. The tendons were anchored on two pier segments and their deviations were done at three places on special types of segments called deviator segments (Fig. 1.9). The partial safety factor of prestressing is “1” for load combination in ultimate limit state according to EC 2-1 given in equation 4.2.

$$1.35 (G_k + \div G_k + Q_k) + 1.0P \dots\dots\dots (4.2)$$

Where:

- G_k g_1 self weight
- $\div G_k$ g_2 imposed load
- Q_k q_{ik}, Q_{ik} variable live load
- P prestressing loads

4.4 Finite element analysis of the bridge

For the following FE-analysis the concrete is assumed to behave fully elastic. Three different load cases are considered namely permanent loading, maximum torsion and maximum shear. As the investigations are focused on the behaviour of the pier segments, only the results of these segments are described below. Two different types of pier segments, one with closed and other with open diaphragm, are analysed. The horizontal and vertical stresses ω_x resp. ω_z for the pier segments and the vertical and horizontal stress distributions on the first joint are illustrated.

4.4.1 Permanent loading

4.4.1.1 Pier segment without manhole

Vertical stress ω_z (Fig. 4.13):

The front side of the pier segment where the tendons are anchored is mostly in vertical compression except for the upper part of diaphragm that is in tension. Compressive stress is more prominent in the lower part of the segment near the

support region. Tensile stresses ($\omega_z \approx 4.5 \text{ N/mm}^2$) are also observed adjacent to the support and the top slab.

The opposite side of the diaphragm is uniformly tensioned almost in the entire area of it due to diverging force from the tendon except for the upper parts of the diaphragm, which is in compression. The top slab is predominantly in slight tension except for minor compression near the first joint.

The stress distribution in the first joint is non-uniform. This is due to the eccentricity of the tendon force at the front face of the diaphragm. The flanges of the top slab are in compression but prominent at the intersection between web and flange. Part of the top slab in between two webs is also in compression. Intensity of compressive stress on the webs decreases with section depth.

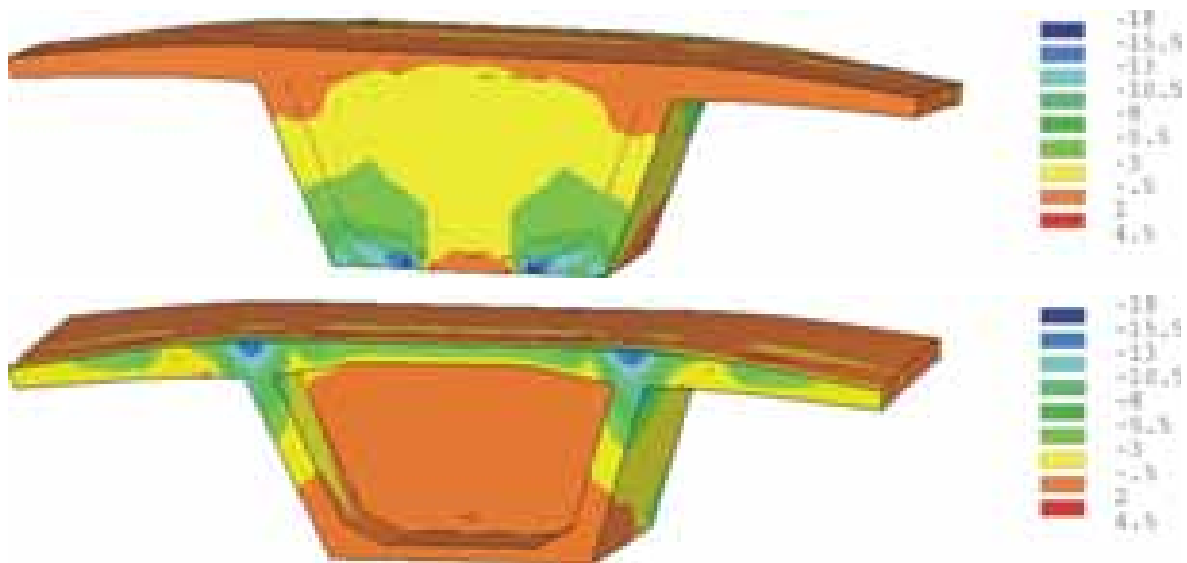


Figure 4.13 Vertical stress ω_z for front and opposite face of pier segment in permanent loading

From principal stress diagram (Fig. 4.14) it can be seen that the forces flow from the flanges to the webs and from the webs to the supports or these extends to diaphragm. Also the forces flow from the top slab along its length to the webs. Finally the load reaches the supports from all directions.

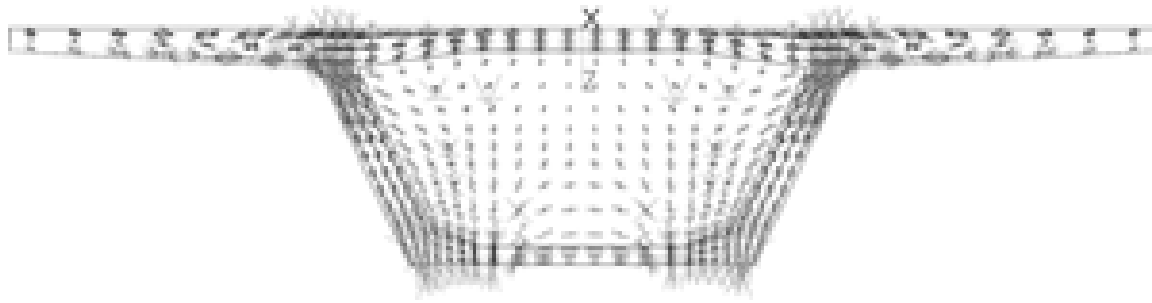


Figure 4.14 Principal stresses for closed diaphragm in permanent loading

Vertical stress ω_z on first joint (Fig. 4.15):

The stress distribution is symmetric due to the symmetric load arrangement. The top slab shows a non-uniform compressive stress distribution. The compressive stress in the top slab increases linearly from two extremes sides of the flange to the middle. Then it changes its course abruptly at the junction between flange and webs. The maximum compressive stress is seen at the junction points. The stresses in the top slab in between two webs are more or less uniform.

The compressive vertical stress distribution on the web is also non-uniform. The stress intensity is high near the junction between top slab and webs and then it decreases from this area to the central regions. This is due to load from the whole bridge that flow diagonally from upper part of the structure to support and the arrangement of prestressing force on the upper part of diaphragm. On the bottom slab very minor irregular tensile stresses are observed.

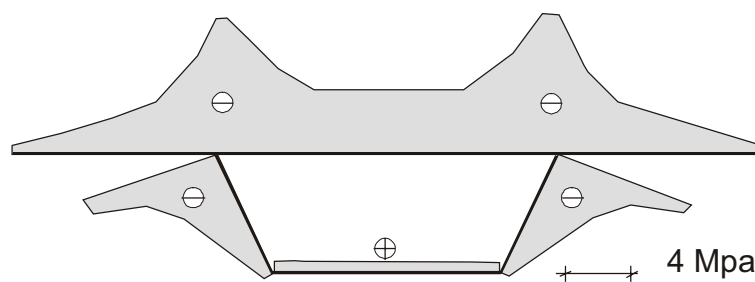


Figure 4.15 Vertical stress ω_z in the first joint for permanent loading

Longitudinal stress ω_x on the first joint (Fig. 4.16):

The stress distribution is symmetric due to symmetric load arrangement. The top slab is predominately compressed except at the tip of the flange that is in minor

tension. The compressive stress increases from tip of the flange to central part of top slab. The web and bottom slab are in full compression.

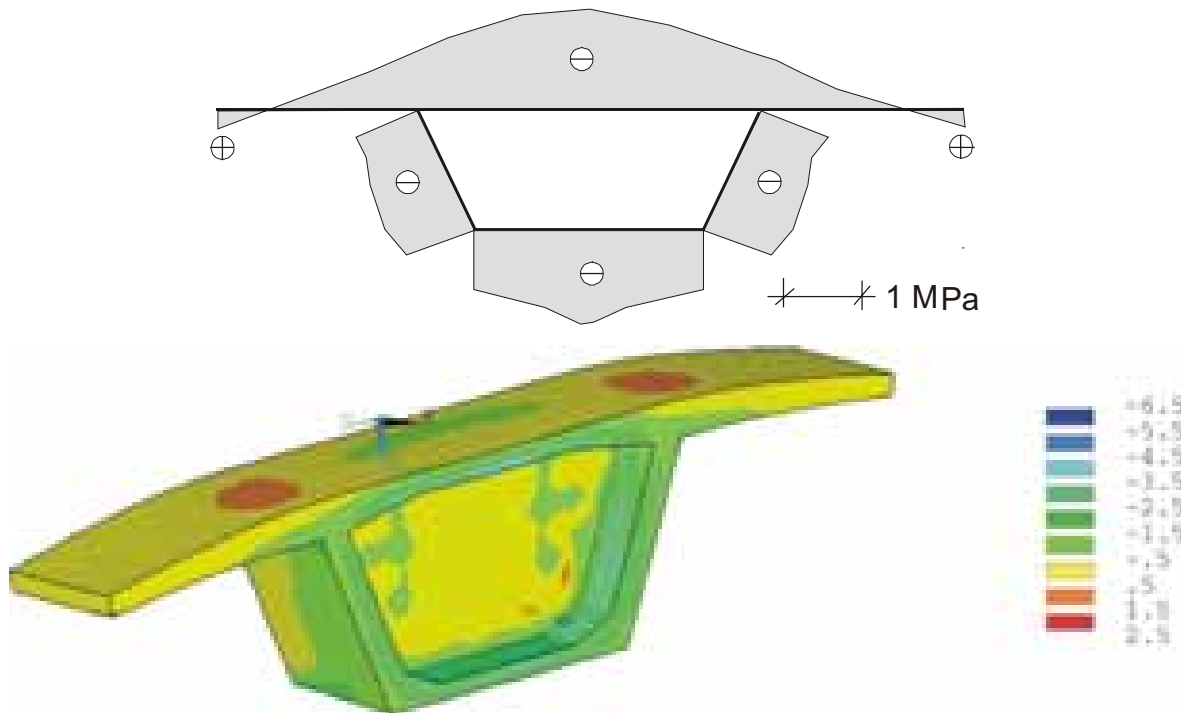


Figure 4.16 Stress ω_x on the first joint for permanent loading

4.4.1.2 Pier segment with manhole

For vertical stress ω_z (Fig. 4.17):

The front face of the pier segment shows compression (Fig. 4.17 top). The intensity of compressive stress is not uniform on the whole face of the diaphragm and the web. The intensity is mild on the top but increases with depth. The range of intensity of compression is similar on the top slab and in the bottom slab in between two supports.

The middle part of the opposite face of diaphragm shows tension on both sides of the manhole (Fig. 4.17 bottom). The intensity of compression on the first joint is less as compared to the pier segment without manhole. Generally the top slab on the first joint is in compression. High compression is observed at the intersection between the flanges and the webs. Also the web is more or less in compression and its intensity decreases with section depth.

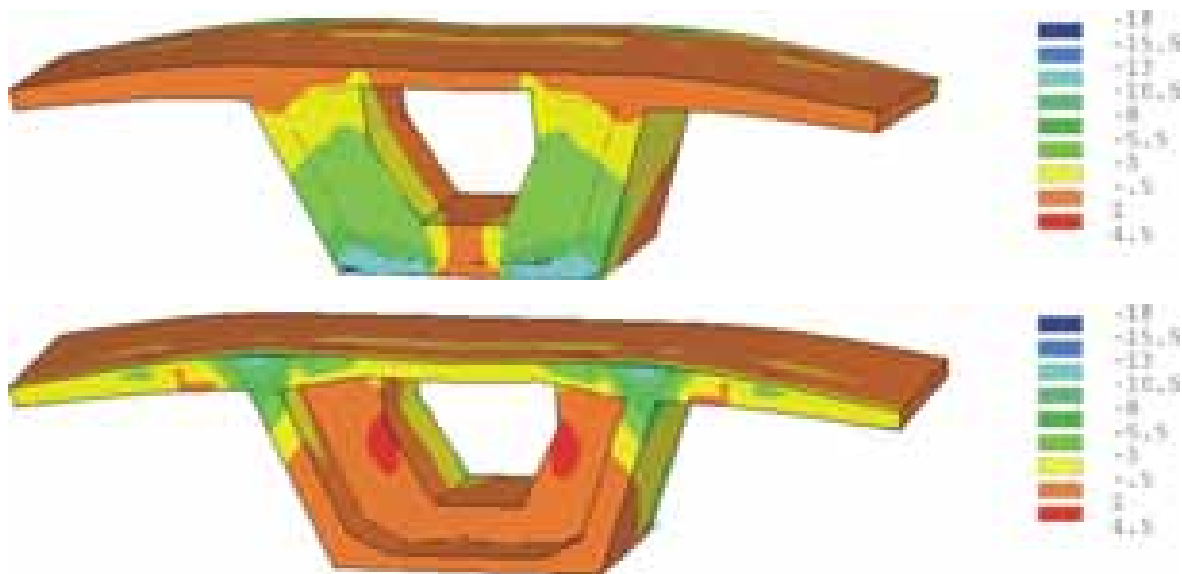


Figure 4.17 Vertical stress ω_z for front and opposite face of pier segment in permanent loading

The principal stress diagram (Fig. 4.18) shows that load flows from the two flanges to the webs. From webs it follows the same path. Only a small part of it flows into the diaphragm. The load from webs and diaphragm flows to two supports.

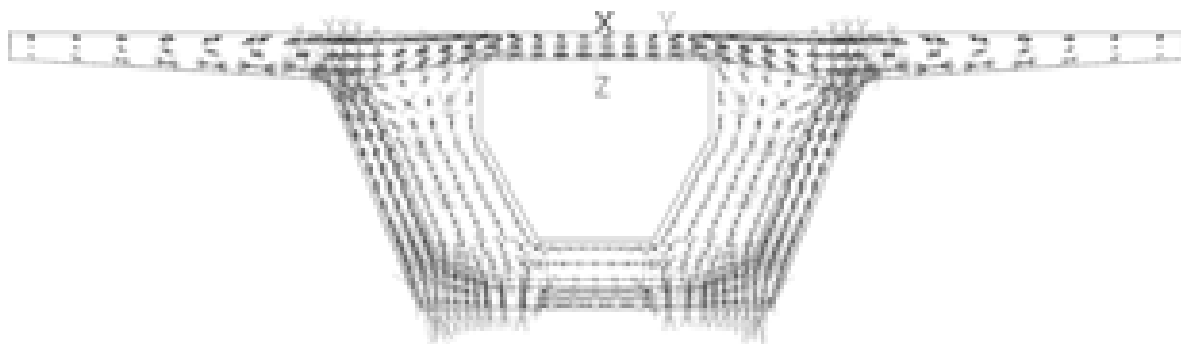


Figure 4.18 Principal stresses for open diaphragm in permanent loading

Vertical stress ω_z on the first joint (Fig. 4.19):

The stress distribution is symmetric due to symmetric load arrangement. The top slab shows non-uniform compressive stress distribution. The compressive stress on flanges increases linearly from two extremes to the junction between flanges and webs. It also decreases linearly from this intersection point to some distance to the interior part of top slab. It shows uniform stress distribution around the

central part of the top slab. The maximum compressive stresses are at the intersection points.

The compressive stress distribution on the web is also non-uniform. The stress value is high near the junction of flanges and webs and then it decreases somehow linearly from this area to support regions. On the bottom slab very minor irregular tension is observed.

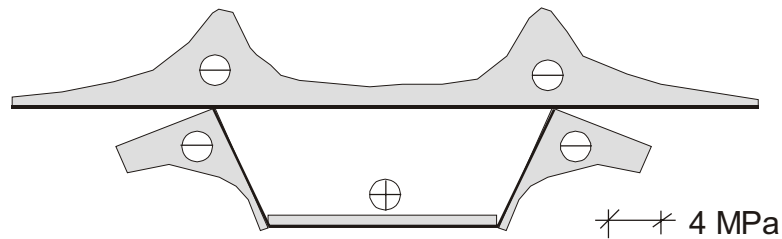


Figure 4.19 Vertical stress ω_z on the first joint for permanent loading

Longitudinal stress ω_x on the first joint (Fig. 4.20):

Compressive stress distribution is symmetric due to symmetric load arrangement. Compressive stress increases from tip of the flange to the area around the junction between web and top slab. Both the webs and the bottom slab are in full compression.

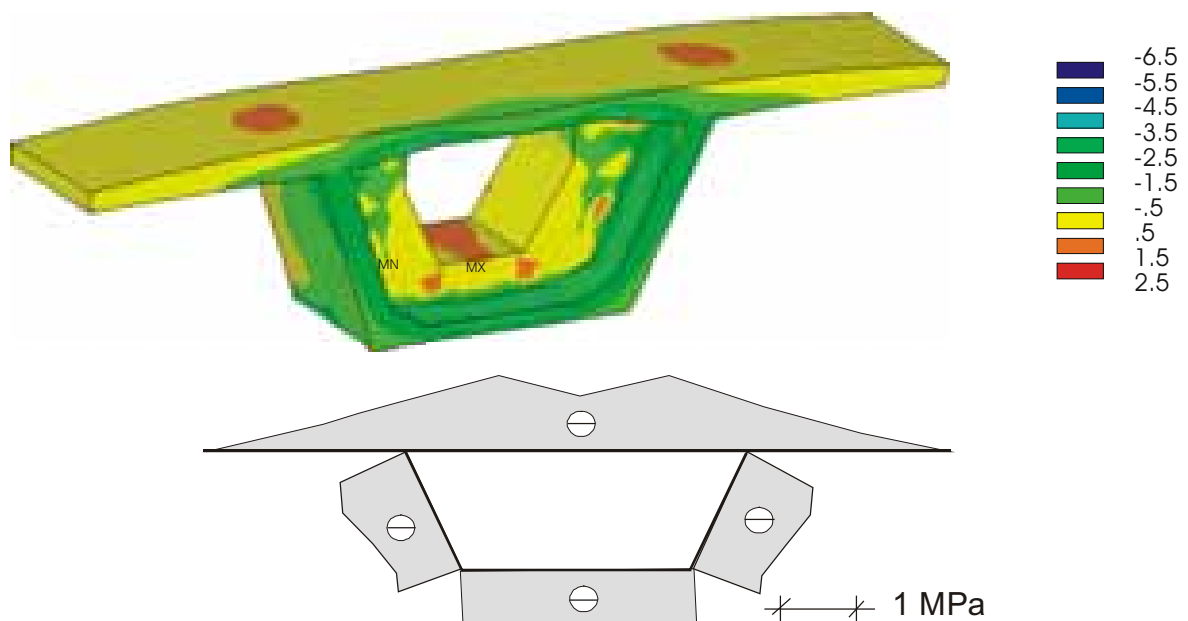


Figure 4.20 Longitudinal stress ω_x on the first joint for permanent loading

4.4.2 Load case for maximum torsion

4.4.2.1 Pier segment without manhole

For vertical stress ω_z (Fig. 4.21):

For this load case, the front face of the pier segment does not show significant difference with that for permanent loading. Similarly, the face is more or less in compression except for intersection between flange and web. Also the bottom slab near the support region shows slight tension. The compressive stress is more prominent in the support region. This shows that the stress increases from top to bottom. The web in side view is also in compression but compression is more prominent on the top.

The first joint is in compression. Due to load arrangement for maximum torsion, the compressive stress at the intersection between flange and web is more prominent on one part. The compressive stress in the top slab is non-uniform. It is observed that compressive stress on the web decreases with depth. Due to the diverging tendon force, the opposite face of the diaphragm is in tension.

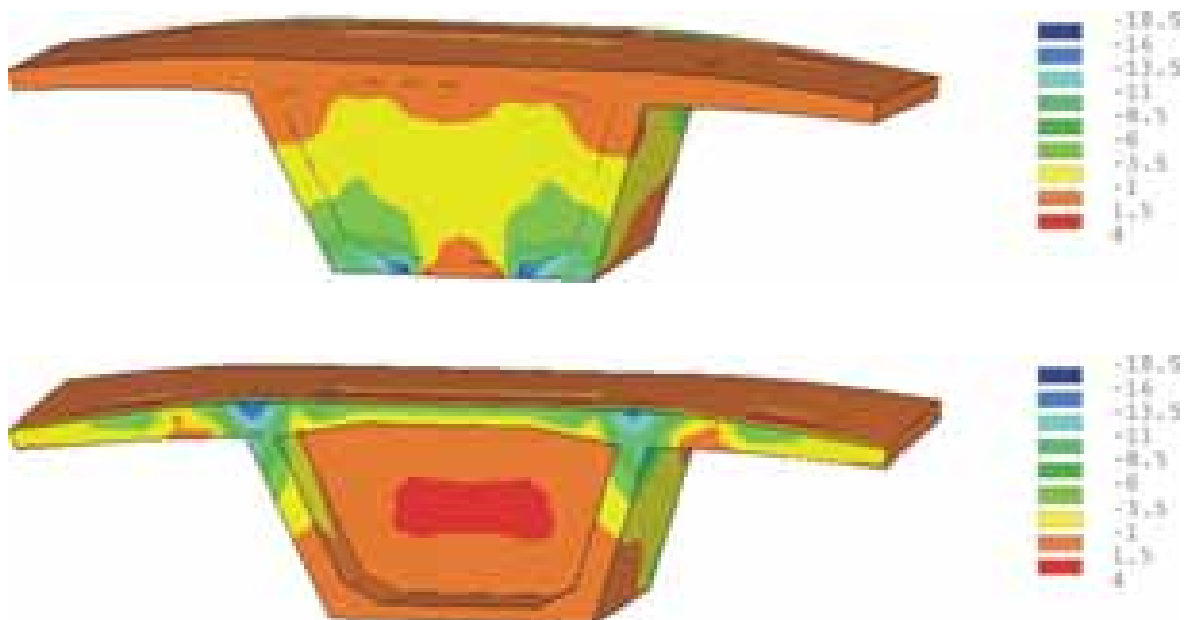


Figure 4.21 Vertical stress ω_z for front and opposite face of pier segment for max. torsion

The principal stress diagram for torsion in Fig. 4.22 shows that the load follows the path from flanges to webs. In the web, the majority of the load flows to the support while small quantity of it flows to the diaphragm.

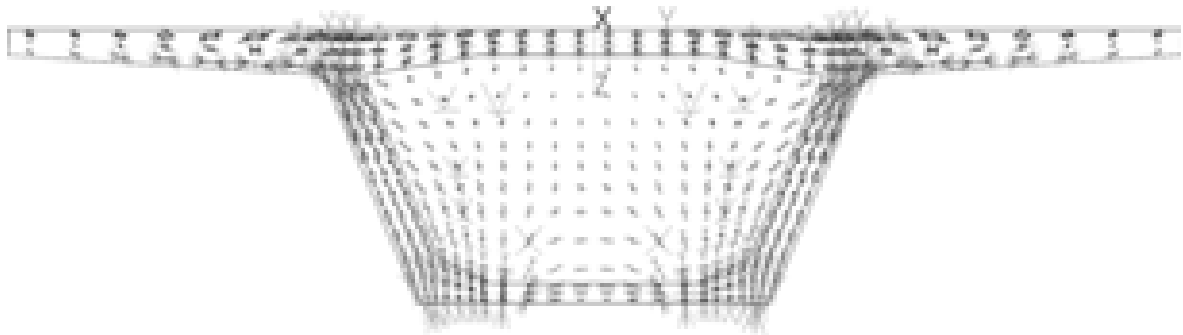


Figure 4.22 Principal stresses of closed diaphragm for max. torsion

Vertical stress ω_z on the first joint (Fig. 4.23):

Basically the stress distribution ω_z is similar to vertical stress ω_z on the first joint for permanent loading. In contrast to the previous one, on the right intersection point between the top slab and the web, the value of stress distribution is a bit higher than the left one due to unsymmetrical load arrangement for maximum torsion. There is also minor difference in stress distribution on bottom slab. The distribution on the webs is more or less similar.

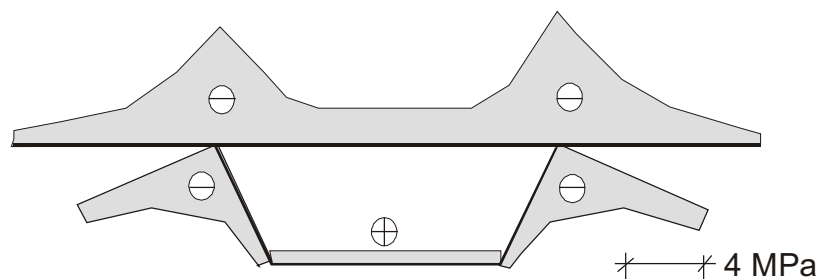


Figure 4.23 Vertical stress ω_z on the first joint for max. torsion

Longitudinal stress ω_x on the first joint (Fig. 4.24):

Due to load arrangement for maximum torsion, tensile stresses are seen only on the tip of right flange. The compressive stress increases from tip of flanges to the mid span of top slab, where it reaches its maximum value. The webs and the bottom slab are in full compression.

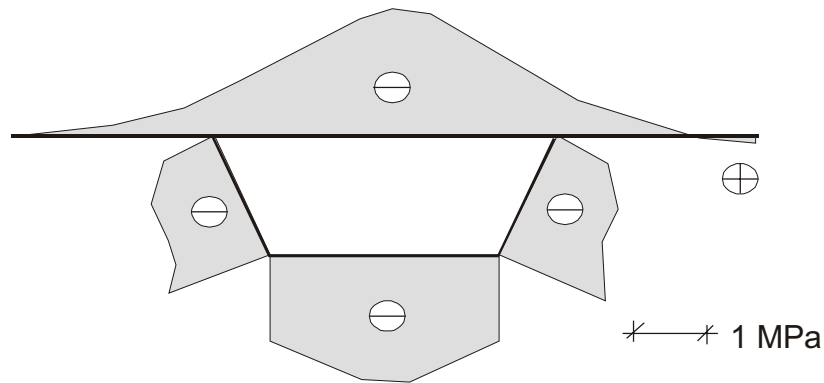


Figure 4.24 Longitudinal stress ω_x on the first joint for max. torsion

4.4.2.2 Pier segment with manhole

Vertical stress ω_z (Fig. 4.25).

The front face of the pier segment is in compression. The compression is small on the top slab but the intensity increases with depth. The compressive stress distribution is uniform on the top slab and the region between the supports. The intensity of compressive stress is varying within the height of diaphragm. The web is mainly compressed in longitudinal direction (see side view).

The central parts of diaphragm on the opposite face of the pier segment show tension. The tensile stress distributions at the centre are not uniform due to max torsion load arrangement. The compressive stress distribution is more prominent at the intersection between flanges and webs. The intensity of compressive stress distribution on the webs decreases with the section depth.

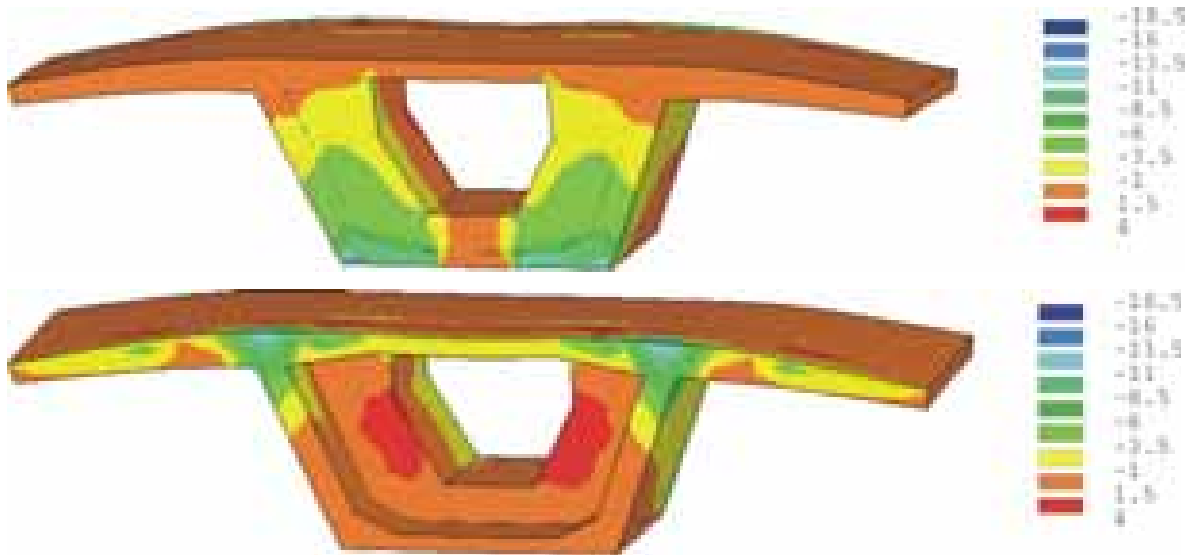


Figure 4.25 Vertical stress ω_z for front and opposite face of the pier segment for max. torsion

The principal stress diagram (Fig. 4.26) shows that the load flows from flange into webs. Also the loads from top slab along its length flows into the webs and then to the supports.

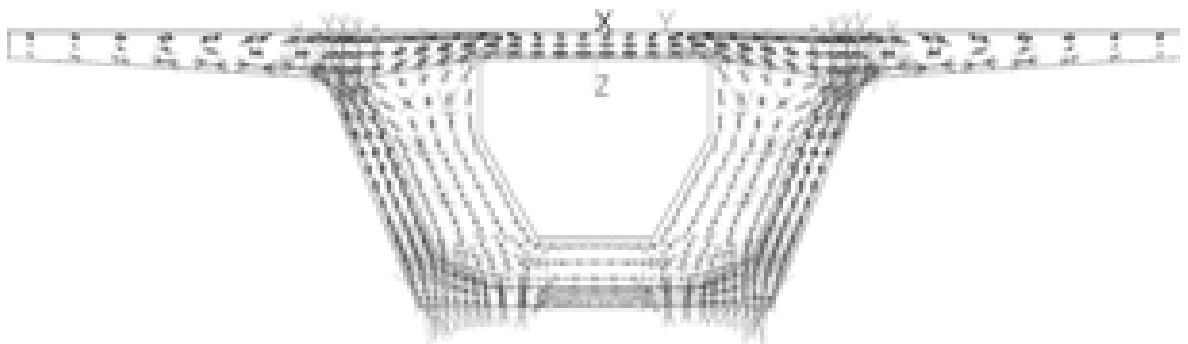


Figure 4.26 Principal stresses of open end diaphragm for max. torsion

Vertical stress ω_z on the first joint (Fig. 4.27):

Basically the stress distribution is similar to that of vertical stress ω_z on the first joint for permanent loading but the value of the stresses is smaller. In contrast to the results for permanent loading, the lower portion of the web does not have any compression. The maximum value of the compressive stresses is located in the intersection point between web and top slab. The value of the right intersection

point is slightly higher than the left one due to load arrangement for maximum torsion. The bottom slab shows minor tensile stresses.

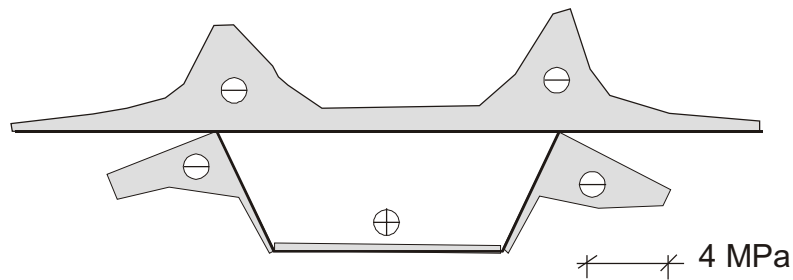


Figure 4.27 Vertical stress ω_z on the first joint for max. torsion

Longitudinal stress ω_x on the first joint (Fig. 4.28):

As in the case for closed diaphragm, the top slab is in compression except for the tip of the right flange, which is in tension. The intensity of compressive stress decreases from top of the web to bottom. The bottom slab is in compression and the compressive stress is higher at the centre than at the webs.

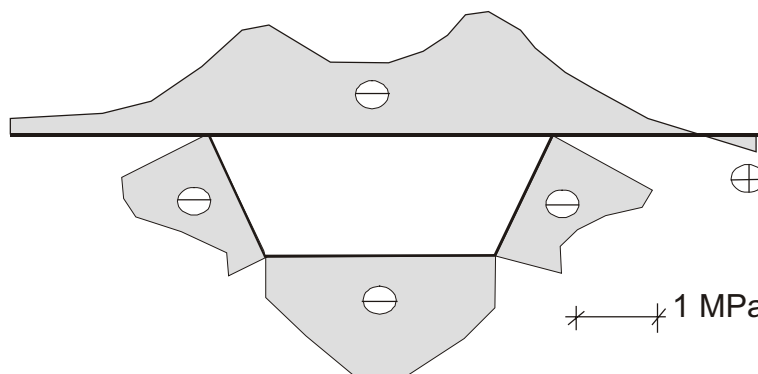


Figure 4.28 Longitudinal stress ω_x on the first joint for max. torsion

4.4.3 Load case for max. shear

4.4.3.1 Pier segment without manhole

Vertical stress ω_z (Fig. 4.29):

The compressive stress distribution on the front face of the pier segment is more or less similar to that for permanent loading and torsion. Here one can observe

tensile stresses at the junction between web and flange. Also minor tension can be seen at the bottom slab. The high compressive stresses on the first joint are caused by minor tensile stresses in the top slab near the joint. The other part of the front face of the segment is in compression. Compressive stress distribution is more dominant around the support region and its intensity increases with section depth.

On the opposite face of the segment, the majority of the diaphragm is in tension except on an upper part near the top slab. This tension is due to divergence of tendon forces. The compressive stress at the intersection between the webs and the flanges are more prominent. However, one of the intersections is more compressed than the other due to load arrangement for maximum shear. The intensity of compressive stress on the webs decreases from top to bottom. Compressive stress distribution in the top slab is non-uniform.

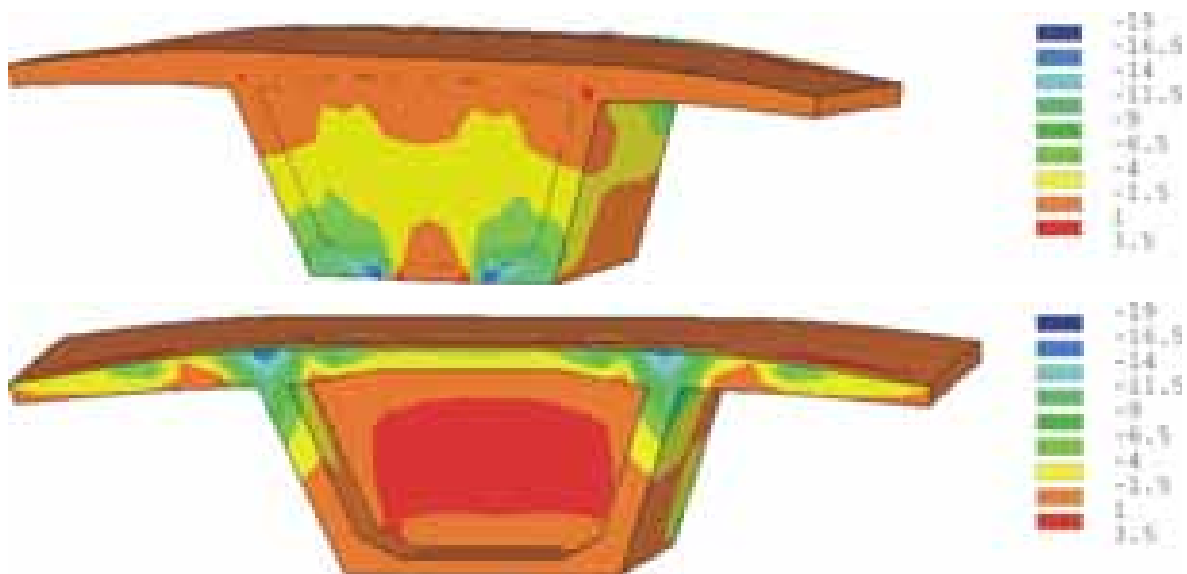


Figure 4.29 Vertical stress ω_z for front and opposite face of pier segment for max. shear

The principal stress diagram (Fig. 4. 30) also shows the load flow from two flanges to the web and from the web to the support. The stress distribution along the top and bottom slab is somehow parallel to the members (torsion). The stress on the diaphragm is scarcely distributed as compared to other parts.

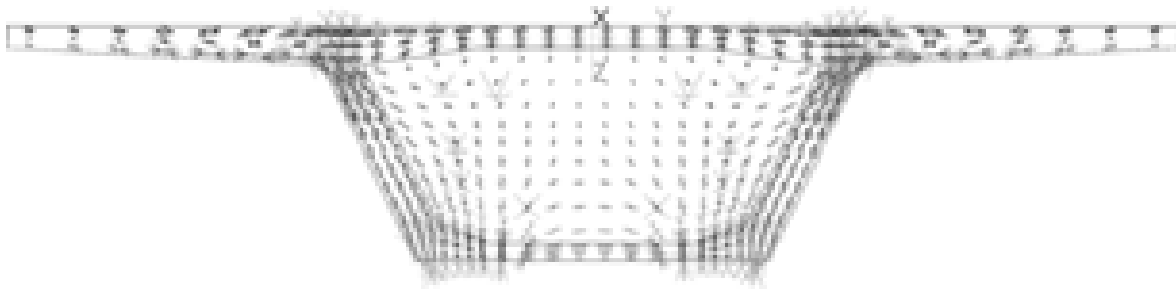


Figure 4.30 Principal stresses for closed diaphragm for max. shear

Vertical stress ω_z on the first joint (Fig.4.31):

The stress distribution is similar to that of vertical stress ω_z for permanent loading. Actually, the compressive stress on the right intersection between the webs and the top slab is slightly higher than the left one due to shear load arrangement. The compressive stress on the upper parts of the webs is higher than the lower part. There are minor tensile stresses in the bottom slab.

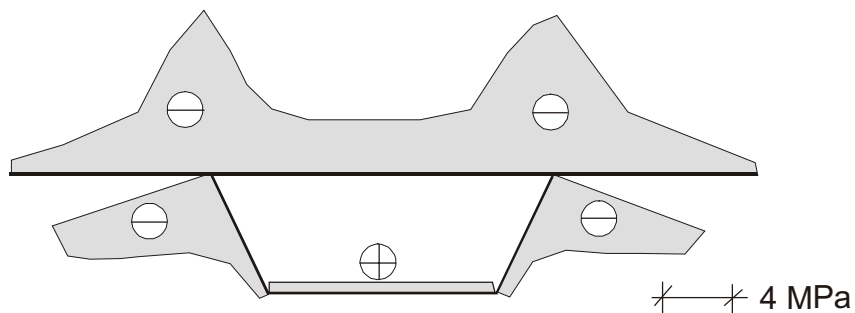


Figure 4.31 Vertical stress ω_z on the first joint for max. shear

Longitudinal stress ω_x on the first joint (Fig. 4.32):

The top slab is in compression except for the tip of flanges that are in minor tension. The maximum compressive stresses are in the central part of top slab. Both webs and bottom slab are in full compression.

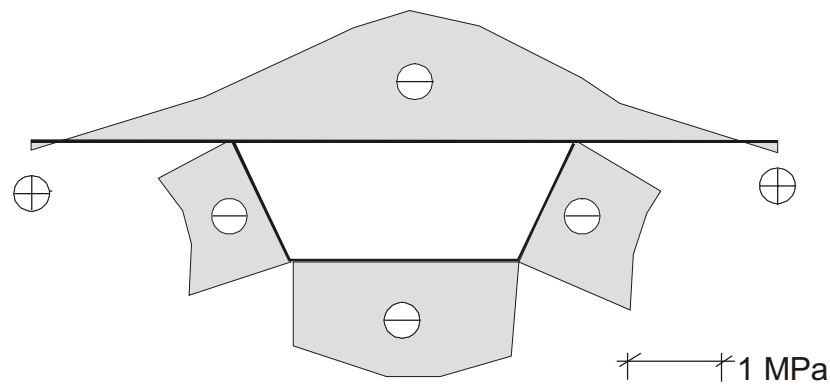


Figure 4.32 Stress ω_x on the first joint for max. shear

4.4.3.2 Pier segment with manhole

For vertical stress ω_z (Fig. 4.33):

The front face of the segment is in compression. The top slab and the area between the two supports are in uniform compression. The compressive stress is more dominant in the area above the supports.

The opposite face the diaphragm is in tension except near the top slab and at the lower edge of the manhole. Similar to the other types of pier segments, the intersection between the webs and flanges are highly compressed. Compression is higher on one intersection point than the other due to load arrangement for max shear. The stress distribution on top slab is non-uniform (Fig. 4.35). But the intensity of compressive stress decreases with depth.

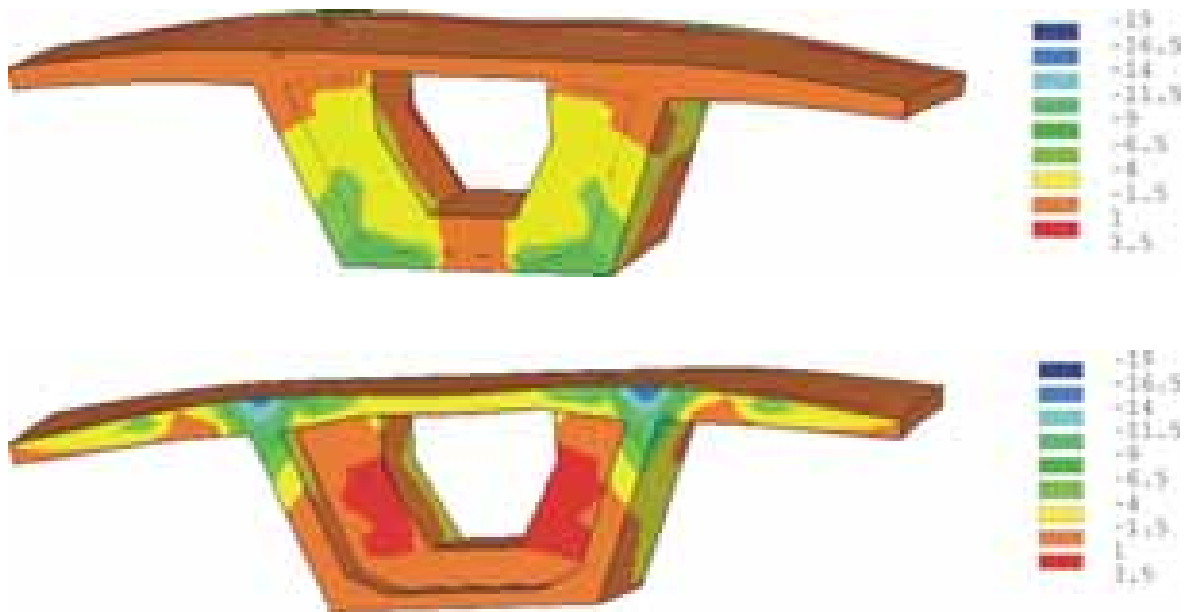


Figure 4.33 Vertical stress ω_z for front and opposite face of pier segment for max. shear

Principal stress diagram in Fig. 4.34 shows that the load path follows from flange to webs and from webs to support. The load path is parallel to the member both at the top and bottom slabs. The load flows from top of the diaphragm to bottom.

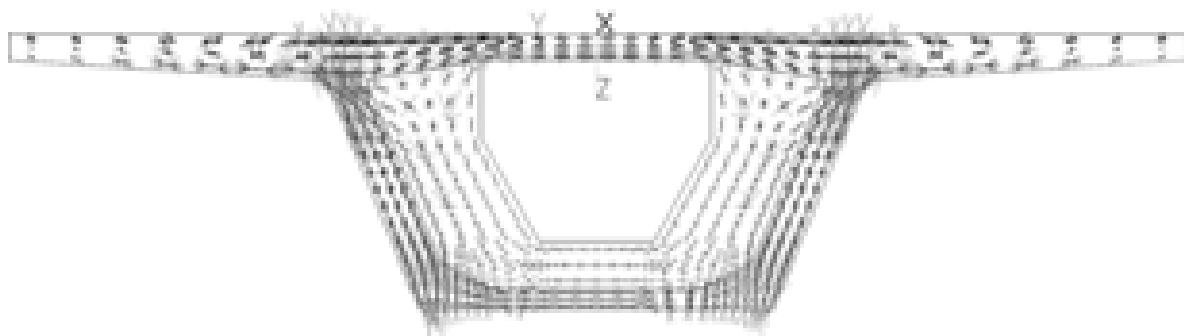


Figure 4.34 Principal stresses for open end diaphragm for max. shear

Vertical stress ω_z on the first joint (Fig. 4.35):

The stress distribution is similar to the vertical stress ω_z of permanent loading. The maximum compressive stress is observed at the intersection point between the webs and the top slab, but the right one is slightly higher than the left due to load arrangement for max. shear. The compressive stress on the web decreases linearly from top to bottom. Mild tensile stresses are observed at the bottom slab.

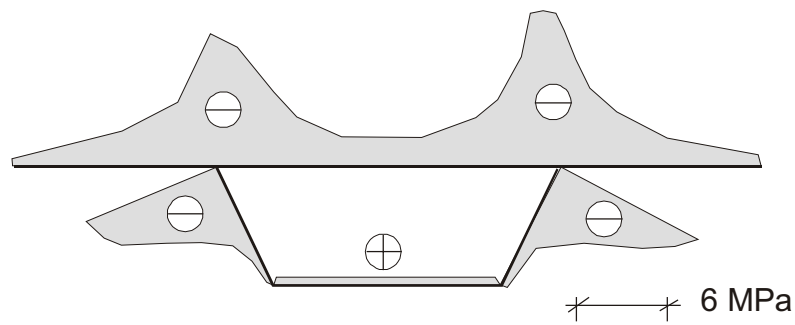


Figure 4.35 Vertical stress ω_z on the first joint for max. shear

Longitudinal stress ω_x on the first joint (Fig. 4.36):

The top slab is in compression except on the tip of both flanges. The maximum compressive stresses are near the intersection between webs and top slab. Both webs and bottom slab are in compression.

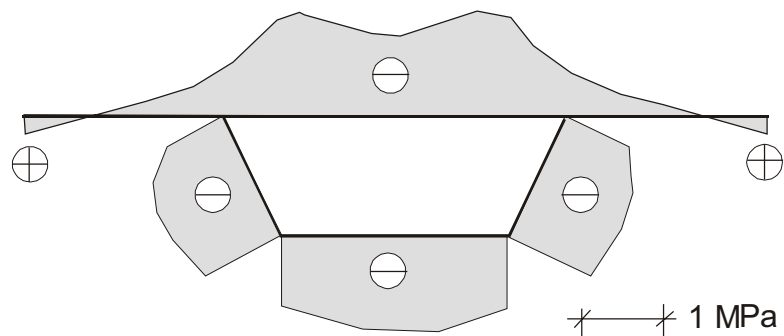


Figure 4.36 Longitudinal stress ω_x on the first joint for max. shear

4.4.4 Summary

For vertical stress ω_z :

The front face of the pier segment with closed diaphragm has a higher compression in the support area than the open diaphragm for all load cases. In the first joint, junctions of webs and top slab show more compression for a closed diaphragm than for an open one. At the opposite face however, the edges of the diaphragm manhole have higher tension than closed diaphragm.

In contrast to load case for permanent loading, the tensile stress on the opposite face of pier segments with closed diaphragm for both torsion and shear loadings shows significant tension.

The pier segment in the segmental bridge has dimension of height $h = 2.4$ m and length $l = 1.5$ m. The FE-results clearly demonstrate that the full segment may be considered as a D-region. It is reasonably to conclude that the stress and strain distributions in pier segment (D- region) are non-linear from the stress distribution ω_z and ω_x for different types of loadings discussed above.

For longitudinal stress ω_x on the first joint:

For permanent load case, pier segment without manhole shows tension on the tips of top slab, but the segment with manhole is fully compressed. For shear and torsion loading it shows tension on the tips of top slab.

The assumption, in the 2-D analysis of diaphragm shown in Figs. 3.10 through 3.12 that the major portion of the load on the pier segment comes from the top to the bottom, has been verified in this chapter. From finite element results and principal stresses one can observe that the prominent stress concentration is at the junction between top slab and webs, which is not inclined geometrically. So the application of load in vertical direction on top of the webs for 2-D analysis and strut-and tie models is acceptable. But when this load reaches the inclined portion of the web it follows the geometry of the web and consequently it acts as an inclined load. Also to attain the maximum tension on top slab, it would be advisable to apply the load on the top of the webs in a vertical direction.

5 Transfer of prestressing force from diaphragm to webs and slabs

The main objective of this research topic is to investigate the transfer of prestressing force (flow of forces) from diaphragm to the webs and the slabs of a hollow box girder bridge and to develop adequate strut-and-tie models for design. The available design models, e.g. the tripod model described in section 2.7.1 are based on engineering simplifications and had not been verified so far. Furthermore it had not been described by Wollman [4] how to estimate the forces for this statically indeterminate strut-and-tie model.

In the following, nine different points were selected on the front face of diaphragm, where a horizontal (prestressing) force is applied. These points in turn are arranged into three rows and three columns as shown in Fig. 5.1. For simplicity only half of the loading points are shown, but on the real structure, the prestressing forces are arranged symmetrically on the face of the diaphragm.

The analysis has been conducted for a pier segment with open and closed diaphragm (constant width of 1.50 m, see Fig. 1.8, 1.9). Pier segments with various diaphragm thickness (0.5 m, 0.75 m and 1.0 m) were analysed. From these analytical results the author has observed that the thickness does not have so much influence on the force transfer. The structure has been restrained on both vertical (y) and longitudinal (z) direction in the first joint to resist the curved tendon forces. There are no significant tensile stresses at the supports for the chosen location of forces. So this simplification is acceptable.

Diagrams showing the force distribution for the rows and columns are given in Figs. 5.3 through 5.14. The measurement for the row (x-direction) starts at the inner side of the web where as for columns (y-direction) starts at the lower part of top slab on the centre of the segment (Fig. 5.1).

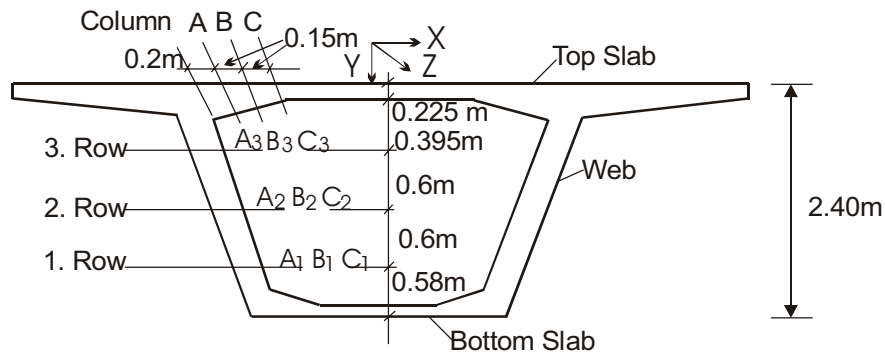


Figure 5.1 Position of load arrangement

Figure 5.2 shows the normal stresses in the first joint caused by a horizontal prestressing force at location A2 according to Fig. 5.1. A highly nonlinear distribution can be seen in the top slab whereas the web and the bottom slab shows a more or less linear distribution. Further shown in Fig. 5.2 is the Tripod model (Fig. 2.17), whereby the nodes A1 to A3 are located in the centre of the stress integral. It can clearly be seen, that Wollmann's [4] assumption that A2 and A3 are located in the middle of the effective width (Fig. 2.20) does not hold true.

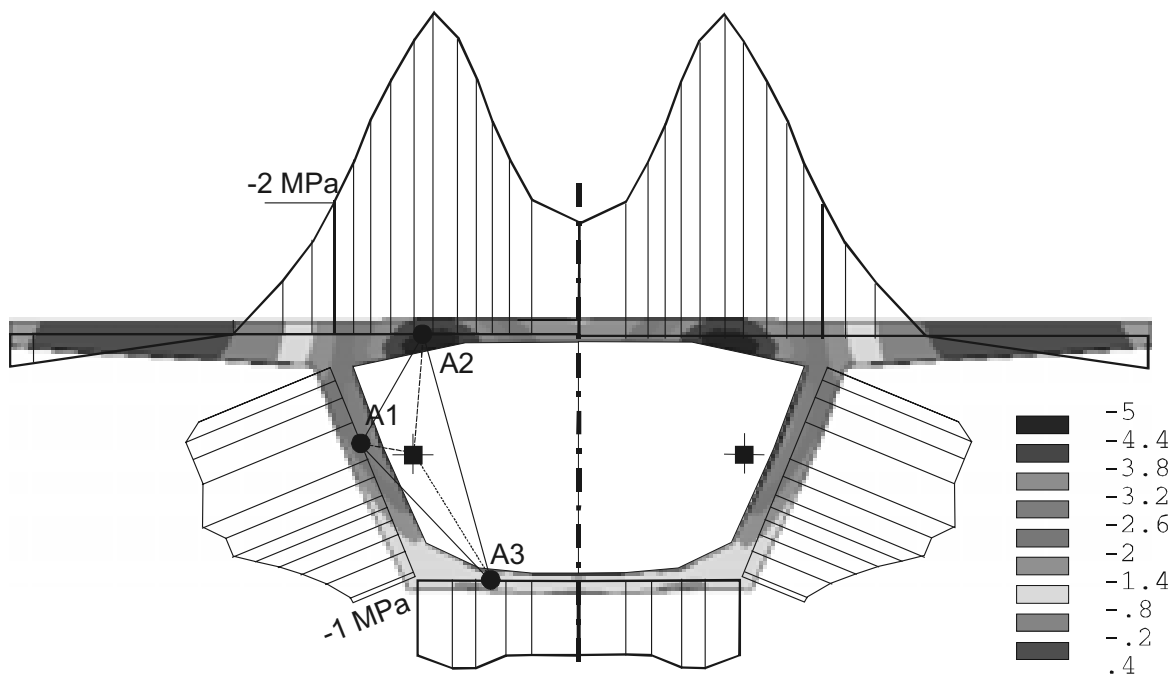


Figure 5.2 Normal stresses in the first joint

5.1 Force distribution due to load arrangement on the first row

Closed diaphragm (Fig. 5.3): The greatest part of the prestressing force is going to the bottom slab due to the small distance of the loading points to this structural element. A linear relation between the force distribution and the distance from the web is seen. The force in the web is obviously greater than in the top slab. But it decreases linearly when the point load moves away from the web. The force in the top slab increases slightly linearly. For a diaphragm with a manhole (Fig. 5.4) the force distribution is similar to the closed diaphragm except for differences in magnitude and linearity.

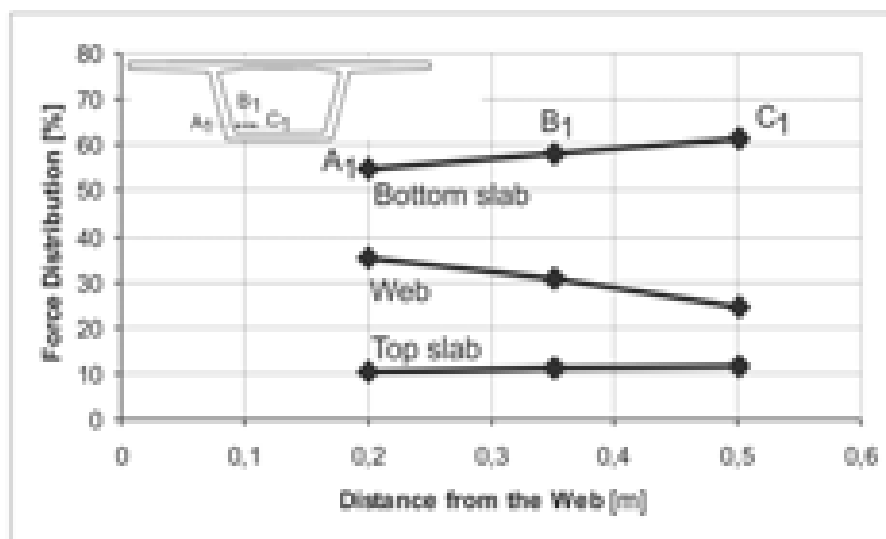


Figure 5.3 Force distribution due to load arrangement on first row for closed diaphragm

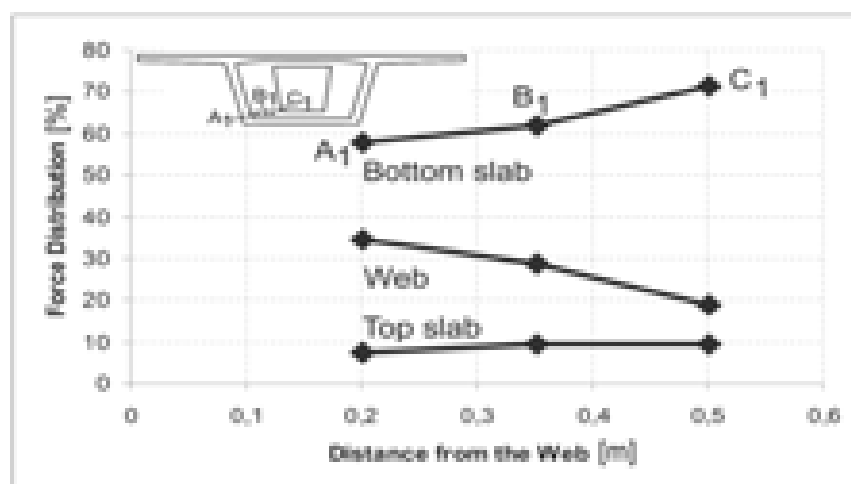


Figure 5.4 Force distribution due to load arrangement on first row for a diaphragm with manhole

5.2 Force distribution due to load arrangement on the second row

The force distribution due to a load arrangement on the second row for a closed diaphragm is shown in Fig. 5.5 and of a segment with a manhole in Fig. 5.6. Again a linear relation between the force distribution and the distance in the row is seen. The force in the bottom slab is higher than in the top slab. The force distribution for a diaphragm with a manhole is similar to that of the closed diaphragm. But at point C_2 the minimum value is observed on the top slab and not on the webs.

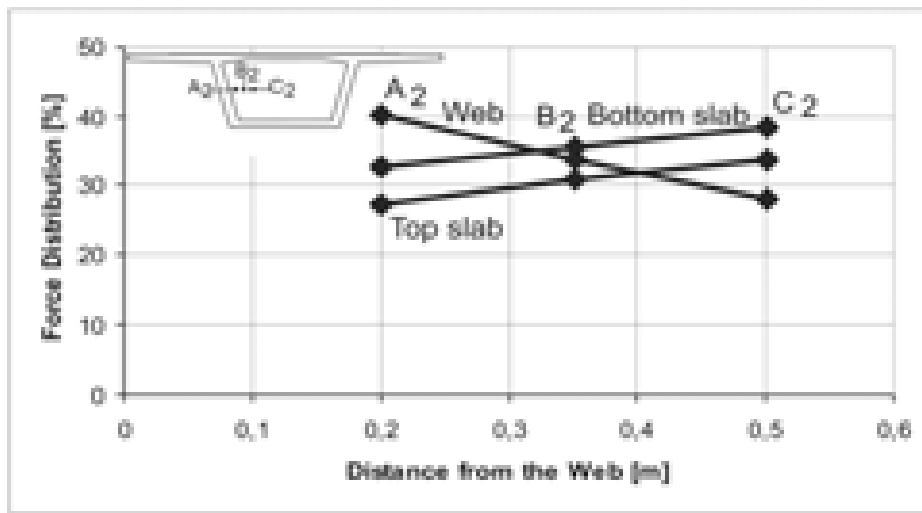


Figure 5.5 Force distribution due to load arrangement on second row for closed diaphragm

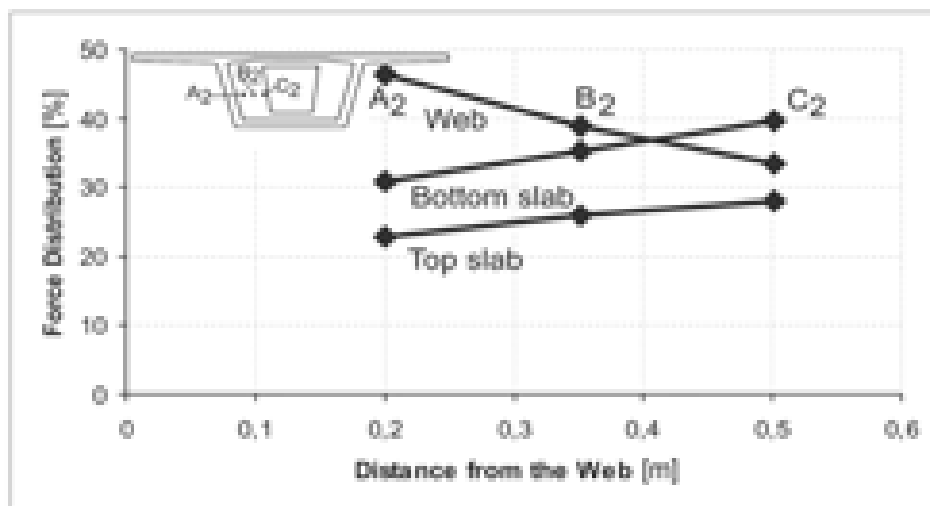


Figure 5.6 Force distribution due to load arrangement on second row for a diaphragm with manhole

5.3 Force distribution due to load arrangement on the third row

Closed diaphragm (Fig. 5.7): In contrast to the results of the first row the maximum force is in the top slab and the minimum value is in bottom slab. The force increases linearly both in bottom and top slabs and decreases linearly in the web as loading point moves away from web. For the diaphragm with a manhole (Fig. 5.8), the force distribution is similar to that of the closed diaphragm except for some irregularities in linearity.

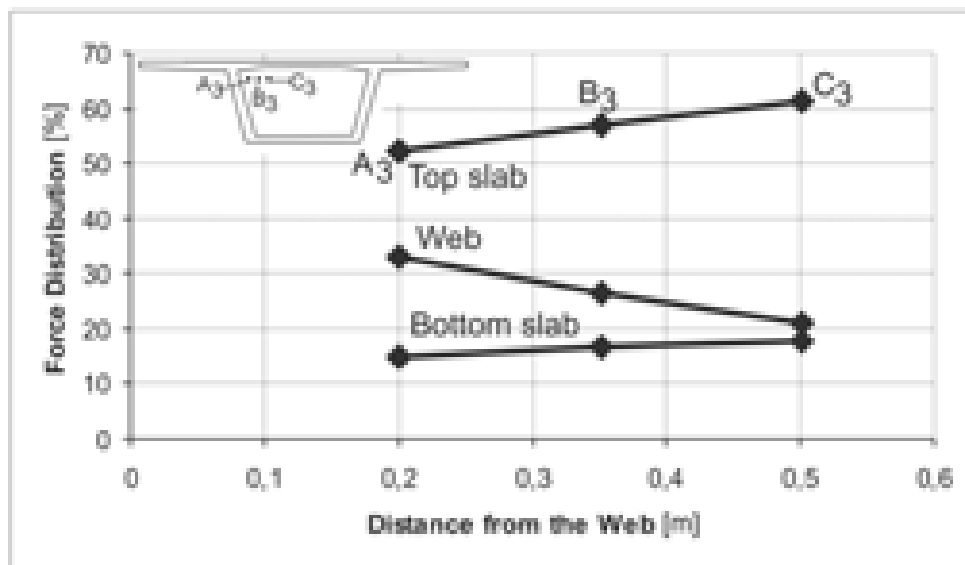


Figure 5.7 Force distribution due to load arrangement on third row for closed diaphragm

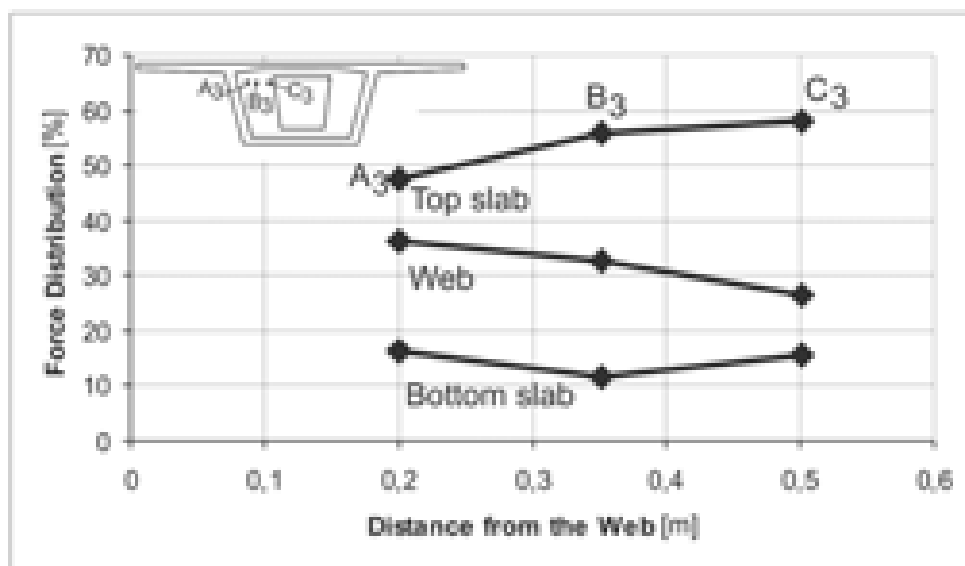


Figure 5.8 Force distribution due to load arrangement on third row for a diaphragm with a manhole

5.4 Force distribution due to load arrangement on the column A

Closed diaphragm (Fig. 5.9): The force in the top slab decreases linearly with depth whereas in the bottom slab it increases with depth. The force distribution in the web is nearly independent from the location of the loading point. No significant differences can be observed between a closed diaphragm and a diaphragm with a manhole (Fig. 5.10).

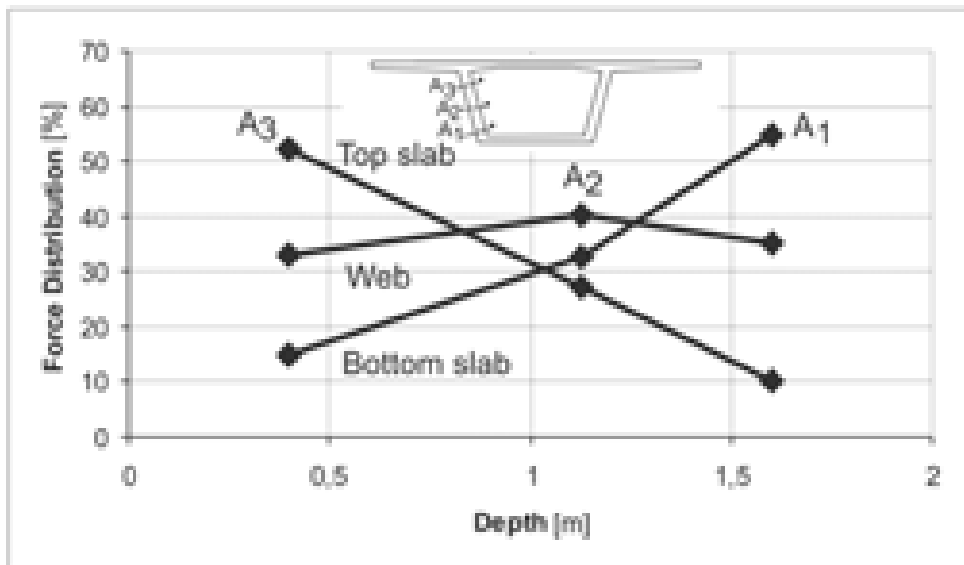


Figure 5.9 Force distribution due to load arrangement on column A for closed diaphragm

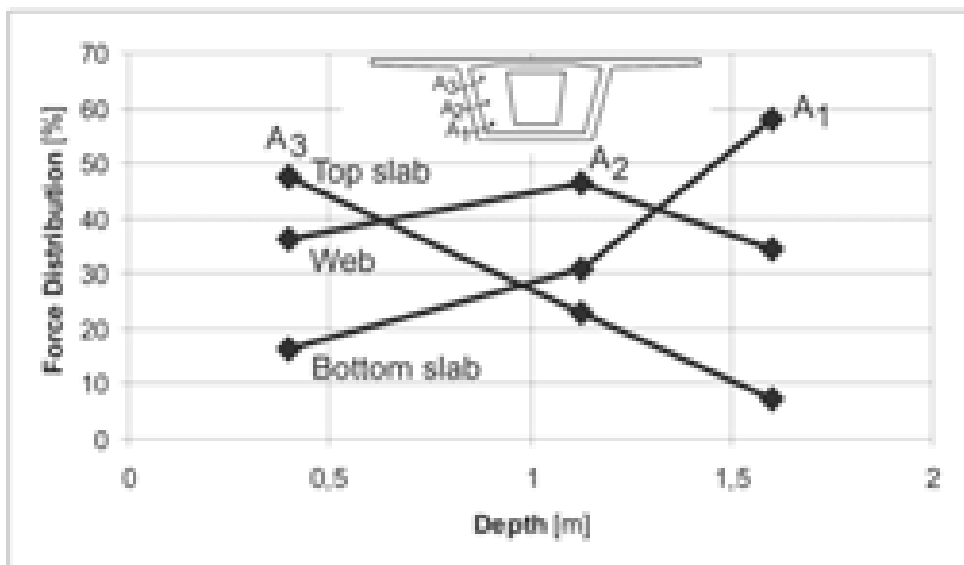


Figure 5.10 Force distribution due to load arrangement on column A for open diaphragm

5.5 Force distribution due to load arrangement on the column B

Closed diaphragm (Fig. 5.11): The force distribution is similar to column A in the top slab, bottom slab and web but varies in magnitude. The manhole (Fig. 5.12) does not change the distribution of forces significantly. Only small differences in magnitude can be observed.

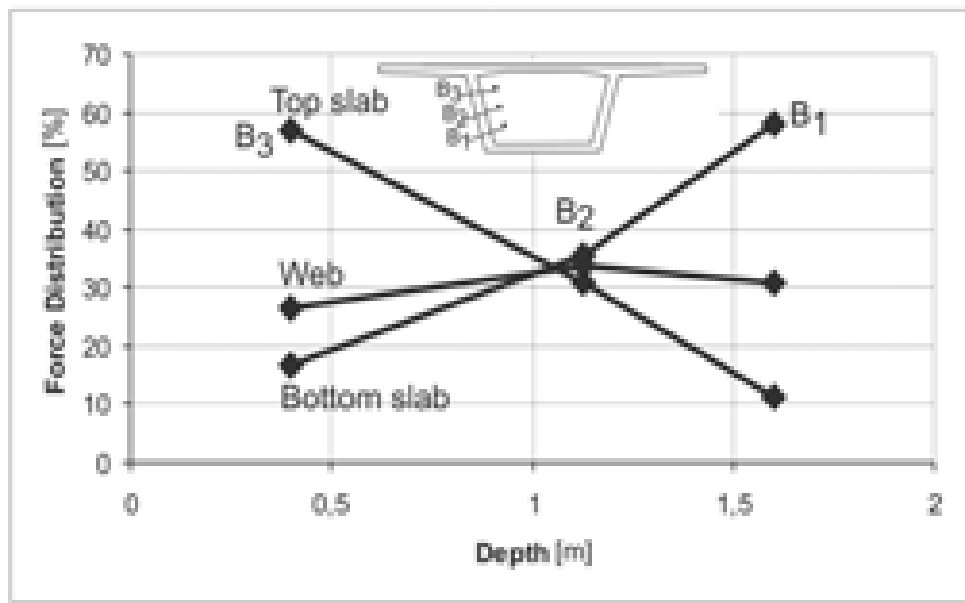


Figure 5.11 Force distribution due to load arrangement on column B for closed diaphragm

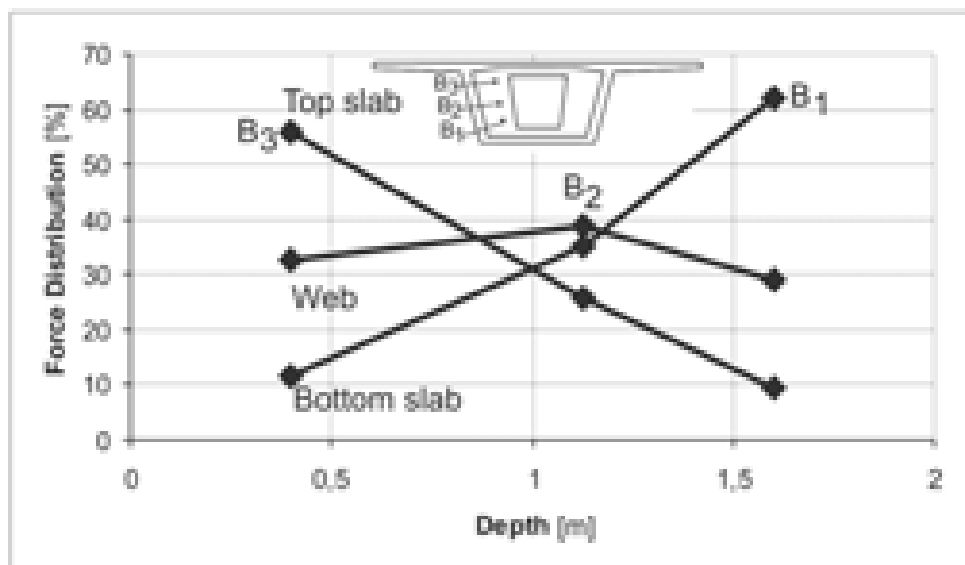


Figure 5.12 Force distribution due to load arrangement on column B for open diaphragm

5.6 Force distribution due to load arrangement on the column C

The force distribution of the closed diaphragm is similar to the columns A and B except for small differences in magnitude (Fig. 5.13). In the case of diaphragm with a manhole (Fig. 5.14), the force distribution is similar to that of closed diaphragm but differs in magnitude.

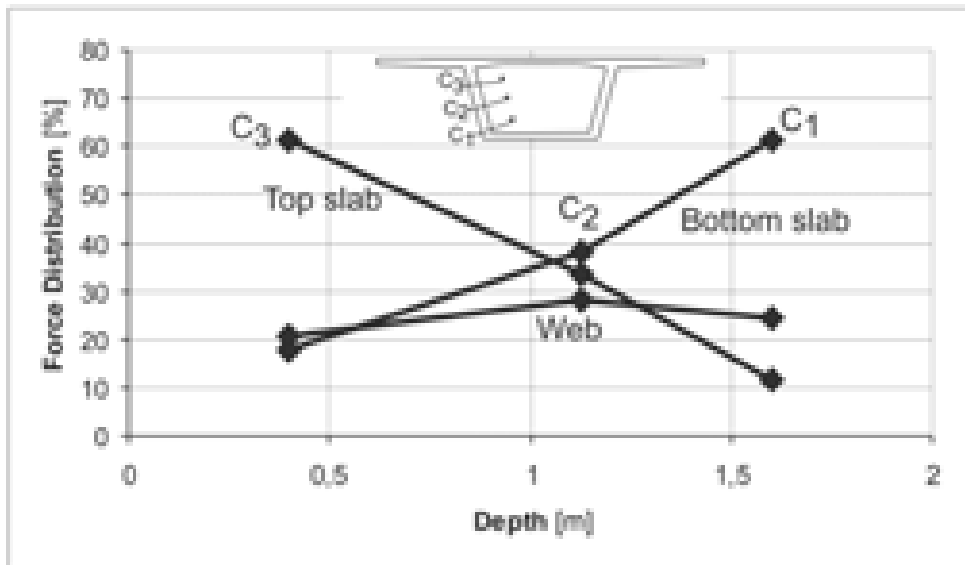


Figure 5.13 Force distribution due to load arrangement on column C for closed diaphragm

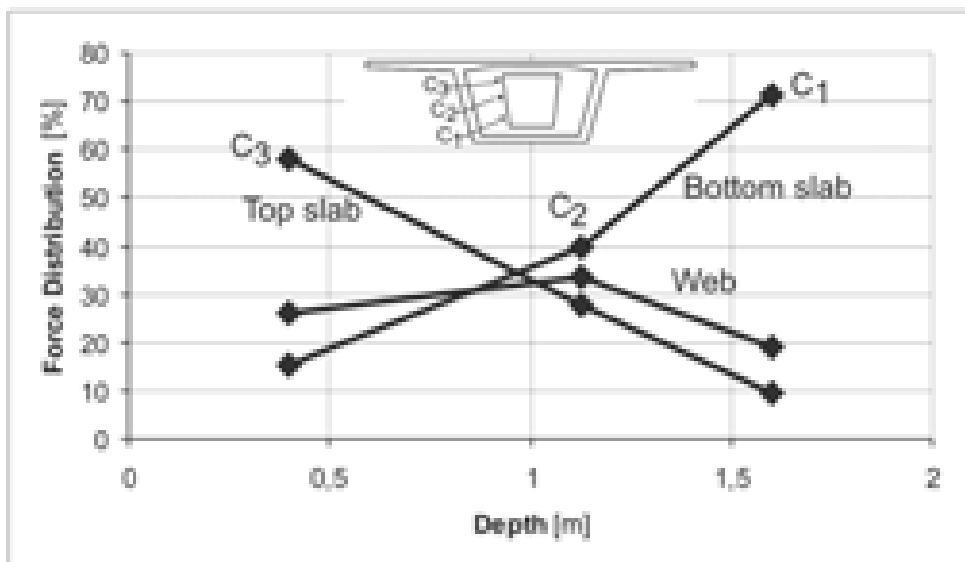


Figure 5.14 Force distribution due to load arrangement on column C for open diaphragm

6 Evaluation of strut-and-tie models for design of diaphragms

In this chapter adequate strut-and-tie models for practical design of diaphragms will be developed. The FE-results will be used to modify the models published by Schlaich et. al [7] (see chapter 2) for a shear wall with and without a manhole for different type of loadings. Furthermore the 3-D strut-and-tie model for force transfer from diaphragm to slabs and webs developed by Wollmann [4] will be evaluated.

6.1 Strut-and-tie models for loads from superstructure

6.1.1 Closed diaphragm – shear and torsion loading

In chapter 3.3.2 a 2-dimensional shear wall was used to carry the corresponding load from the bridge. The load was applied on top of the diagonal sides in the proportion that could call the corresponding maximum shear and torsion forces. As it is seen in the following figures, the strut-and-tie model developed by Schlaich et. al (Fig. 6.2) agrees very well with the results from finite element analysis shown in Figs 6.1 and 6.4.

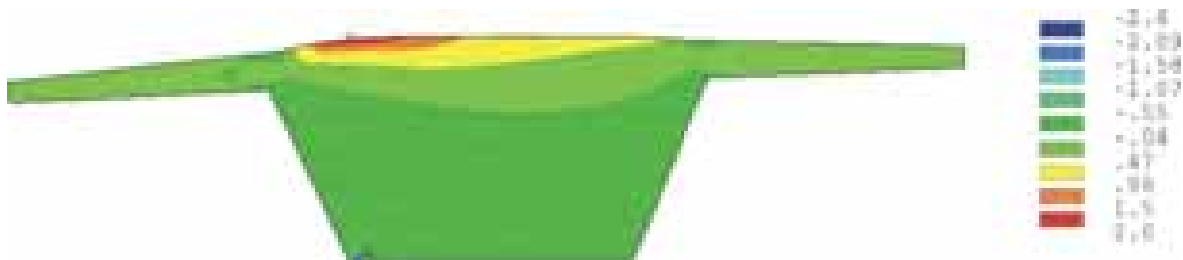


Figure 6.1 Horizontal elastic stress σ_x

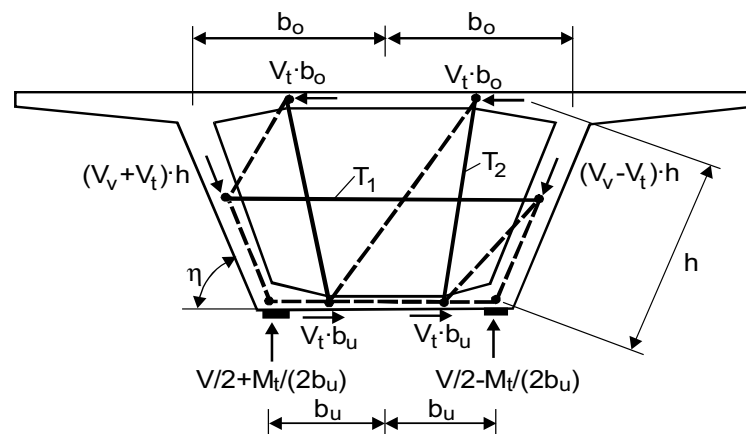


Figure 6.2 Diaphragm strut-and-tie model for shear and torsion moment [7]

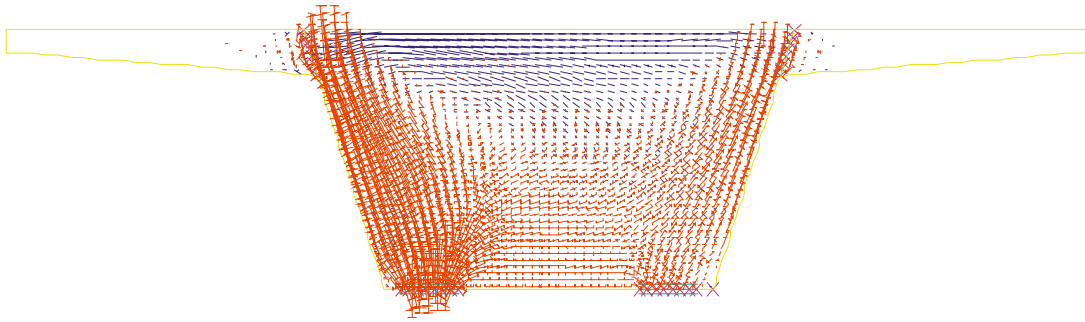


Figure 6.3 Principal stress diagram

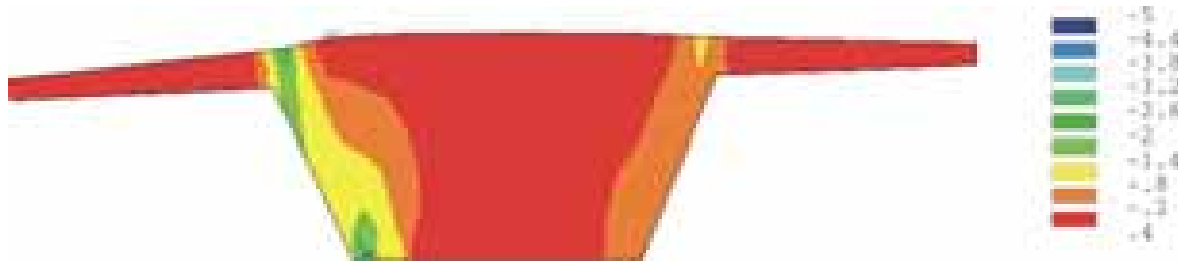


Figure 6.4 Vertical elastic stress ω_y

6.1.2 Pier Segment with two supports and manhole – permanent loading

Horizontal tensile stresses ω_x are seen in the upper part of diaphragm above the manhole (Fig. 6.5). This corresponds with tie force T_1 of the Schlaich's model in Fig. 6.8. In contrary to the tension tie T_2 in Schlaich's model, the lower part of diaphragm near the support region shows no tension.

Both webs show vertical compressive stresses ω_y (Fig. 6.7). Vertical compressive stresses in the lower part of the webs have greater width than at the supports. The tensile stresses extend from top of diaphragm down to the vertical edge of the opening due to uplifting action of external loads on the diaphragm. Based on the stress distributions in both directions a new strut-and-tie model is developed. The new model (Fig. 6.9) has tension tie T_1 in horizontal direction, T_2 in vertical direction on both sides of the manhole and T_3 in diagonal direction.

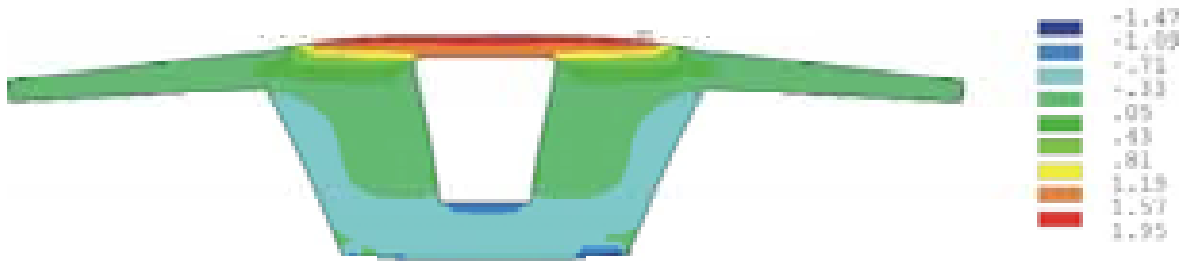


Figure 6.5 Horizontal elastic stress ω_x

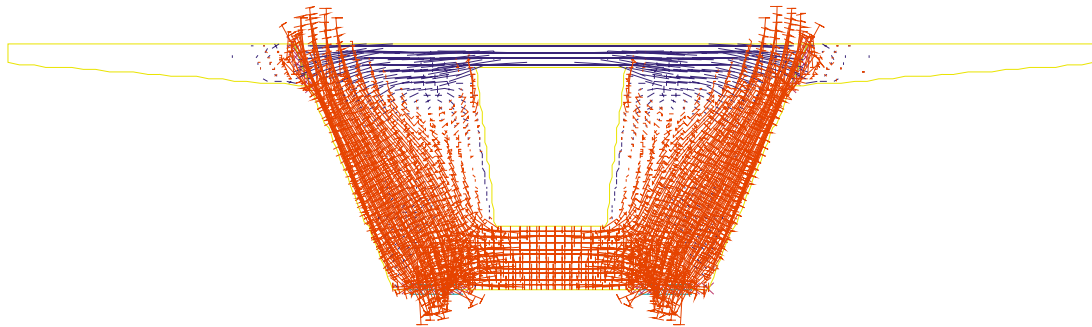


Figure 6.6 Principal stress diagram

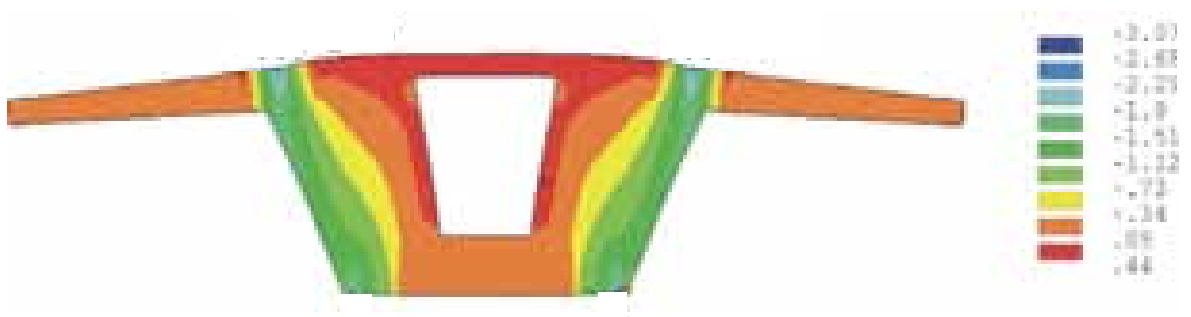


Figure 6.7 Vertical elastic stress ω_y

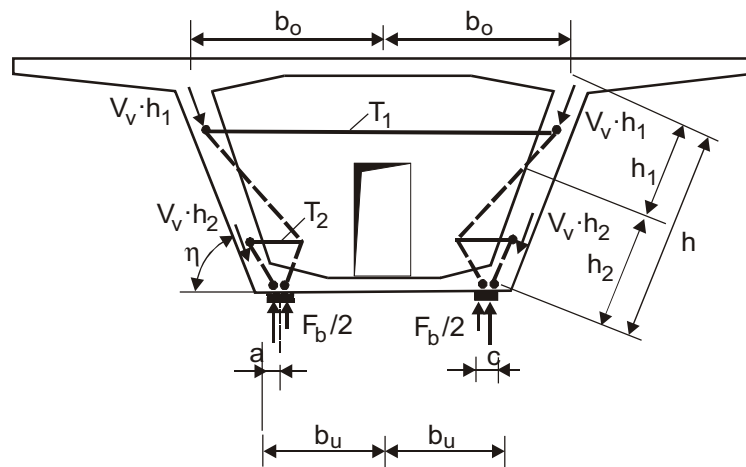


Figure 6.8 Strut-and-tie model for pure shear loading [7]

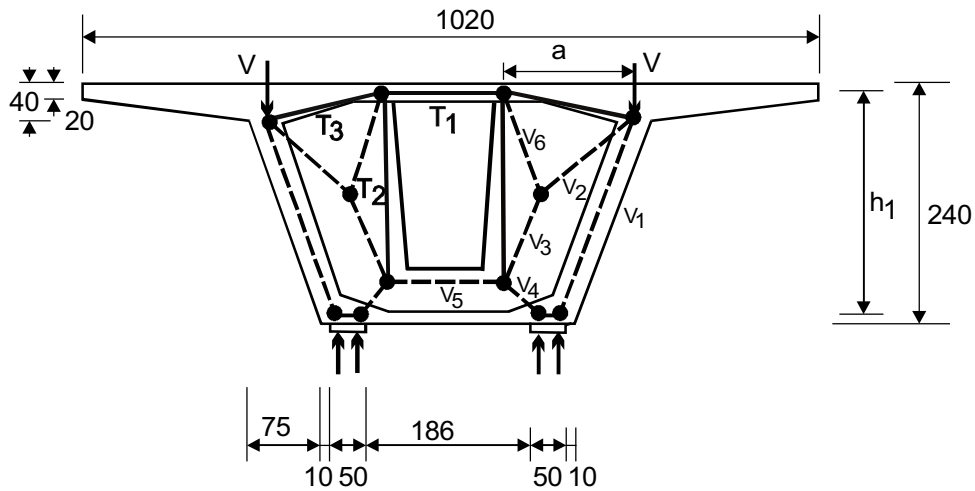


Figure 6.9 New strut-and-tie model for pure shear loading

An investigation has been conducted for shear wall that has dimension as shown in Fig. 6.9. The value of the average tensile stresses in the horizontal and vertical directions are calculated from the normal stress distributions ω_x and ω_y of the finite element analysis. The values of compressive forces V_1 to V_6 that flow through the diaphragm to the supports are determined from the load (V) based on the numerical analysis conducted for truss model is shown in appendix D. The values of tie forces T_1 , T_2 and T_3 of the finite element analysis, truss model and the developed formulae (eq. 6.1 through 6.3) agree very well (Tab. 6.1). However the value of T_2 of finite element analysis shows some discrepancy due to the difficulty to determine the real integration width of this force. For derivation of formulae please refer to appendix D and E.

Table 6.1 Tie forces from various models

	T_1	T_2	T_3
Truss model	366KN	118KN	433KN
Formulae	369KN	136KN	448KN
Finite E. Analysis	353KN	80KN	414KN

$$T_1 = 0.7 \left(\frac{V}{h_1} \right) a \quad \dots\dots\dots (6.1)$$

$$T_2 = \frac{V (2h_1 - 4a)}{12.5h_1} \quad \dots\dots\dots (6.2)$$

$$T_3 = 0.85 \left(\frac{V}{h_1} \right) \dots\dots\dots (6.3)$$

- V Half of total vertical force
 T_1, T_3 Tensile force on horizontal direction (mainly)
 T_2 Tensile force in vertical direction

6.1.3 Pier Segment with central support and closed diaphragm – permanent loading

The stress distribution ω_x (Fig. 6.10) shows tension in the upper part of the diaphragm that corresponds with tensile force T_2 of Schlaich's model (Fig. 6.13) [7]. The lower part of the diaphragm is in compression in horizontal direction. The stress distribution ω_y (Fig. 6.12) shows tensile stresses that extend from top to bottom slab. This does not agree with Schlaich's model where the lower part of the diaphragm is in full compression. The external load and support reaction cause compression in diagonal direction and tension at its perpendicular direction. A new strut-and-tie model (Fig. 6.15) is developed based on the FE-results and principal stress diaphragm (Fig. 6.11). Tension force T_3 is added for tensile stresses in the lower part of diaphragm. Another type of strut-and-tie model is given for diaphragm with indirect support in Fig. 6.14 [101]. Also this can be one of the possible options of strut-and-tie model for diaphragm with indirect support.



Figure 6.10 Horizontal stress ω_x

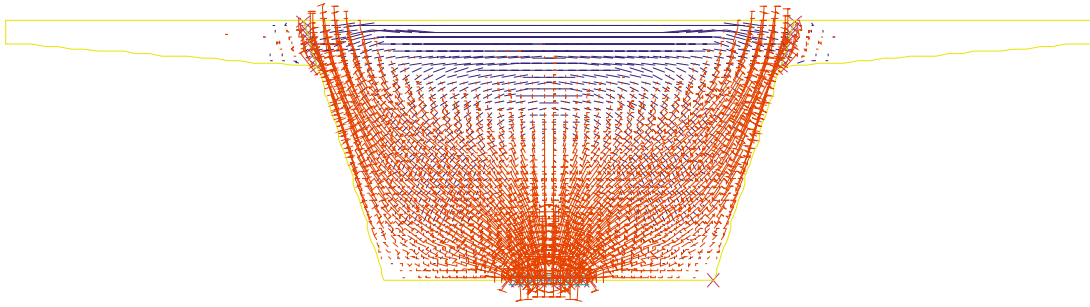


Figure 6.11 Principal stress diagram

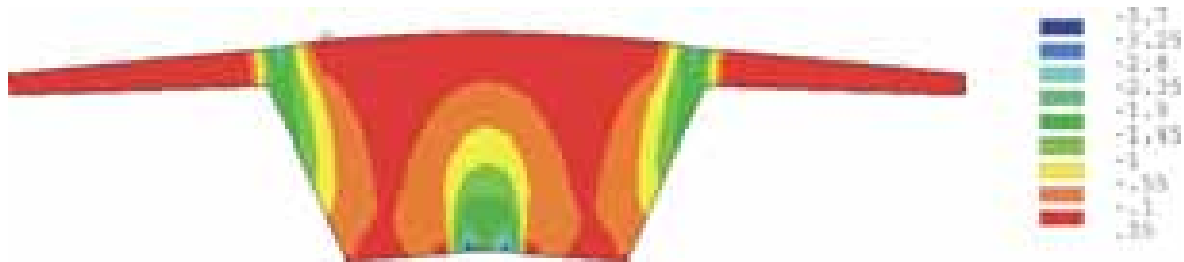


Figure 6.12 Vertical stress σ_y

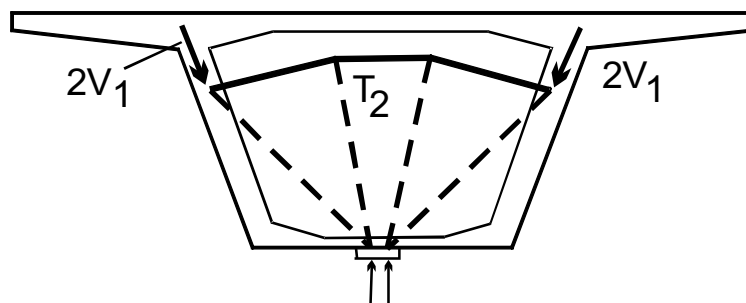


Figure 6.13 Schlaich's strut-and-tie model for diaphragm with indirect support [7]

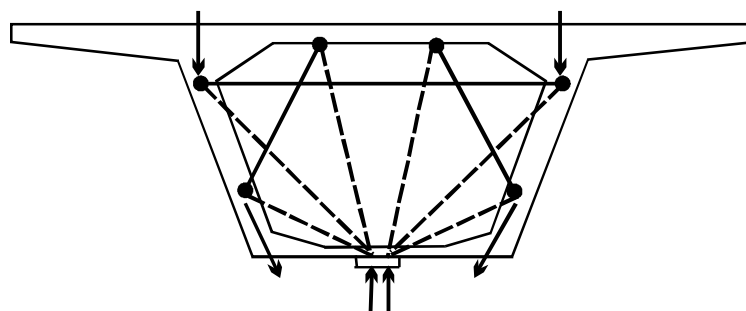


Figure 6.14 Strut-and-tie model for diaphragm with indirect supports. [101]

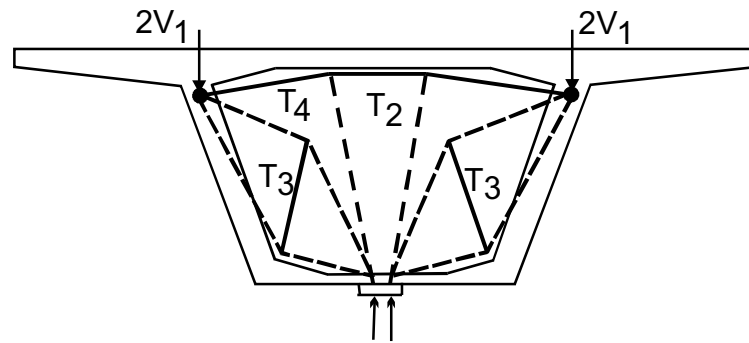


Figure 6.15 New strut-and-tie model for pure shear loading

From the geometry it is possible to calculate tensile forces T_2 , T_3 and T_4 in Fig. 6.15. The values of tensile forces calculated by methods of section and joint are given in appendix B.

6.2 Strut-and-tie model for prestressing force

Wollman [4] has developed three different strut-and-tie models (tripod model, corbel and frame action), which describe the flow of forces due to a prestressing force in a 3-dimensional end diaphragm (see section 2.7 and Fig. 6.17, 6.18). His investigation of force transfer from diaphragm to webs and slabs was based on simple beam theory (linear strain and stress distribution over the section depth at the joint). The location and magnitude of the resultant forces are obtained by integrating this stress distribution over respective areas, but the stress distribution on the D-region is complex in nature and cracks are sometimes observed in this area. So simple beam theory should not be applied here. Finite element calculations, for load on different locations were conducted (see chapter 5) to analyse the complex flow of forces in a diaphragm. To put these results into field of practice, the force arrangement in the column direction was selected. The summary of the numerical investigations, the average values of force transfer in percentage for previously defined heights for closed and open diaphragms are given below. The values for different heights may be calculated by interpolations. Please note that these factors are only applicable for the given geometry of the pier segment.

Table 6.2 Value of force transfer in percentage for open diaphragm (Fig. 5.12)

parts of pier segment	B1 [h = 1.82 m]	B2 [h = 1.22 m]	B3 [h = 0.62 m]
web	29 %	39 %	33 %
top slab	9 %	26 %	56 %
bottom slab	62 %	35 %	11 %

Table 6.3 Value of force transfer in percentage for closed diaphragm (Fig. 5.11)

parts of pier segment	B1 [h = 1.82 m]	B2 [h = 1.22 m]	B3 [h = 0.62 m]
web	31 %	33 %	26 %
top slab	11 %	32 %	57 %
bottom slab	58 %	35 %	17 %

Two symmetric concentrated forces are applied on the front face of pier segment. The resulting vertical stress distributions ω_y for front and opposite faces of the diaphragm is given in Fig. 6.16. Tension ties T_1 , T_2 and T_3 shown in Fig. 6.17 can capture the tension area on the opposite face of the pier segment. Fig. 6.18 shows more refined model in three dimension.

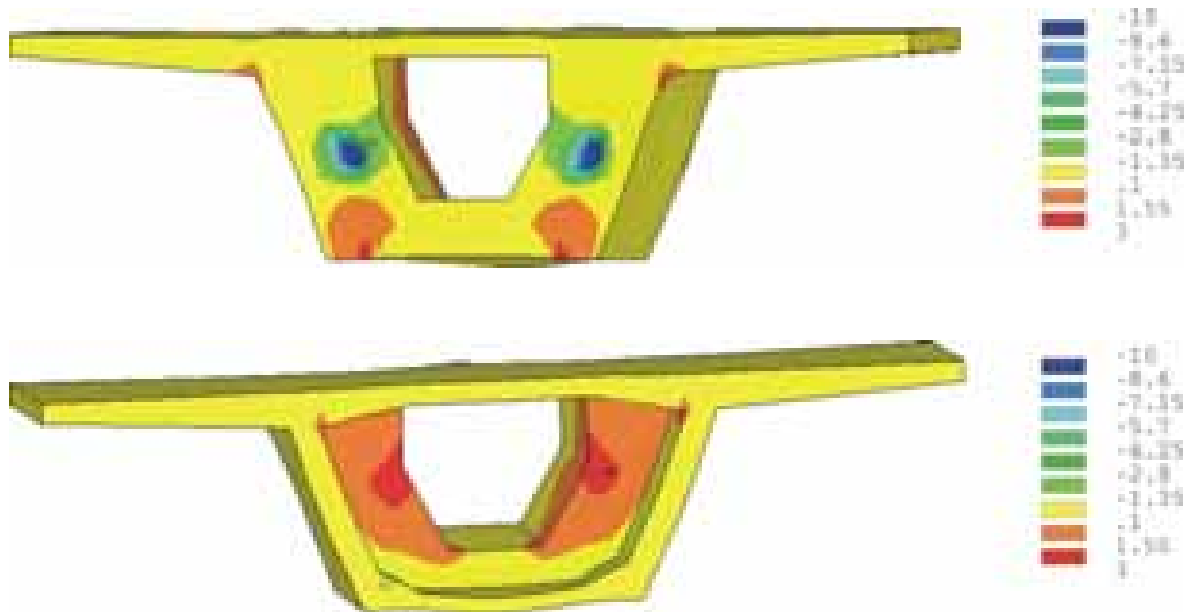


Figure 6.16 Vertical stress ω_y

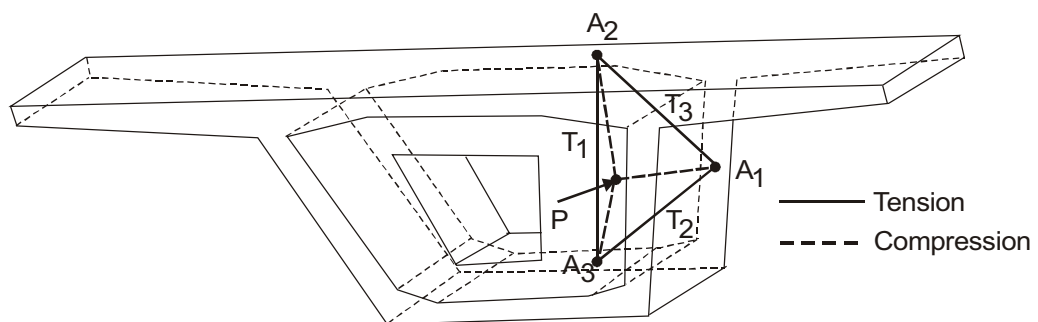


Figure 6.17 Tripod 3-D model

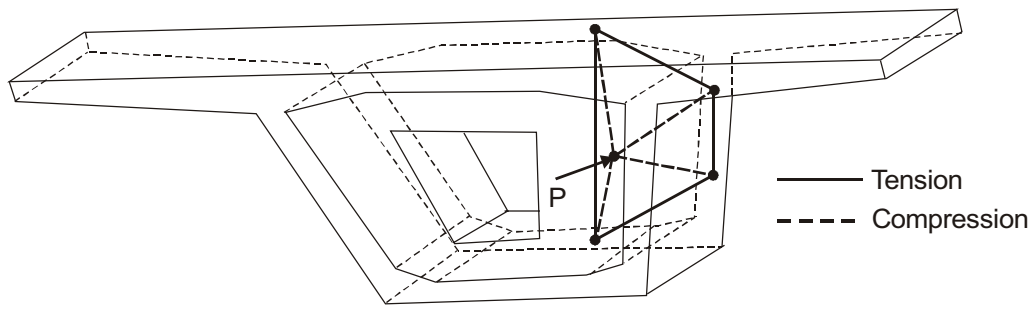


Figure 6.18 Refined 3-D model

7 Summary and conclusion

The design of pier segments is still based on rough approximations. The analyses carried out in this thesis are aimed to create better, more realistic strut-and-tie models for practical design of diaphragms. The background information for the development of strut-and-tie models in D-regions was explained in Chapter 2 of this dissertation. The discussions in this Chapter were focused mainly on the works of Schlaich [3, 7] and Wollmann [4] due to their direct correlation to the nature of the research conducted here. Schlaich's works concentrate on development of strut-and-tie models on shear walls due to the vertical loading. Whereas the work of Wollmann fills the gap left by the former researcher: horizontal loading. Although the works done by these two researchers are tremendous, still they contain some inaccuracies in their models and in further analysis.

The works of Schlaich have been thoroughly examined in Chapter 3 of this dissertation. The finite element results show that shear wall with two supports and closed diaphragm has very good agreement with the strut-and-tie model developed by Schlaich. But the finite element results for shear wall with two supports and open diaphragm and shear wall with central support and closed diaphragm show differences from Schlaich's models. So his models were refined and more accurate strut-and-tie model were developed for both cases.

A 3-D finite element analysis of an existing segmental bridge was developed in Chapter 4 to study the load path on the pier segments and the behaviour of stresses on the first joints. The discussions on differences and similarities of elastic stresses for open and closed diaphragm for all types of loadings were done. The extracted results from finite element analysis of pier segments indicate that first joint shows non-linear stress and strain distributions. Although the research was conducted on the standard bridge that had been constructed in Bangkok [29], it may not show the exact behaviour of stresses for diaphragms with other dimensions. Moreover during analysis the effects of creep, shrinkage and bowing were not considered.

So it is recommended to do a further research for other dimensions of the bridges to determine the behaviour of horizontal stresses on the first joint.

The strut-and-tie models that were developed by Wollmann [4] for transfer of force from diaphragm to webs and slabs were rectified in Chapter 5 of this thesis. The models and sub models developed by him for transfer of horizontal concentrated force were reasonable but the method used to analyse the values of transferred force were inaccurate. So, a 3-D finite element model of a pier segment was thoroughly investigated and the results of force distributions on the webs, top and bottom slabs have been illustrated on various diagrams for different positions in rows and columns.

After careful observation of stresses on vertical and horizontal directions of the shear walls that have been mentioned on previous Chapters, the new strut-and-tie models were developed in Chapter 6 of this dissertation. The new strut-and-tie models have extra tie forces on the diaphragm than that of Schlaich's models [7]. The simplified empirical formulae for practical purpose were developed to calculate this tie forces. The new strut-and-tie models can further be refined and developed by dimensioning and modelling of struts, ties and by smearing and concentrating of the nodes to include crack width limitations. But for the moment, it is out of the scope of this research. The average values of force that flows from diaphragm to webs and to top and bottom slab were approximated by taking the average results in Chapter 5 and were tabulated in Chapter 6.

References

- [1] Lalande M.L.: L'emploi du béton précontrainte dans la préfabrication des ouvrages d'art. Travaux, August 1946, page 281-298
- [1a] Chen W.F, Duan L.: Bridge Engineering Handbook. Section 11.1-11.4, Boca Raton, 2000
- [1b] Mathivat J.: Reconstruction du pont de Choisy-le-Roi. Travaux, January 1966, page 22-40
- [2] PCI.: Precast Segmental Box Girder Bridge Manual (1978)
- [3] Schlaich J. et. al.: Towards a consistent design of structural concrete. PCI journal, May-June 1987, page 77-150
- [4] Wollmann G.P.: Anchorage zones in post-tensioned concrete structures. PhD. Thesis, University of Texas at Austin, May 1992
- [5] American Association of State Highway and Transport Officials (AASHTO): Guide specification for design and construction of segmental concrete bridges (1989)
- [6] Takebayashi T. et. al.: A full scale destructive test of a precast segmental box girder bridge with dry joints and external tendons. Proc. Civil Engrs. Structs & Bldgs, no. 104, August 1994, page 297-315
- [7] Schlaich J, Schäfer K.: Konstruieren im Stahlbetonbau. Betonkalender 1993 Teil II, page 425-454
- [8] Feix J.: Brücke zur Ile de Ré: Bauingenieur 65 (1990), Seite 161-162
- [9] Nguyen V.-X.: Zum Bau der Brücke Ile de Ré in Frankreich. Bauingenieur 63 (1988), Seite 168
- [10] Specker A.: Der Einfluss der Fugen auf die Querkraft- und Torsionstragfähigkeit extern vorgespannter Segmentbrücken, PhD. Thesis, Technical University Hamburg-Harburg, 2001
- [11] Rombach G., Specker A.: Design of Joints in Segmental Hollow Box Girder Bridges. Proc. of the 1st FIB congress, Osaka, Oct. 2002, page 51-56
- [12] Roberts C.L., Breen J.E., Kreger M.E.: Measurement Based Revisions for Segmental Bridge Design and Construction Criteria. August 1993, page 229-274
- [13] Deutscher Betonverein: Empfehlungen für Segmentfertigteilebrücken mit externen Spanngliedern, Deutscher Betonverein / Bundesministerium für Verkehr, Ausgabe 1999

- [14] Aguilar G. et. al.: Experimental Evaluation of Design Procedures for Shear Strength of Deep Reinforced Concrete Beams. ACI Journal July-August 2002, page 539-548
- [15] Leonhardt F., Mönning E.: Vorlesungen über Massivbau, Zweiter Teil, Sonderfälle der Bemessung im Stahlbetonbau, zweite Auflage, Springer Verlag, Berlin 1975, page 141
- [16] Comité Euro-International du Béton: CEB-FIP Model Code 1990 Design Code, Bulletin d'Information No. 213/214, Lausanne, May 1993
- [16a] Comité Euro-International du Béton: CEB-FIP Model Code 1987, Bulletin d'Information No. 181. Anchorage zones of prestressed concrete members state of the art report, Lausanne, April 1987
- [17] Ansys Engineering Analysis System User's Manual (for ANSYS Revision 7.0), Swanson Analysis. NC. , Houston, USA, 2003
- [18] Eurocode 2 Part 1: Design of concrete structures, issued 1992
- [19] DIN 1045-1:2001: Tragwerke aus Beton, Stahlbeton und Spannbeton Teil 1: Bemessung und Konstruktion, 2001
- [20] Schäfer K., Baumann P.: Ausbreitung von Druckkräften in Betonscheiben- Vergleichende Versuche mit Lasteinleitungen über Lastplatten, Bewehrungsumlenkungen und Bewehrungsknoten. Versuchsbericht, Institut für Massivbau, Universität Stuttgart, 1986
- [21] Wurm P., Daschner F.: Versuche über die Teilflächenbelastung von Normalbeton. Deutscher Ausschuss für Stahlbeton, Heft 286, 1977
- [22] Rostasy F.S., Holzenkämpfer P.: Rechenmodel zur Ermittlung der Tragfähigkeit für die Verbindung Ankerkörper – Beton von Spannverfahren. Forschungsbericht des Institutes für Baustoffe, Massivbau und Brandschutz der TU Braunschweig, Dezember 1991
- [23] Mehlhorn G. et.al.: Anwendung der FEM zur Tragfähigkeitsermittlung der Verbindung Ankerkörper-Beton bei Spannverfahren. Forschungsbericht, Fachgebiet Massivbau der Universität Gesamthochschule Kassel, 1993
- [24] Hegger J., Neuser J.U.: Betonrücken mit Spanngliedern ohne Verbund - Krafteinleitung von externen Spanngliedern, Institut für Massivbau, RWTH Aachen, Seite 1-14
- [25] Neuser J.U.: Zur Krafteinleitung bei externer Vorspannung. PhD. Thesis Institut für Massivbau, RWTH Aachen, 2003

- [26] Kreger M.E.: Evaluation of distress in J-2e Bridge. Final report submitted to the Washington Metropolitan Area Transit Authority, Austin, November 1989
- [27] Eurocode 1-3: Traffic loads on bridges, issued 1991
- [28] Holzenkämpfer P.; Rostásy F.S.: Spanngliedverankerungen im Beton – Umrechnung für die Anwendung nach EC2, Teil 1. Mitteilungen des Institutes für Bautechnik 1992, Heft 3, Seite 85-87
- [29] Rombach G.: Bangkok Expressway – Segmentbrückenbau contra Verkehrschaos. aus: Aus dem Massivbau und seinem Umfeld (Hilsdorf, Kobler ed.). Schriftenreihe des Institutes für Massivbau und Baustofftechnologie, University of Karlsruhe, 1995, Seite 645-656
- [30] American Association of State Highway and Transportation Officials (AASHTO): Standard specifications for highways bridges. Washington DC, 1983, 13th edn.
- [31] Eurocode 2, Part 1-3: Prefabricated structures, issued 1992
- [32] Tjhin T. N., Kuchma D. A.: Computer-Based Tools for Design by Strut-and-Tie Method: Advances and Challenges. ACI Structural Journal, Oct. 2002, title no. 99-s60, page 586-594
- [33] Tan K.H., Naaman A.E.: Strut-and-Tie Model for Externally Prestressed Concrete Beams. ACI Structural Journal, Nov.-Oct. 1993, page 683-691
- [34] Alshegeir A., Ramirez J.A.: Strut-Tie Approach in Pretensioned Deep Beams. ACI Journal, May-June 1992, title no. 89-s29, page 296-304
- [35] Ali M.A., White R.N.: Automatic Generation of Truss Model for Optimal Design of Reinforced Concrete Structures. ACI journal July-August 2001, title no. 98-s41, page 431-442
- [36] Liang Q.Q., Xie Y.M., Steven G.P.: Generating Optimal Strut-and-Tie Model in Prestressed Concrete Beams by Performance-Based Optimisation. ACI Journal March-April 2001, title no. 98-s23, page 226-231
- [37] Yun Y.M.: Nonlinear Strut-Tie Model Approach for Structural Concrete. ACI Journal, July-August 2000, title no. 97-s61, page 581-590
- [38] Alshegeir A., Ramirez J.A.: Analysis of Disturbed Regions with Strut and Tie Models, Publication No. CE-STR-90-1, School of Civil Engng., Purdue University, Indiana, 1990.

- [39] Yun Y.M., Ramirez J.A.: Strength of Struts and Nodes in Strut-and-Tie Model. *Journal of Structural Engineering*, January 1996, page 20-29
- [40] Ramirez J.A.: Strut-Tie Design of Pretensioned Concrete Members. *ACI Journal*, September-October 1994, Title no. 91-s55, page 572-578
- [41] Roberts-Wollmann C.L., Breen J.E.: Design and Test Specifications for Local Tendon Anchorage Zones. *ACI Journal*, November-December 2000, title no. 97-s88, page 867-875
- [42] Siao W.B.: Strut-and-Tie Models for Shear Behaviour in Deep Beams and Pile Caps Failing in Diagonal Splitting. *ACI Journal*, July-August 1993, title no. 90-s38, page 356-363
- [43] Tan K.H., Tong K., Tang Y.: Direct Strut-and-Tie Model for Prestressed Deep Beams. *Journal of Structural Engineering*, September 2001, page 1076-1083
- [44] Walter H., Baillet L., Brunet M.: Modelling of anchors in concrete structures with different contact and friction behaviours. *Proc. fourth World Congress on Computational Mechanics (WCCM IV)*, [CD-ROM], Buenos-Aires, Argentina (1998)
- [45] Maxwell B.S., Breen J.E.: Experimental Evaluation of Strut-and-Tie Model Applied to Deep Beam with Opening. *ACI Journal*, January-February 2000, title no. 97-s16, page 142-148
- [46] Baker J.M.: The cantilevered precast segmental bridge over the Kishwaukee river in Illinois (USA). *L'industria Italiana del Cemento* 1/1988, page 26-33
- [47] Stone W.C., Breen J.E.: Design of Post-Tensioned Girder Anchorage Zones. *PCI Journal*, March-April 1984, page 28-61
- [48] Stone W.C., Breen J.E.: Behaviour of Post-Tensioned Girder Anchorage Zones. *PCI Journal*, January-February 1984, page 64-105
- [49] Grasser E., Thielen G.: Hilfsmittel zur Berechnung der Schnittgrößen und Formänderungen von Stahlbetontragwerken nach DIN 1045, DAfStb, Heft 240, Ausgabe Januar 1972, page 43-56
- [50] Haveresch K.H.: Verstärkung älterer Spannbetonbrücken mit Koppelfugenrissen. *Beton- und Stahlbeton* 95, 2000, Heft 8, page 452-460
- [51] Eibl J., Obrecht H., Wriggers P.: Finite Elemente Anwendungen in der Baupraxis. *Universität Karlsruhe* September 1991, page 71-93

- [52] Beck H., Mehlhorn G., Stauder W., Schwing H.: Zusammenwirken von einzelnen Fertigteilen als großflächige Scheibe. Heft 224 der Schriftenreihe des DAfStb, Berlin 1973
- [53] Provida J.: Zu nichtlinear adaptiven Finite Elemente Analysen von Stahlbetonscheiben. TU München 1999
- [54] Hong S.G., Kim D.J., Kim S.Y., Hong N.K.: Shear Strength Reinforced Concrete Deep Beams with End Anchorage Failure. ACI Journal, January-February 2002, title 99-s2, page 12-22
- [55] Palermo D., Vecchio F.: Behaviour of Three-Dimensional Reinforced Concrete Shear Walls. ACI Journal, January-February 2002, title 99-s9, page 81-89
- [56] Carbone V.I., Giordano L., Mancini G.: Serviceability Behaviour of D-regions. Proceedings of the 1st fib congress, session 13, page 359 –367, Oct. 2002, Osaka
- [57] Brockmann C., Springer S.: Advances in the External Post-Tensioning of Segmental Bridges. Proceedings of the 1st fib congress, session 2, page 251 –260, Oct. 2002, Osaka
- [58] Ikeda H., Fujita M., Kawamura N., Nakajima T.: Design and Construction of Prestressed Concrete Girder Bridges by the Segmental Method on the New Meishin Expressway. Proceedings of the 1st fib congress, session 1, page 279 –286, Oct. 2002, Osaka
- [59] Abe H., Eguich S., Yoshioka T., Keizou K., Cervenka J.: Experiments and Analysis of Concrete Anchorage for Prestressing Tendons in the Kiso River Bridge. Proceedings of the 1st fib congress session 2, page 539 –544, Oct. 2002, Osaka
- [60] Lau C.K., Hui C.H., Wong K.Y., Leung Y.W.: Prestressed concrete application in bridges in the Hong Kong Airport Core Programme projects. Structural Concrete, March 2000, page 27-45
- [61] Shafer G., Brockmann C.: Design and construction of the Bang Na – Bang Pli – Bang Pakong Expressway. Proceedings of the 13th FIP Congress, Amsterdam, page 275-280
- [62] Fischer O., Krill A.: The Bang Na Expressway, Bangkok: A full-scale loading test of a precast segmental box girder bridge for 6 lanes of traffic. Proc. of the 13th FIP congress, Amsterdam 1998, page 503-506

- [63] Rogenhofer H., Herold W.: The Bang Na Expressway - Fabrication of precast concrete boxes in the world's largest segmental yard. Proceedings of the 13th FIP Congress, Amsterdam 1998, page 197-200
- [64] Strasky J., Korenek M.: Short Span Segmental Bridges in Czechoslovakia. PCI Journal /January-February 1986, page 107-132
- [65] Tassin D., Dodson B., Takebayashi T.: Analysing the Ultimate Capacity of a Precast Segmental Box Girder Bridge. Reports Structural Engineering International 1996, page 255-258
- [66] Pate D.: The Chesapeake and Delaware Canal Bridge Design-Construction Highlights. PCI Journal, Sept-Oct. 1995, page 20-30
- [67] Sofia M.J., Homsí E.H.: Fabrication and Erection of Precast Concrete Segmental Boxes for Baldwin Bridge. PCI Journal Nov.- Dec.1994, page 36-52
- [68] Jungwirth D., Bonomo R.: Prestressed Segmental Structures - The German Experience. Concrete International, 1992, page 45-50
- [69] Kreger M.E., Fenves G.L., El-Habr K.C.: Finite Element Analysis of Externally Posttensioned Segmental Box Girder Construction. External prest. in Bridges, ACI, 1990, Detroit, page 1-21
- [70] Strasky J., Korenek M.: Progressive placing of the segmental bridge across the Rokytka valley near Prague. L'Industria Italiana del Cemento 1989, page 586- 604
- [71] Moreton A.J.: Segmental Bridge Construction in Florida – A Review and Perspective. PCI Journal, May-June 1989, page 37-77
- [72] Hurd M.K.: Segmental box-girder bridge construction. Concrete International, September 1986, page 19-26
- [73] American Engineering Co.: Precast prestressed segmental concrete bridge over the river Kentucky at Frankfort (USA). L'Industria Italiana del Cemento 1986, page 446-463
- [74] Muller J.M., Barker J.M.: Design and Construction of Linn Cove Viaduct. PCI Journal, September-October 1985, page 38-53
- [75] Bassi K.G., Lin W.L., Al-Bazi G., Ramakko O. E.: The Twelve Mile Creek Precast Prestressed Segmental Bridges. PCI Journal, November-December 1984, page 30-47
- [76] Wium D.J.W.: Precast Segmental Bridges - Status and Future Directions. Civil Engineering for practicing and design engineers, 1984, page 59-79

- [77] Yu Ching K.: Segmental Box Girders for the High Level West Seattle Bridge. PCI Journal, July-August 1984, page 53-67
- [78] McClure R. M., West H.H.: Full scale testing of a prestressed concrete segmental bridge. Can. J. Civ. Eng. II, page 505-515 (1984)
- [79] Podolny W., Mireles A.A.: Kuwait's Bubiyan Bridge - a 3-D Precast Segmental Space Frame. PCI Journal, January-February 1983, page 68-107
- [80] Ward D. J.: An Overview of Prestressed Segmental Concrete Bridges. PCI Journal, March-April 1983, page 120-131
- [81] Matt P.: Status of Segmental Bridge Construction in Europe. PCI Journal, May-June 1983, page 104-125
- [82] Podolny W. et. al.: Recommended Practice for Precast Post-Tensioned Segmental Construction. PCI Journal, January-February 1982, page 15-61
- [83] Lamberson E.A, Baker J.M.: Kishwaukee River Bridges. Concrete International, August 1981, page 93-101
- [84] Smyth W.J.R.: Byker Viaduct Britain's First Prestressed Segmental Railway Bridge. PCI Journal, March-April 1981, page 92-110
- [85] Lovell J.A.B.: The Islington Avenue Bridge. PCI Journal, May-June 1980, page 32-67
- [86] Muller J.: Construction of Long Key Bridge. PCI Journal, November-December 1980, page 97-110
- [87] Gallaway T.M.: Design Features and Prestressing Aspects of Long Key Bridge, PCI Journal, November-December 1980, page 84-94
- [88] Tadros M.K., Ghali A., Dilger W.H.: Long-term Stresses and Deformation of Segmental Bridges. PCI Journal, July-August 1979, page 66-87
- [89] Muller J.: Ten years of experience in precast segmental construction. PCI Journal, January-February 1975, page 28-61
- [90] Gentilini B., Gentilini L.: Precast Prestressed Segmental Elevated Urban Motorway in Italy. PCI Journal, September-October 1975, page 26-43
- [91] Hanson J.M. et.al.: Recommended Practice for Segmental Construction in Prestressed Concrete. PCI Journal, March-April 1975, page 22-41
- [92] Lacey G.C., Breen J.E., Burns N.H.: State of the Art for Long Span Prestressed Concrete Bridges of Segmental Construction. PCI Journal, September-October 1971, page 52-75

- [93] Murata J., Tsuno K., Ishii H.: Prefabrication and Erection of Prestressed Concrete Highway Bridges by Precast Block Processes. Japan-U.S Science Seminar, August 23-27, 1971, page 149-161
- [94] Lee D.J.: Western Avenue Extension – the design of section five. The Structural Engineer 1970, page 109-121
- [95] Muller J.: Long-Span Precast Prestressed Concrete Bridges Built in Cantilever. ACI Journal 1969, page 705-741
- [96] Falkner H., Teutsch M., Huang Z.: Segmentbalken mit Vorspannung ohne Verbund unter kombinierter Beanspruchung aus Torsion, Biegung und Querkraft. Beton- und Stahlbeton 88 (1993) Heft 7, Seite 182-188
- [97] Specht M., Vielhaber J.: Träger in Segmentbauart mit verbundloser Vorspannung - Biegetragverhalten. Beton- und Stahlbeton 88 (1993), Heft 6, page 149-193
- [98] Dimel E.: Nigerbrücken Ajaokuta, Nigeria - Spannbetonbrücken in Segmentbauweise. Spannbeton in der BDR 1983-1986, page 51-56
- [99] Eibl J., Voß W.: Zwei Autobahnbrücken mit externer Vorspannung. Beton- und Stahlbeton 84 (1989), page 291-296
- [100] Rombach G., Specker A.: Segmentbrücken mit Hohlkastenquerschnitt. Betonkalender 2004, Teil 1, seite 179-211
- [101] Eurocode2 part 2. Design of concrete structure, concrete bridges (stage 34) pr EN 1992-2, July 2003, page 112
- [102] Mörsch E.: Über die Berechnung der Gelenkquader. Beton und Eisen 23 (1924), Heft 12, page 156-161

Appendix A: Forces of the tripod model

To calculate the tensile and compressive forces caused by transfer of force from diaphragm to webs and slabs shown in Fig. A1, the values of force distribution in table 6.2 are taken from the previous chapter.

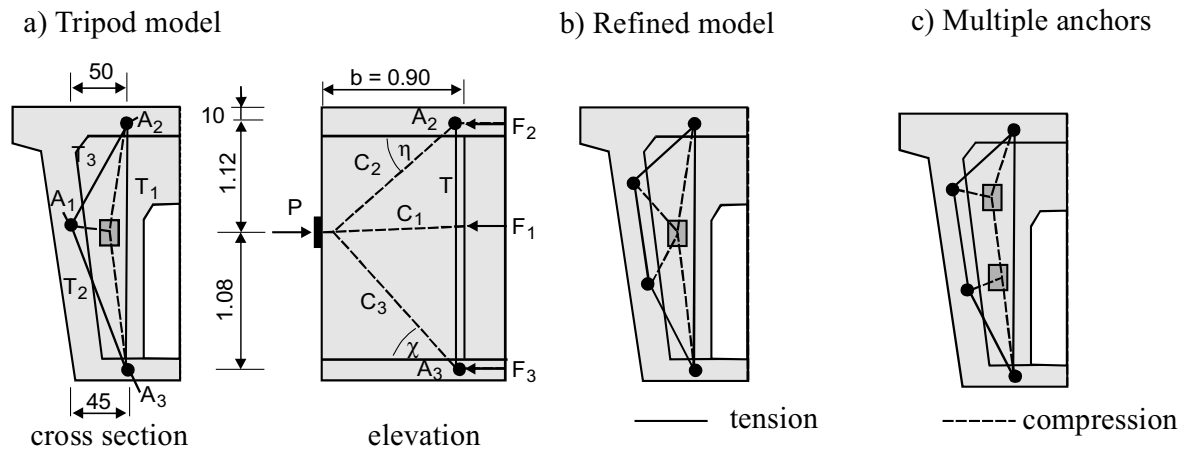


Figure A1 Tripod Model [4]

Table A1 Distribution of prestressing force for diaphragm with manhole on column B (Tab. 6.2) ($L_s=0.35\text{m}$)

parts of pier segment	B1 [h = 1.82 m]	B2 [h = 1.22 m]	B3 [h = 0.62 m]
web	29 %	39 %	33 %
top slab	9 %	26 %	56 %
bottom slab	62 %	35 %	11 %

In the following example, it is assumed that the prestressing force P in Figure A1 is located at a depth of 1.22 m that enables to use the percentages for second column in Tab. A1. The force P has a value of 3864 kN.

$$\text{Force on the web: } F_1 \mid 0.39 \hat{P} \mid 1507\text{kN}$$

$$\text{Force on the top slab: } F_2 \mid 0.26 \hat{P} \mid 1005\text{kN}$$

$$\text{Force on the bottom: } F_3 \mid 0.35 \hat{P} \mid 1352\text{kN}$$

Here by it is assumed that point A1 is located in the same height as the load. By doing so, the calculation of forces is simplified. The model of Neuser [25] is based on the same assumption.

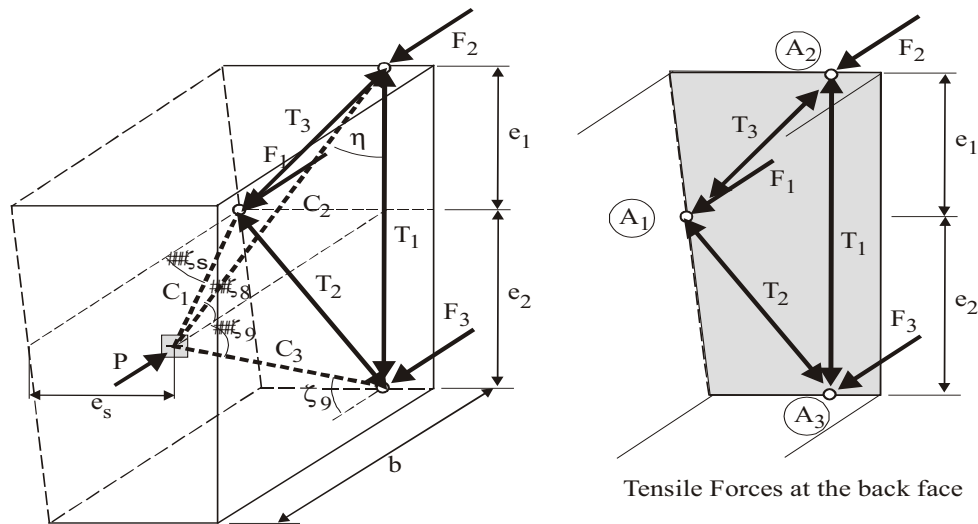
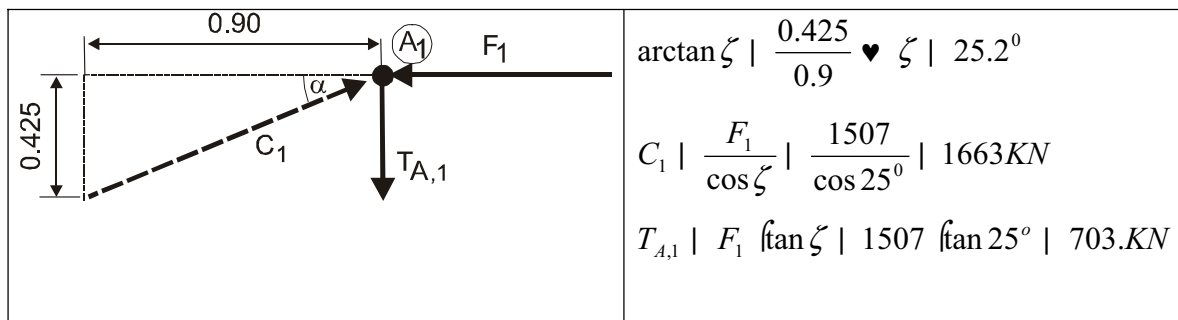
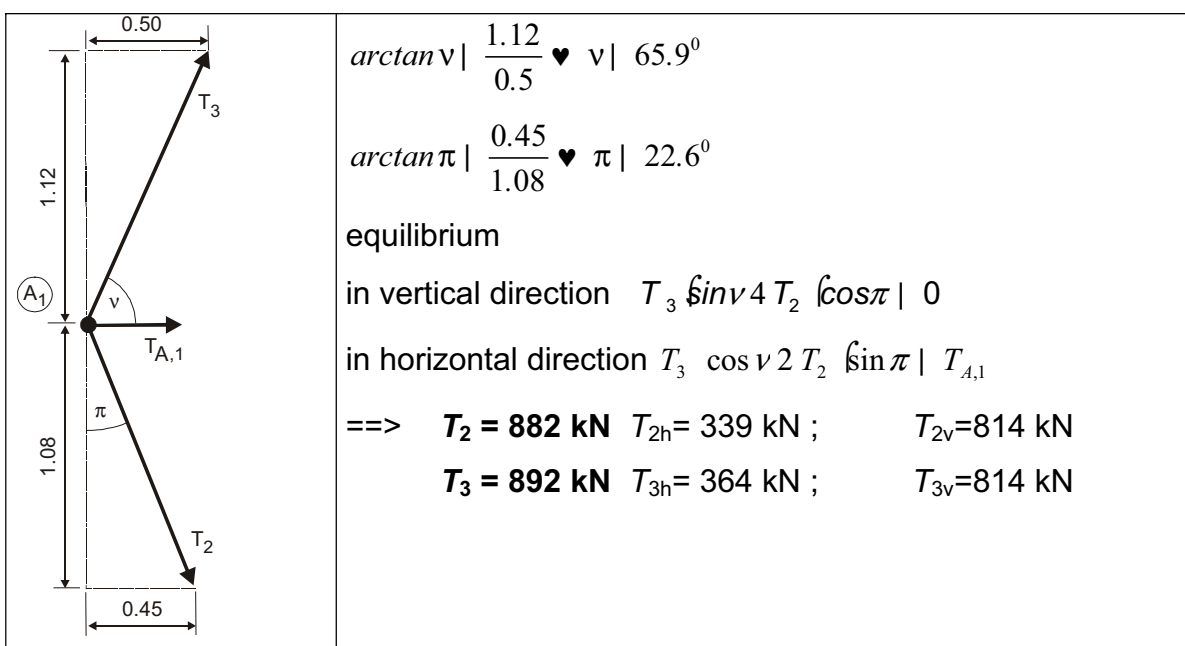


Figure A2 Strut-and-tie model

Node A1: equilibrium in a horizontal plane

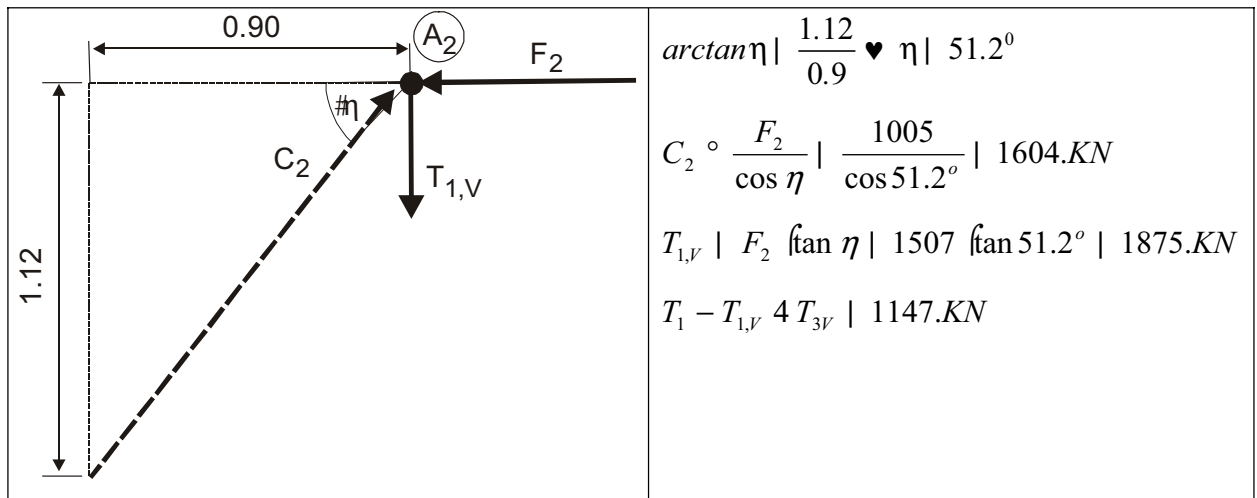


Node A1: equilibrium in a vertical plane

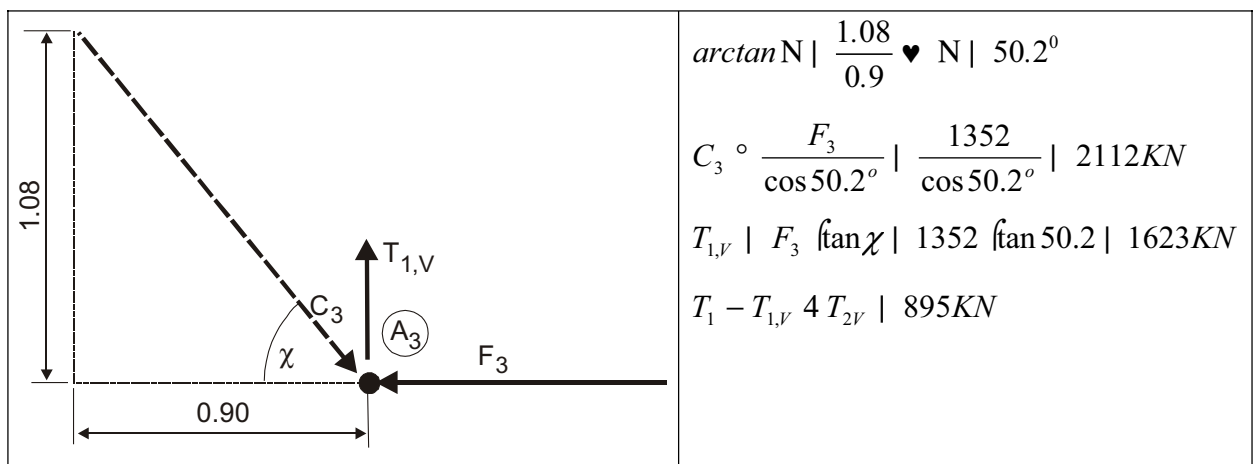


Simplification: Horizontal components of C_2 and C_3 are neglected. For more accurate estimation of forces use the model of Neuser [25].

Node 2: equilibrium in a vertical plane

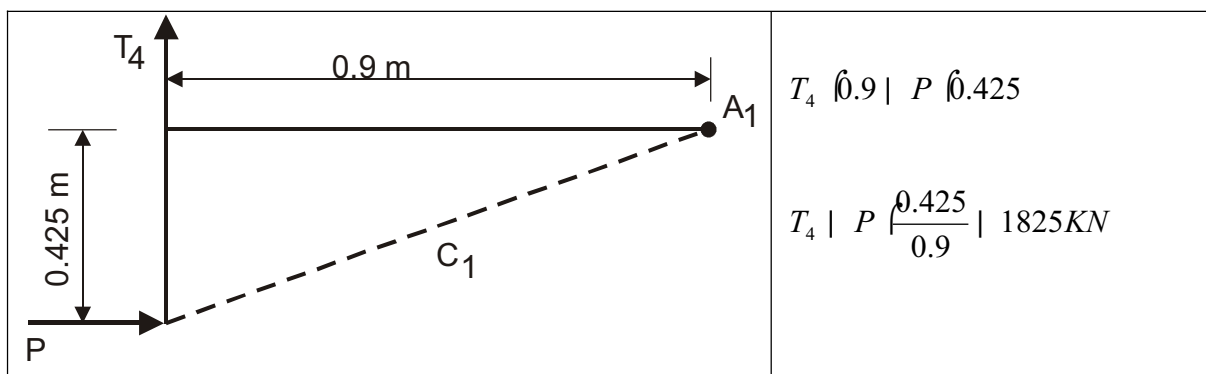


Node 3: equilibrium in a vertical plane



Please note that the stresses in the truss model are very sensitive to the location of the resultant forces F_1 to F_3 . To design a model, which results in the maximum tensile forces should be chosen.

Node A1: equilibrium in a horizontal plane



For reasons of serviceability the corbel action has to be considered. The maximum horizontal force is smaller than T_4 .

Appendix B: Strut-and-tie model of indirect support

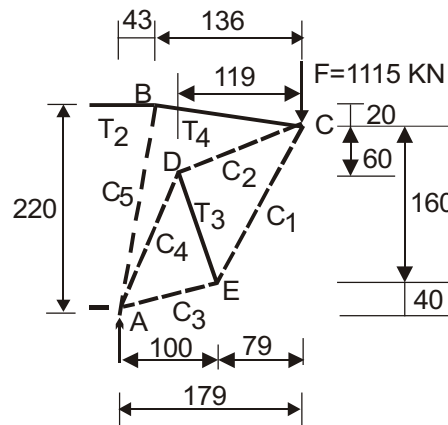


Fig. 1 Strut-and-tie model

NODE: A

$$\begin{aligned}
 -M_A &| 0 \\
 T_2 & \left(\frac{1.79}{2.24} \right) F | 0 \\
 T_2 & | \frac{1115 \left(\frac{1.79}{2.24} \right)}{2.2} | 907.2 \text{KN}
 \end{aligned}$$

NODE: B

$$\begin{aligned}
 -F_x &| 0 \\
 T_4 & \left(\frac{1.36}{1.375} \right) 2 C_5 \left(\frac{0.43}{2.24} \right) | T_2 \\
 0.980 T_4 & 2 0.192 C_5 | 907.2 \dots \dots \dots B_1
 \end{aligned}$$

$$\begin{aligned}
 -F_y &| 0 \\
 4 T_4 & \left(\frac{0.2}{1.375} \right) 2 C_5 \left(\frac{2.2}{2.24} \right) | 0 \\
 4 0.145 T_4 & 2 0.982 C_5 | 0 \dots \dots \dots B_2
 \end{aligned}$$

Simult :

$$\begin{aligned}
 0.980 T_4 & 2 0.192 C_5 | 907.2 \text{KN} \\
 4 0.145 T_4 & 2 0.982 C_5 | 0 \\
 T_4 & | 891.7 \text{KN}, C_5 | 131.7 \text{KN}
 \end{aligned}$$

NODE: C

$$-F_x | 0$$

$$T_{4H} 4 C_1 \left(\frac{0.79}{1.7844} \right) 4 C_2 \left(\frac{1.19}{1.3327} \right) | 0$$

$$0.4427C_1 + 2 \cdot 0.8929C_2 | 882.KN \dots \dots \dots B_3$$

$$-F_y | 0$$

$$T_4 \left(\frac{0.2}{1.375} \right) 2 C_1 \left(\frac{1.6}{1.7844} \right) 2 C_2 \left(\frac{0.6}{1.3327} \right) | 1115KN$$

$$0.8967C_1 + 2 \cdot 0.4502C_2 | 985.3 \dots \dots \dots B_4$$

Simult :

$$0.4427C_1 + 2 \cdot 0.8929C_2 | 882KN$$

$$0.8967C_1 + 2 \cdot 0.4502C_2 | 985.3KN$$

$$C_2 | 589.8KN, C_1 | 802.73KN$$

NODE: D

$$-F_x | 0$$

$$C_2 \left(\frac{1.19}{1.3327} \right) 4 T_3 \left(\frac{0.4}{1.077} \right) 4 C_4 \left(\frac{0.6}{1.5232} \right) | 0$$

$$0.3714T_3 + 2 \cdot 0.3939C_4 | 526.65KN \dots \dots \dots B_5$$

$$-F_y | 0$$

$$4 C_2 \left(\frac{0.6}{1.3327} \right) 4 T_3 \left(\frac{1.0}{1.077} \right) 2 C_4 \left(\frac{1.4}{1.523} \right) | 0$$

$$4 \cdot 0.9285T_3 + 2 \cdot 0.9192C_4 | 265.54KN \dots \dots \dots B_6$$

Simult :

$$0.3714T_3 + 2 \cdot 0.3939C_4 | 526.65KN$$

$$4 \cdot 0.9285T_3 + 2 \cdot 0.9192C_4 | 265.54KN$$

$$T_3 | 536.7KN, C_4 | 830.96KN$$

NODE: E

$$-F_x \mid 0$$

$$C_1 \left(\frac{0.79}{1.7844} \right) 2 T_3 \left(\frac{0.4}{1.077} \right) 4 C_3 \left(\frac{1.0}{1.077} \right) \mid 0$$

$$355.3893 \ 2 \ 199.3315 \ 4 \ 0.9285 C_3 \mid 0$$

$$C_3 \mid 597.44 \text{KN}$$

SUMMARY:

	T ₂ (KN)	T ₃ (KN)	T ₄ (KN)
Truss Model	907	536	891
Strut-and-tie model	907.2	536.7	891.7
Existing model	914.3	-	899
Finite element	960	525	960

Appendix C: Comparison of tensile forces

Model	Schlaich's model		Finite element Model	Shear wall
Direct support Closed diaphragm (shear and torsion loading) see section 3.3.2.1	T1	811KN	865 KN	
	T2	1066 KN	869 KN	
Direct support Open diaphragm (pure shear) see section 3.3.1.2	T1	184 KN	396 KN	
	T2	571KN	No tension	
Indirect support Closed diaphragm (pure shear) see section 3.3.1.3	T2	914 KN	960 KN	

Appendix D: Derivation of formulae

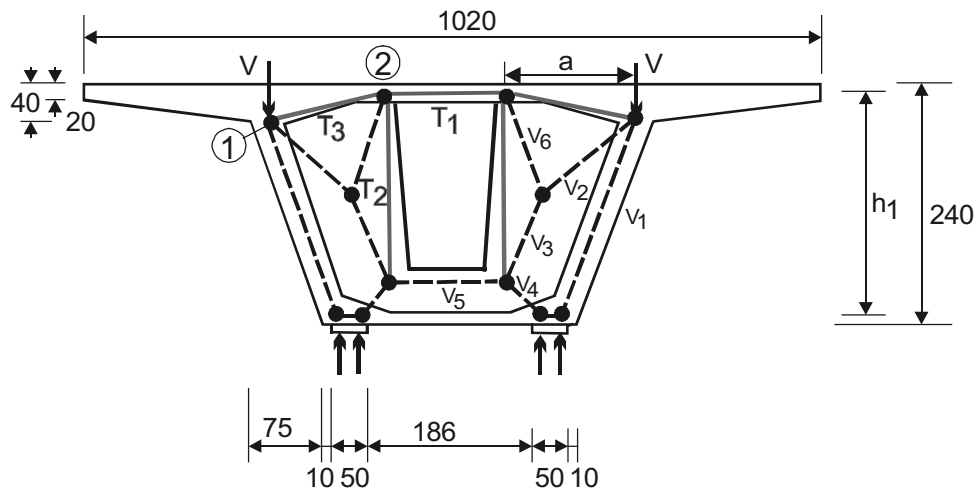


Fig. 1 New strut-and-tie model

Results of compressive forces are taken from Sofistik

$$V \mid 41115KN, V_1 \mid 4745KN \mid 0.67V, V_2 \mid 4432KN \mid 0.38V, V_3 \mid 4540KN \mid 0.48V$$

$$V_4 \mid 4428KN \mid 0.38V, V_5 \mid 4366KN \mid 0.33V, V_6 \mid 4176KN \mid 0.16V$$

Node 1

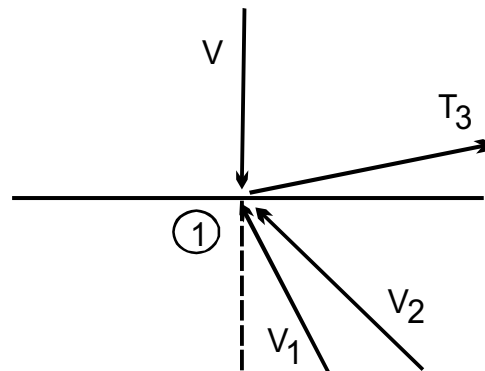


Fig. 2

$$T_{3H} \mid V_{1H} \ 2 \ V_{2H}$$

$$T_{3H}$$

$$\sin \zeta \mid \frac{T_{3H}}{T_3} \heartsuit \ T_{3H} \mid T_3 \ (\sin \zeta \mid 0.995T_3$$

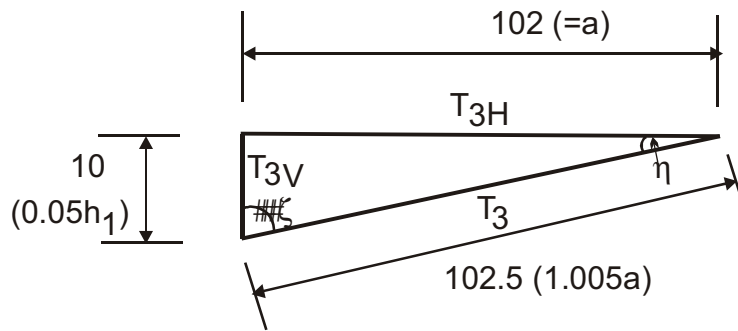


Fig.3

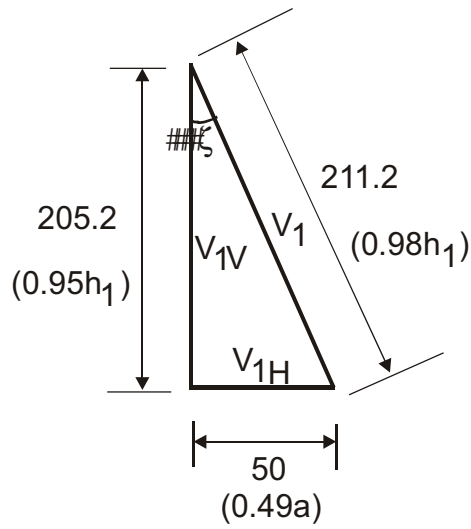


Fig. 4

Horizontal V_1

$$V_{1H} = V_1 \sin \zeta = V_1 \left(\frac{0.49a}{0.98h_1} \right) = \frac{V_1 a}{2h_1}$$

Horizontal V_2

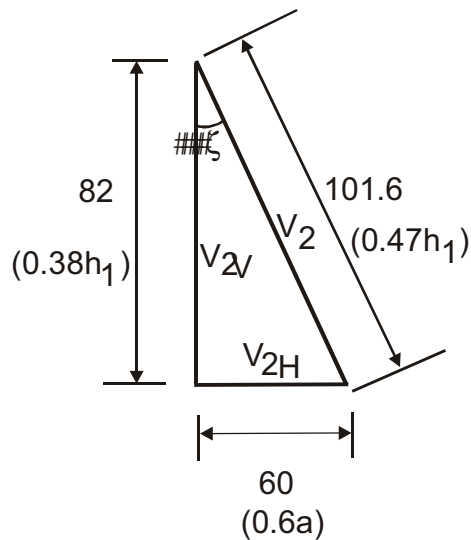


Fig. 5

$$V_{2H} | V_2 \left(\sin \zeta | V_2 \left(\frac{0.6a}{0.47h_1} \right) \right) | 1.28 \left(\frac{V_2 a}{h_1} \right)$$

$$T_{3H} | V_{1H} 2 V_{2H}$$

$$T_{3H} | \left(\frac{V_1 a}{2h_1} \right) | 2 \cdot 1.28 \left(\frac{V_2 a}{h_1} \right) | \left(\frac{V_1 a}{2h_1} \right) | 2 \cdot 0.726 \left(\frac{V_1 a}{h_1} \right) | 1.226 \left(\frac{V_1 a}{h_1} \right) | 0.995 T_3$$

$$\heartsuit T_3 | 1.232 \left(\frac{V_1 a}{h_1} \right)$$

$$\heartsuit T_3 | 0.825 \left(\frac{V_1 a}{h_1} \right)$$

$$\heartsuit T_3 | 434.38KN$$

Node 2

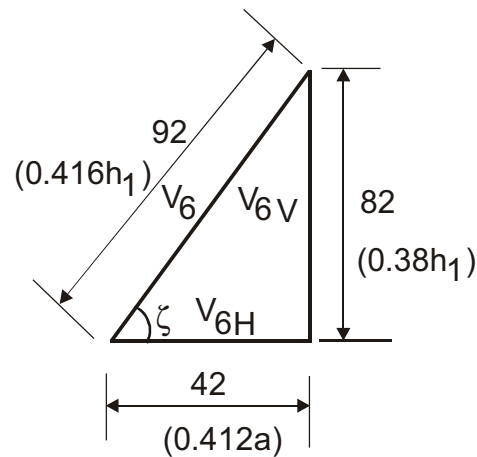


Fig. 6

$$V_{6H} | V_6 \left(\frac{0.412a}{0.426h_1} \right) | 0.155 \left(\frac{V_1 a}{h_1} \right)$$

$$T_1 | 0.995 \left(0.825 \left(\frac{V_1 a}{h_1} \right) \right) | 4 \cdot 0.155 \left(\frac{V_1 a}{h_1} \right)$$

$$T_1 | 0.67 \left(\frac{V_1 a}{h_1} \right)$$

$$T_1 | 352.77KN$$

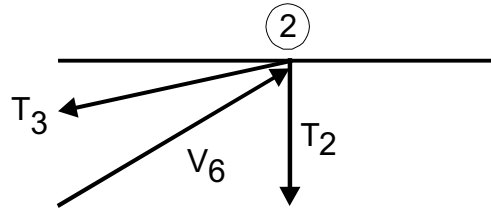


Fig. 7

$$T_2 \mid V_{6V} \ 4 \ T_{3V}$$

$$V_{6V} \mid V_6 \left(\sin \zeta \mid 0.16V \left(\frac{0.38h_1}{0.426h_1} \right) \right) \mid 0.144V$$

$$T_{3V} \mid T_3 \left(\sin \eta \mid 0.825 \left(\frac{V a}{h_1} \right) \right) \left(0.0975 \mid 0.08 \left(\frac{V a}{h_1} \right) \right) \quad \text{See Fig. 3}$$

$$T_2 \mid 0.144V \ 4 \ 0.08V \left(\frac{a}{h_1} \right)$$

$$T_2 \mid \left(\frac{V}{12.5h_1} (1.8h_1 \ 4 \ a) \right)$$

$$T_2 \mid 118.44KN$$

Formulae: For safety reason and to apply the formulae for other dimensions, it is advisable to increase the coefficients of the equations.

$$T_1 \mid 0.7 \left(\frac{V a}{h_1} \right)$$

$$T_2 \mid \frac{V (2h_1 \ 4 \ a)}{12.5h_1}$$

$$T_3 \mid 0.85 \left(\frac{V a}{h_1} \right)$$

RESULT SUMMARY

	T ₁	T ₂	T ₃
Truss Model	366 KN	118 KN	433 KN
Formulae	369 KN	136 KN	448 KN
Finite E. Analysis	353 KN	80 KN	414 KN
Existing Model	184 KN	-	-

Appendix E: Strut-and-tie model of direct support with open diaphragm

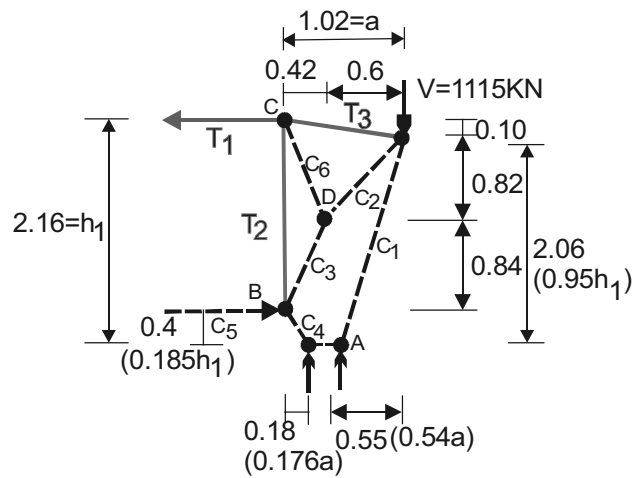


Fig. 1 Strut-and-tie model

NODE: A

$$-M_A | 0$$

$$C_5 \left(\frac{0.185h_1}{4} T_1 \right) \left(\frac{h_1}{2} V \right) \left(\frac{0.54a}{4} \right) | 0$$

$$C_5 | T_1$$

$$T_1 \left(\frac{0.185h_1}{4} T_1 \right) \left(\frac{h_1}{2} V \right) \left(\frac{0.54a}{4} \right) | 0$$

$$4 T_1 \left(\frac{0.815h_1}{4} \right) | 4V \left(\frac{0.54a}{4} \right)$$

$$T_1 \left| 0.66 \left(\frac{V}{h_1} \right) \right| - 0.7 \left(\frac{V}{h_1} \right) \left| \right.$$

$$T_1 | 368.6KN$$

$$-F_y | 0$$

$$C_4 \left(\frac{0.4}{0.438} \right) \left| 2 C_1 \left(\frac{2.06}{2.132} \right) \right| | V$$

$$0.9132C_4 + 2 \cdot 0.966C_1 | V \dots \dots \dots E_1$$

$$-F_x | 0$$

$$C_{4H} + 4 C_{1H} | 0$$

$$C_4 \left(\frac{0.18}{0.438} \right) \left| 4 C_1 \left(\frac{0.55}{2.132} \right) \right| | 0$$

$$0.4109C_4 + 4 \cdot 0.258C_1 | 0 \dots \dots \dots E_2$$

Simult :

$$0.9132C_4 + 2 \cdot 0.966V_1 | 41115KN$$

$$0.4109C_4 + 4 \cdot 0.258C_1 | 0$$

$$C_1 | 4724.36KN, C_4 | 4454.8KN$$

NODE: B

$$-F_x | 0$$

$$C_4 \begin{vmatrix} 0.4109 \\ 0.2 \end{vmatrix} C_3 \begin{vmatrix} 0.3363 \\ 0.2 \end{vmatrix} T_2 \begin{vmatrix} 0.0680 \\ 1 \end{vmatrix} C_5 | T_1 \\ 454.8 \begin{vmatrix} 0.4109 \\ 0.2 \end{vmatrix} C_3 \begin{vmatrix} 0.3363 \\ 0.2 \end{vmatrix} T_2 \begin{vmatrix} 0.068 \\ 1 \end{vmatrix} | 368.6KN \\ 0.3363C_3 \ 2 \ 0.068T_2 | 181.7KN \dots \dots \dots E_3$$

$$-F_y | 0$$

$$C_4 \begin{vmatrix} 0.9132 \\ 0.4 \end{vmatrix} C_3 \begin{vmatrix} 0.9396 \\ 0.2 \end{vmatrix} T_2 \begin{vmatrix} 0.9977 \\ 0 \end{vmatrix} | 0 \\ 454.8 \begin{vmatrix} 0.9132 \\ 0.4 \end{vmatrix} C_3 \begin{vmatrix} 0.9396 \\ 0.2 \end{vmatrix} T_2 \begin{vmatrix} 0.9977 \\ 0 \end{vmatrix} | 0 \\ 0.9396C_3 \ 4 \ 0.9977T_2 | 415.34KN \dots \dots \dots E_4$$

Simult :

$$0.3363C_3 \ 2 \ 0.068T_2 | 181.7KN \\ 0.9396C_3 \ 4 \ 0.9977T_2 | 415.34KN \\ T_2 | 105.2KN, C_3 | 4553.9KN$$

NODE:C

$$-F_x | 0$$

$$4 T_1 \ 2 T_{3H} \ 4 C_{6H} \ 2 T_{2H} | 0 \\ 4 \ 368.6 \ 2 T_3 \begin{vmatrix} 0.9950 \\ 4 \end{vmatrix} C_6 \begin{vmatrix} 0.4560 \\ 2 \end{vmatrix} T_2 \begin{vmatrix} 0.0680 \\ 1 \end{vmatrix} | 0 \\ 4 \ 368.6 \ 2 \ 0.995T_3 \ 4 \ 0.456C_6 \ 2 \ 7.18 | 0 \\ 0.995T_3 \ 4 \ 0.456C_6 | 361.42KN \dots \dots \dots E_5$$

$$-F_y | 0$$

$$C_6 \begin{vmatrix} 0.8904 \\ 4 \end{vmatrix} T_2 \begin{vmatrix} 0.9973 \\ 0.4 \end{vmatrix} T_3 \begin{vmatrix} 0.0970 \\ 1 \end{vmatrix} | 0 \\ 0.89C_6 \ 4 \ 0.0975T_3 | 104.94KN \dots \dots \dots E_6$$

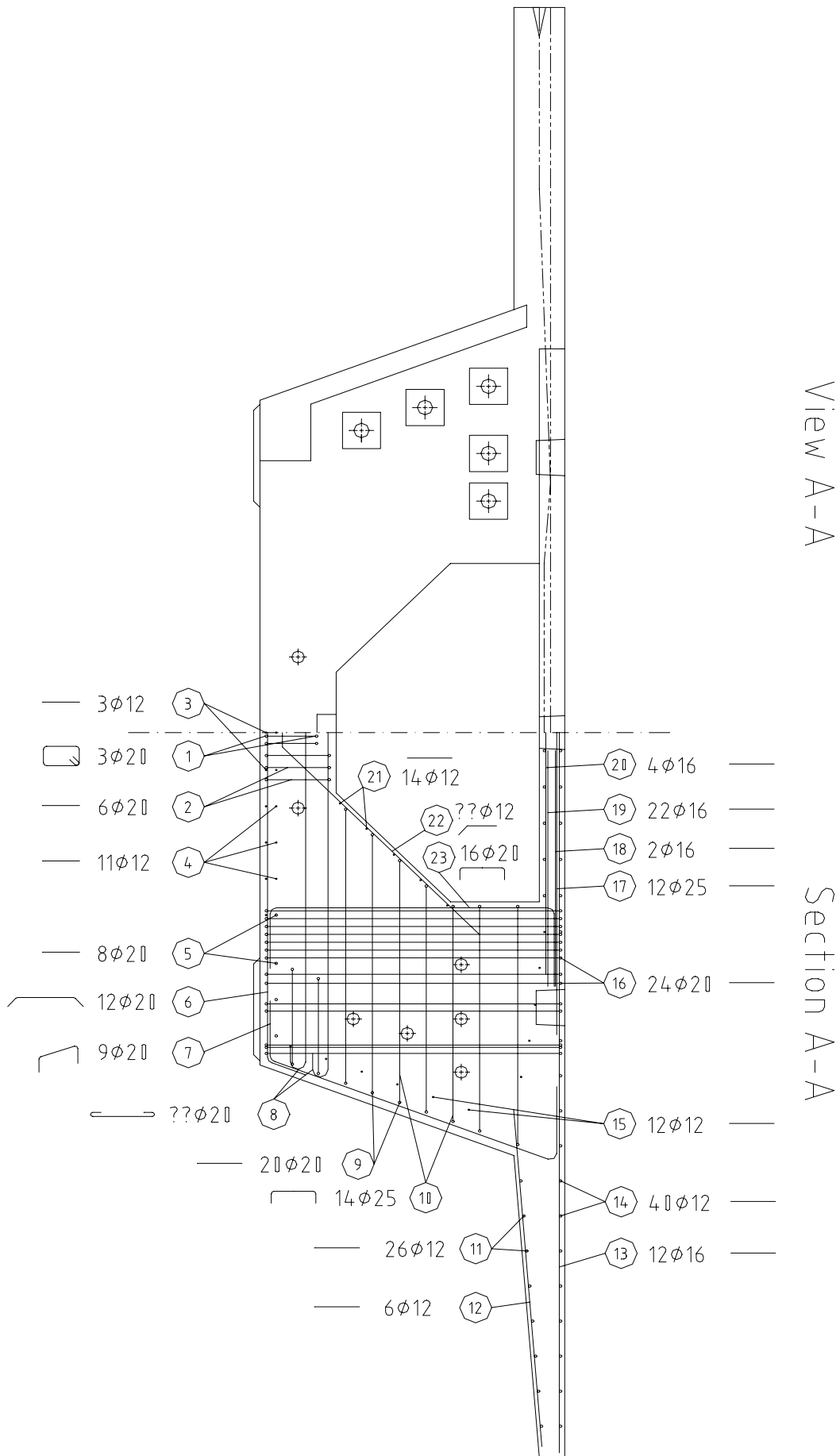
Simult :

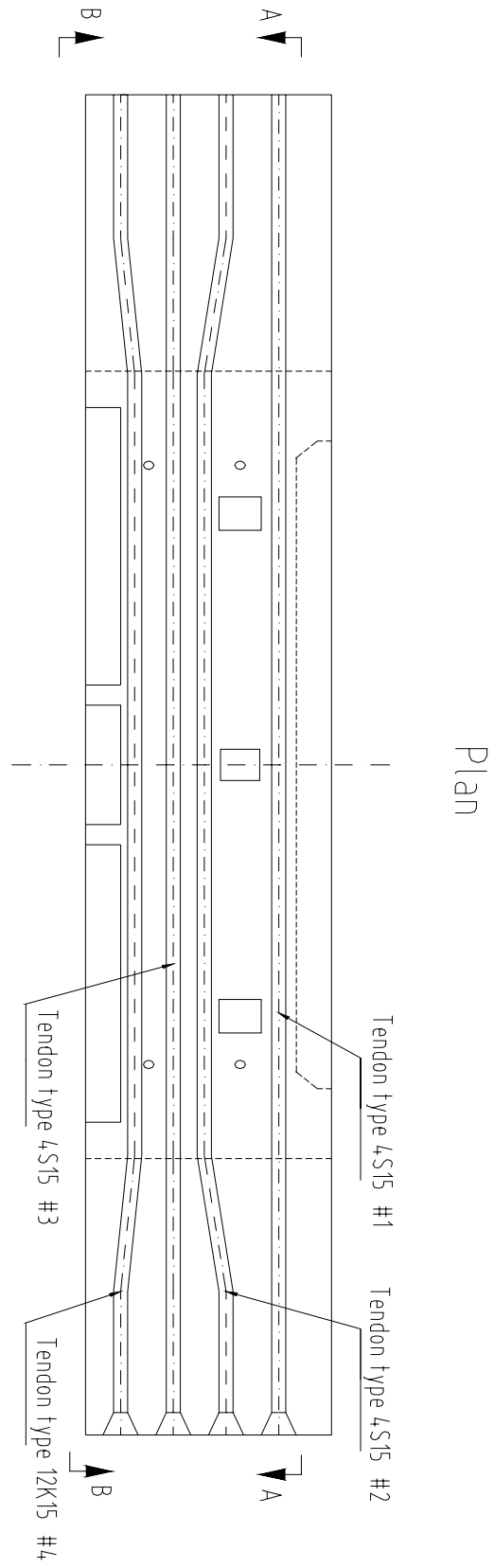
$$0.995T_3 \ 4 \ 0.456C_6 | 361.42KN \\ 4 \ 0.0975T_3 \ 2 \ 0.89C_6 | 104.94KN \\ T_3 | 439.31KN, C_6 | 4166.09KN$$

NODE: D

$$\begin{aligned} &4 C_2 \begin{pmatrix} 0.7682 \\ 0.41661 \end{pmatrix} C_6 \begin{pmatrix} 0.8902 \\ 0.5539 \end{pmatrix} C_3 \begin{pmatrix} 0.94170 \\ 0 \end{pmatrix} \\ &4 \begin{pmatrix} 0.7682 C_2 \\ 0.41661 C_6 \end{pmatrix} \begin{pmatrix} 0.8902 \\ 0.5539 \end{pmatrix} \begin{pmatrix} 0.94170 \\ 0 \end{pmatrix} \\ &C_2 \mid 4486.4KN \end{aligned}$$

Appendix F: Tendon and reinforcement layout of pier segment





Curriculum Vitae

Personal Data

Name Nigatu Chaffo Dullo
Date of birth 20.04.1965
Place of birth Lante
Marital status Single
Nationality Ethiopian

School Attended

1971-1976 Lante primary school, Ethiopia
1977-1982 Arba Minch comprehensive high school, Ethiopia

University attended

1988-1993 Technical University Brno, Czech republic
Awarded degree MSc.

Professional work experience

09/1994-09/1999 Lecturer at Arba Minch Water Technology Institute,
Ethiopia
10/1999-03/2000 Language studies in Bremen, Germany
04/2000-12/2003 PhD. research in department of concrete structure TUHH,
Germany